DYNAMICS OF A PERFECTLY PREMIXED JET FLAME EXHIBITING SELF-EXCITED HIGH-FREQUENCY, TRANSVERSE THERMOACOUSTIC INSTABILITIES

by

LUCKY VO TRAN
B.S. University of Central Florida, 2012
M.S. University of Central Florida, 2014

A dissertation submitted in partial fulfillment of the requirements
for the degree of Doctor of Philosophy
in the Department of Mechanical and Aerospace Engineering
in the College of Engineering and Computer Science
at the University of Central Florida
Orlando, Florida

Spring Term
2019

Major Professor: Kareem Ahmed

ABSTRACT

This work is an investigation of the behavior of a premixed turbulent jet flame in a cylindrical dump combustor. The degeneracy of the simple configuration in this study lends itself for a detailed study of inherent mechanisms of a self-excited thermoacoustic instability in isolation from system coupling effects, enabling detailed numerical simulations to be carried out to supplement experimental findings. Tests were done at a nominal pressure of 8 bar and inlet temperature around 450 ˚C. Self-excited large eddy simulations were also carried out in OpenFOAM, using a b-Ξ flame-wrinkling model to model the combustion process. Eigenfrequency analysis in COMSOL was also done to support and explain the findings from both the numerical simulations and trends observed in the experiments. Measurements from high frequency pressure transducers were analyzed to determine the frequencies of the excited modes in the rig test and compared to the spectra from the LES simulation. The time-resolved fields from the LES simulation were phase-averaged to deduce the acoustic-flame interactions. Despite the (axis)symmetry in this configuration, the non-axisymmetric 1T and 1T1L modes were (simultaneously) excited. Two distinct behaviors are noted for the dynamic flame behavior. In the downstream region, the flame motion is well described by a bulk kinematic displacement as a result of the interaction of the flame front with the local acoustic perturbation. In the upstream region, near the combustor dump plane, large-scale wrinkles are observed in the flame front that have characteristics of a convective wave. The current findings provide additional evidence supporting and further establishing the theory of inherent acoustic-flame interactions as an excitation mechanism (distinct from acoustically-induced hydrodynamic oscillations) for high-frequency, transverse thermoacoustic instabilities.

To all of mankind who will remain on Earth

ACKNOWLEDGMENTS

The study herein was performed during my extended internship with Siemens Energy at the Orlando Campus; I worked primarily in the combustion technology group in the large gas turbines division, with interfaces to the combustion engineering groups and other technology teams. This dissertation is a result of a true collaboration between UCF, Purdue, and Siemens persons. My continued education at the University of Central Florida, the partnership with Purdue University, were opportunities made possible and funded by Siemens. Enrique Portillo Bilbao, my mentor at Siemens, was a key organizer in this arrangement.

I am fortunate to have had correspondence and grown close to numerous outstanding faculty. My committee was stacked with hand-picked members (a rare occurrence): Kareem Ahmed, Alain Kassab, Bhimsen Shivamogi, and Axel Schülzgen; they were extremely supportive of my ideas and helpful throughout my time at UCF. Collaborators at Purdue, who recorded the measurements, include Timo Buschhagan, John Philo, Rohan Gejji, and an-old-friend Carson Slabaugh. The support of additional project leads throughout my tenure is also acknowledged through Ray Laster, Stefan Dederichs, Lukasz Panek, and Michael Huth. The eventual choice of the OpenFOAM solver, modeling approach, and the numerical settings used in this dissertation was developed based on the experiences gained while working on their projects. Invaluable experience was obtained while running simulations for Stefan Dederichs on JURECA, a cluster at the Forschungszentrum Jülich. The spectrum analysis approach used in this dissertation were modifications to MATLAB scripts originally provided by Lukasz. Two notable students and colleagues were Reinout De Jongh and Vahid Sharifi, they were also

running large eddy simulations to earn their own degrees. Reinout was an amicable companion across the sea that shared my struggles of running self-excited LES. I simulated variations of the Duisburg burner case, which Vahid examined for his dissertation work, to contribute to Michael's project. Although more questions were generated than answered, the excitation mechanism in VIPER was made concrete thanks to the shared similarities with the Duisburg burner. The moniker "large scale wrinkles" adopted in this dissertation was generated during constructive discussions with Michael Huth.

Itza Beltran, my only mentee that ever listened, the closest I have to a successor. My kiddo. I'll still be your Mr. With lots of love, Amanda Gauthier: who smiled and said the words I wanted to hear the most, when I wanted to hear them most, from the one I wanted most to hear them from; the only one allowed to serve me mixed drinks. Finally, my family for their unwavering love and support throughout my life.

TABLE OF CONTENTS

LIST OF FIGURES

LIST OF TABLES

NOMENCLATURE

Roman Symbols

b	=	reaction regress variable, volume fraction of unburnt mixture
c	=	solid specific heat
c_p	=	constant pressure specific heat
c_v	=	constant volume specific heat
Co	=	Courant number
d	=	pre-mixing tube diameter
D	=	combustion chamber diameter
f	=	frequency
Fo	=	Fourier number
k	=	turbulent kinetic energy
k	=	thermal conductivity
$\dot{m}$	=	mass flow rate
M_w	=	molecular weight
q	=	volumetric heat release rate
p	=	static pressure
Pr	=	Prandtl number
R	=	gas constant
R_u	=	universal gas constant
Re	=	Reynolds number
t	=	time variable
T	=	temperature
u	=	streamwise velocity component

v	=	normal velocity component
w	=	spanwise velocity component
X	=	streamwise coordinate
y^+	=	non-dimensional wall distance
Y	=	normal coordinate
Z	=	spanwise coordinate

Greek Symbols

α	=	thermal diffusivity
δ	=	Kronecker delta
Δ	=	difference
ϵ	=	turbulent dissipation rate
η	=	group variable
λ	=	wavelength
Ξ	=	flame wrinkling factor
θ	=	scaled, normalized temperature
κ	=	von Karman constant
μ	=	dynamic, absolute viscosity
μ_t	=	turbulent viscosity
ν	=	kinematic viscosity, momentum diffusivity
ρ	=	density
τ	=	shear stress
τ_w	=	wall shear stress

Subscripts

$_0$	=	baseline
$_{app}$	=	apparent quantity
$_b$	=	bulk
$_{cr}$	=	critical
$_i$	=	initial
$_f$	=	film
$_f$	=	final
$_t$	=	apparent, turbulent
$_\tau$	=	friction
$_w$	=	wall

Superscripts

$\bar{}$	=	arithmetic time-average
$'$	=	Fluctuating quantity
$+$	=	non-dimensional, inner coordinate
$\sim$	=	density weighted time-average
$\rightarrow$	=	vector

Abbreviations

AR	=	Aspect ratio
BC	=	Boundary Condition
BP	=	Baseplate
CH	=	Channel
CAD	=	Computed Aided Design
CFD	=	Computational fluid dynamics

DNS	=	Direct Numerical Simulation
DLR	=	German Aerospace Center
FANS	=	Favre-averaged Navier-Stokes
FEM	=	Finite Element Method
FPC	=	Fully Premixed Configuration
FSR	=	Full Scale Range
FVM	=	Finite Volume Method
HWT	=	Half-wave Tube
LES	=	Large Eddy Simulation
LRE	=	Liquid Rocket Engine
LPRE	=	Liquid Propellant Rocket Engine
LNSE	=	Linearized Navier-Stokes Equation
PC	=	Personal Computer
QWT	=	Quarter-wave Tube
RAM	=	Random Access Memory
RANS	=	Reynolds-averaged Navier-Stokes
WALE	=	Wall Adapting Large Eddy (model)

CHAPTER ONE: INTRODUCTION

Increasing (more stringent) emissions regulations has pushed the gas turbine industry towards lean premixed combustion. Unfortunately, lean premixed combustion is also susceptible to thermoacoustic oscillations. Thermoacoustic instabilities have been encountered in many engineering applications, most notably in rocket engines: see Crocco's [1-7] works for examples of combustion instabilities in solid and liquid rocket engines; Zinn [8] and Culick [9, 10] have also wrote several works on the same topic of instabilities in rocket engines. Thermoacoustic instabilities usually occur at discrete frequencies associated with the standing wave acoustic modes of the hardware. For stagnant conditions (no flow), the acoustic modes are eigenmodes of the system (the non-trivial solutions to the acoustic Helmholtz equation). The eigenfrequencies and eigenmodes depend on the geometry, acoustic boundary condition, and sound speed of the fluid medium. The acoustic modes in a cylindrical duct with both ends closed and uniform properties are depicted in Figure 1. For steady flow, the impact of a background velocity is to modify the local propagation speed to be different than the sound speed and the acoustic modes in a system with a steady background mean flow is superficially similar to the modes in a stagnant system with non-uniform properties. Only a limited number of the lowest frequency modes are pictured in Figure 1. There are an infinite number of eigenmodes and the density of modes increases with increasing frequency. Mathematically, the eigenfrequencies form a countable set and form a basis. Thermoacoustic instabilities are a result of interactions between acoustic waves with the spatial and/or temporal variations of fluid and flow properties (density, temperature, pressure, velocity) accompanied with a heat release (usually from combustion).

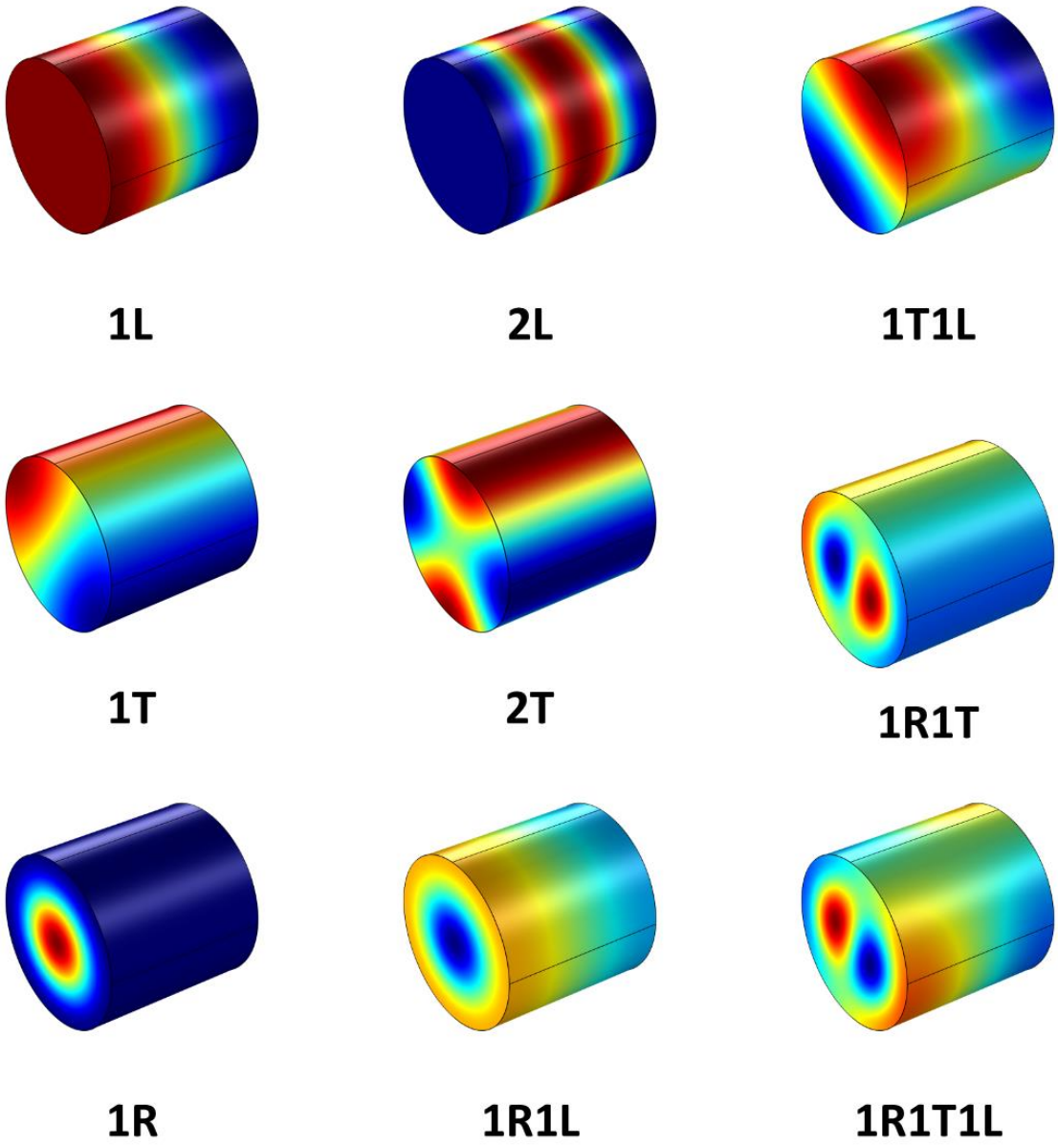

Figure 1: Acoustic modes in a cylindrical duct with closed ends

Lord Rayleigh [11] gave one of the earliest explanations for thermoacoustic instabilities in his explanation of the Sondhauss experiment. Rayleigh reasoned that for thermoacoustic instabilities to occur, a certain criterion must be satisfied: heat must be added while the gas is being compressed and/or removed while the gas is being rarefied. Rayleigh's criterion is now better understood as a condition that the heat release must be in phase with the acoustic pressure oscillations for positive gain or growth. The Rayleigh criterion does not have to be globally satisfied for thermoacoustic oscillations to occur. While some regions of interaction may be out-of-phase and tend to diminish thermoacoustic oscillations, the oscillations can still grow in amplitude if the in-phase interaction is strong enough in other areas or at other times to overcome the diminishing effects of the out-of-phase interactions: it is only necessary to have more constructive interactions occurring than destructive interactions.

For sustained thermoacoustic oscillations to occur there should also be a feedback mechanism, otherwise the flame (providing the heat release) is likely to be disrupted & extinguished. An unsteady heat release may occur under the influence of vortex shedding [12] behind bluff bodies, vortex generators, or unstable shear layers [13]. These unsteady hydrodynamic effects cause the dancing and singing motions in the combustor. For transverse/tangential/azimuthal modes, O'Connor et al. [14] have given a focused review on the interaction between acoustic, hydrodynamic, and combustion processes.The role of hydrodynamic instabilities in triggering thermoacoustic oscillations is an active field of research that is still gaining awareness in the gas turbine community. A recent work by Kirthy et al. [15], using global hydrodynamic stability analysis on measured flow fields, suggests that certain shear layer modes are susceptible to acoustic open-loop forcing (as opposed to closed loop). Their

work demonstrates that the understanding of the role of shear layer instabilities is far from exact and a physical understanding of the processes involved is still being developed, even for simple combustion systems.

Additionally, the acoustic oscillations (as they can propagate upstream) can induce instantaneous air and/or fuel flow fluctuations in the combustion chamber [16]. Works by Lieuwen & Zinn [17] as well as Sattelmayer [18] have highlighted the importance of considering equivalence ratio fluctuations generated by self-excited instabilities which subsequently drive the instability in a feedback loop. The air and fuel supply lines can couple with the acoustic oscillations in the combustor, causing oscillations in the fuel-air mixture due to unsteady mixing. These equivalence ratio fluctuations advect downstream to the flame, causing an unsteady burning rate.

Even for the simple turbulent premixed flames (with constant incoming composition), the turbulent velocity fluctuations in front of the flame give rise to unsteady heat release, which can be converted into flame-generated sound (distinct from flow generated sound). The so-called acoustic radiation by a turbulent premixed open flame was studied by Rajaram & Lieuwen [19]. Hence, various sound sources are naturally present in practical combustion systems. For a given combustion system, an understanding of which of these processes are involved, and which specific process is driving the thermoacoustic instability, is needed to design more robust combustion systems.

It should be apparent that the oscillation amplitude cannot grow indefinitely without an external energy input, there must be some (possibly non-linear) mechanisms that eventually

limits the growth of oscillations. [20] Thermoacoustic oscillations grow in amplitude until the gain is in equilibrium with the damping rates. If the damping is insufficient, the mechanical loading can lead to system rupture or catastrophic failure. Even when immediate damage does not occur, over time the mechanical loading reduces the life of the components due to high cycle fatigue (HCF). Aside from damage, thermoacoustic instabilities may also limit the operability of the engine. The reduced flame stability associated with combustion instabilities may also lead to flashback or flameout. Under large acoustic velocity fluctuations, the flame may instantaneously be located upstream of the intended anchor point or flame-holding position. Once released from the anchoring effect, the flame is free to propagate upstream unless it is impeded by another mechanism. In premixed combustion, the flows in duct passages are usually at a higher velocity than the flame speed. However, the no-slip boundary condition at solid walls ensures that there are always low speed regions where boundary layer flashback is possible. Additional design considerations must also ensure there is enough heat transfer to quench any upstream propagating flames. Similarly, combustion instabilities may also lead to a lifted flame. Classically, the lifted flame is considered an unstable flame as it is free to dance around in the combustor. However, the traditional view that lifted flames are unstable is gradually being overturned, with recent combustor designs specifically exploiting characteristics of stable lifted flames to produce less NOx. The development of the FLOX (**fl**ameless **ox**idation) combustor at DLR is one such example [21, 22].

Thermoacoustic instabilities may be mitigated by the installation of acoustic damper elements such as Helmholtz resonators or quarter-wave-tube resonators, which have distinct damping mechanisms. Helmholtz resonance of a cavity is a spring-mass type effect and is

governed by the resistance at the orifice neck and inertia of gases inside the cavity. A common experience of Helmholtz resonance occurs in a moving car with one slightly opened window. In a Helmholtz resonator (used to mitigate acoustic phenomenon) the acoustic energy is converted into mechanical energy of the gases moving into and out of the Helmholtz cavity which are then dissipated by viscous effects.

The frequency of the Helmholtz resonator is not one of the standing wave modes in the cavity or neck, an acoustic damper based on acoustic resonance is the quarter-wave tubes (also half-wave tubes and so on). They are so-called because of the shape of the standing wave acoustic mode present in the tube (QWT's have one closed end, HWT's have both ends open). Part of the acoustic energy in the combustion chamber is transferred to the acoustic oscillations in the QWT's and then dissipated by viscous effects. Zahn et al. [23] have investigated the influence of the number and positions of QWT's on azimuthal modes. Sohn & Park [24] have compared the acoustic damping provided by quarter-wave and half-wave tubes against Helmholtz resonators. Different selective tuning mechanisms arise for Helmholtz resonators compared to QWT's because they have distinct damping mechanisms. That is, the length of the QWT does not appreciably alter its sound absorption coefficient, whereas it strongly affects the Helmholtz resonator (because it alters the cavity volume). The optimal open area for a Helmholtz resonator is also frequency dependent, whereas QWT's and HWT's are insensitive to the open-area ratio. For the same resonant frequency QWT's generally have better damping than HWT's (it is advantageous to have shorter length tubes for damping). However, HWT's may be incorporated as part of other design features (such as fuel feed lines in engines or propellant feed lines in rockets).

Helmholtz resonators generally provide the greatest damping factor ratio for the smallest footprint, requiring the fewest number of elements to provide the same damping capacity when compared to QWT's and HWT's. A drawback of QWT's and HWT's is their length determines their resonant frequency: long length QWT's and HWT's are needed to damp low frequency instabilities, longer length tubes are also weaker dampers. Helmholtz, quarter-wave, and half-wave resonators all need cooling considerations, especially Helmholtz resonators which are prone to hot gas ingestion. Dampers with negative acoustic refractive index, so called meta-material dampers, have recently been developed to overcome the drawbacks of traditional resonators and create more compact, effective dampers, with promising results thus far. Fok & Zhang [25] have compared the performance of a meta-material damper to traditional Helmholtz and rod-spring resonators.

Piloted Burners

Bandaru & Turns [26] investigated the influence of a pilot on a jet in crossflow configuration. The fuel in their experiments was hydrogen. The hydrogen flow in the pilot was increased with fixed jet flame and crossflow conditions. With increasing pilot, the jet lift-off height decreased until the flame became attached to the burner tube. Increasing the pilot even further eventually lead to the flame attaching around the entire circumference of the burner tube. Goh & Gollahalli [27] performed experiments on a similar configuration, with propane and propylene diffusion flames and with and without a hydrogen pilot. They performed flame structure measurements in order to determine the influence of the pilot on the flame structure.

Bray & Fletcher [28] studied the ignition of cold premixed ethylene air mixtures using a coaxial hydrogen pilot flame under supersonic flow condition. They experimentally mapped the boundary between conditions that would result in ignition and conditions that resulted in quenching of the flame. If the pilot is too small, the heat will be insufficient to overcome the heat loss due to mixing. Quenching occurs until the reaction rate is fast enough to counteract the heat transfer due to mixing.

Masri & Pope [29] developed a velocity-composition based joint pdf transport equation to predict properties in a turbulent non-premixed flame. Cao & Pope [30] investigated different chemical mechanisms and the resulting PDF calculated for turbulent non-premixed piloted flames. The goal of these works were to validate models and test their capabilities of predicting concentrations. These two works were hallmarks in the development of the tabulated chemistry approach.

Nair & Lieuwen have observed the acoustic characteristics of pre-mixed piloted flames and swirl-stabilized flames [31, 32] as well as bluff-body stabilized flames near blowout [33]. The configuration studied by Nair & Lieuwen [31, 32] consisted of a central premixed jet surrounded by a ring of 24 premixed pilots and they were able to control the air and fuel flowrates of the mains and pilot independently. An important characteristic of the configuration and the tested conditions is that the main central jet could not be anchored without the pilot. As the pilot fuel is reduced and the burner approaches blowout, the flame periodically detaches and reattaches from one or more pilots. As the pilot fuel is reduced further, the flame tip begins to violently flap radially.

Li et al. [34] investigated lean blowout in a piloted burner with methane fuel and compared it with blast furnace gases, documenting two important regimes as lean blowout is reached. As the equivalence ratio of the main flame is reduced, the flame enters a regime where it is intermittently extinguished and reignited; this initial regime was referred to as the blowout-reignition state and associated the upper equivalence ratio at which this phenomenon begins as the trigger point. It was noted that the calorific value of blast furnace gases is less than methane with a slower reaction rate, yielding a longer flame. At the same time, the blast furnace gases also have a lower post flame temperature, so that the velocity and viscosity of the burnt mixtures is also less. These conditions provide a longer lifetime for the vortex shedding from the bluff body.

The Sandia Flame D configuration is a well-studied benchmark configuration for a piloted methane flame and has been studied using LES [35]; however, the Flame D configuration is non-premixed. Wang & Chen [36] have focused on modelling the kinetics and radical concentrations in the Sandia Flame D, E, and F. Ritler et al. performed LES on the Sydney piloted spray flame series [37, 38]. Dunn et al. [39] performed the initial characterization of the Sydney premixed piloted jet burner (PPJB). The PPJB consists of a central lean premixed jet with a stoichiometric premixed pilot surrounded by a co-flow of lean premixed hydrogen-air combustion pilots. It is designed specifically to study finite-rate chemistry effects in the thickened flame front regime. Chen & Ihme [38] performed LES on the Sydney PPJB using a three-stream flamelet and progress variable approach.

Barlow et al. [40] studied local extinction and flame blowout on piloted methane-air jet flames using a modified version of the Sydney piloted burner. The modification involves a central tube that can be recessed to tailor the profile of mixture fraction in the central tube. Barlow et al. found that stratified-premixed combustion allows a much great rate of heat release compared to flames with near homogeneous mixture fraction profiles at the burner exit. The additional heat release in the inhomogeneous cases augments the stabilizing effect of the pilot. Velocimetry measurements also showed lower turbulence levels in the near field, suggesting that the shear layer growth is inhibited or suppressed by the heat release of the stratified mixture.

Kundu et al. [41, 42] have investigated the fuel staging in a prototype, downscaled SGT-750 burner: with a main stage, pilot stage, and a Rich-Premixed-Lean burner stage. The prototype burner consists of three concentric stages with the pilot stage in-between the main stage and the RPL stage. Kundu et al. noted that the pilot flame suffers from a NOx emission penalty due to an increase in local fuel-air un-mixedness. An optimized (with better mixing) could likely yield stable operating conditions without a NOx penalty. They also noted that it may be possible under certain situations with low pilot fuel ratio for thermoacoustic instabilities to occur. However, their work focused mostly on static combustion instabilities, they did not take any acoustic pressure measurements. Analysis of the chemiluminescence images revealed a dominant thermoacoustic frequency of 1117 Hz, corresponding to an axial mode. OH-PLIF results hinted that a shear layer instability was present and that the vortices in the shear layer likely play an important role in the mixing of the fresh cold gases with the hot recirculated products.

Dhanuka et al. [43] performed large eddy simulations on a lean premixed pre-vaporized (LPP) combustor with Jet-A fuel. The main flame was premixed, but the central pilot was non-premixed. The nature of the main flame was the primary cause of the unsteadiness in the flow and flame properties. The flame length for the pilot flame by itself varied by only 5%, but the flame length variations increased to 22% when the main flame was added. The main flame was stabilized by hot products from the pilot flame, which in the LPP combustor were carried upstream to the base of the main flames by the recirculation zones.

Although robust burners are often piloted, one can argue that ideally a combustion system could be designed that is always stable without needing a pilot. Attention should be focused on understanding the detailed characteristics of un-piloted systems to make them inherently stable. However, this approach is far from practical. In many situations, the main flames cannot be stabilized (with respect to static instabilities) without the action of a pilot flame. Furthermore, the pilot flame has numerous practical usages. During startup, the pilot flame is usually the first stage to be ignited; the main stages are lit by the action of the pilot flame. The ability of the pilot to extend the operational envelope to a broader range of conditions cannot be overlooked. Operational flexibility is important for running the gas turbine engine at part-load conditions (less than full load) while still meeting emissions requirements (low NOx and CO). The addition of a pilot stage allows for combustion tuning to take place so that these emissions requirements may be met. In order to better design combustion systems, a detailed understanding of the inherent physical mechanisms of self-excited un-piloted flames is needed in order to exploit the benefits of different approaches to suppress instabilities.

Swirl-stabilized Flames

A common feature in industrial burners is to use elements that impart swirl onto the flow before entering the combustion chamber, increasing the operational flexibility of the combustor. For example, the application of a swirled pilot stage into the FLOX burner extended its operational envelope by 10% [21]. The swirl allows for a local increase in velocity magnitude for the same mass-flux (allowing the flow velocity to more easily overcome the flame speed). Additionally, the swirling nature of the flow can dramatically change the flow features the combustion chamber.

Kumaran & Shet [44] performed experiments on a piloted open jet flame with no swirl, low swirl, and high swirl. The effect of swirl is to widen the apex of the flame and reduce the flame length. According to Kumara & Shet [44], the pilot flame at the burner rim improves flame stability by offsetting the heat loss of the main flame near the anchor point. However, the instabilities being referred to by Kumara & Shet are flame lift-off and blowout, not thermoacoustic instabilities. This stabilizing mechanism of offsetting the heat loss is less applicable in an anchored flame subjected to acoustic oscillations. It could however, play a role in lifted flames.

Foley et al. [45] performed PIV and CH-PLIF on a swirl burner in order to analyze the characteristics of a shear layer stabilized flame. Foley et al. refer to flames stabilized by the matching condition of the flame speed and normal flow velocity as normal propagation stabilized flames. An additional process is possible at edges of flames where the edge speed must match the tangential flow velocity, these are referred to as edge stabilized flames. Their findings

suggest that for shear layer stabilized flames, flame blow-off might occur by an imbalance between the flow velocity and the edge flame speed, rather than local extinction induced by flame stretching.

Aguilar et al. [46] studied a single-nozzle swirl burner versus a triple-nozzle burner under transverse forcing. The focus the work by Aguilar et al. was to ascertain the degree to which a simple single-nozzle burner could replicate the complex flow fields in a multi-nozzle burner. An important finding was that, upstream of the jet merging zone, the hydrodynamic influence of one swirling jet on another is minimal. OH-PLIF measurements by the same group were performed later by Smith et al. [47] under leaner conditions. Smith et al. noted that the outer flames cannot be stabilized without the piloting action of the center nozzle (they also become lifted). The center nozzle was operated at an equivalence ratio of 0.85 whereas the outer nozzles were operated at an equivalence ratio of 0.6 in order to simulate a central pilot. Smith et al. found that the flame brush for the single nozzle was much thinner than the triple nozzle, suggesting that the flame for a single nozzle and triple nozzle may have different responses to the flow.

Färber et al. [48] compared the stability of a piloted and un-piloted industrial swirl burner near the lean blowout limit. Unpiloted flames had narrower cone angles and smaller inner recirculation zones than piloted configurations. Lean blow-off occurred only for the narrower cone angles and the stability of the flame was correlated to the flame shape, which was significantly influenced by the pilot and wall heat flux conditions.

Froud et al. [49] studied the precessing vortex core for a piloted premixed burner with swirl and found that the center of the vortex was periodically displaced from the burner axis,

resulting in the precessing phenomenon. The reversed flow zone is also periodically displaced, but lags behind the vortex core forming a feedback loop. The precessing vortex core phenomenon demonstrates how easily a complex unsteady flow field can develop due to the presence of swirl. Identifying mechanism for excitation mechanisms for thermoacoustic instabilities in these systems can be difficult when there are unsteady flow effects present (the precessing vortex core phenomenon occurs even in isothermal flows).

Bradley et al. [50] investigated premixed swirling combustion in a rotating matrix burner. They found that at higher equivalence ratios, the flame is stabilized by hot gases in recirculation zones in both the inner and outer zones. At low equivalence ratios (less than 0.6), the flame is stabilized by only the hot gases in the inner recirculation zone. Unstable combustion occurs as an oscillation between these two states, which is triggered by quenching of the flame in-between the two recirculation zones. That is, the combustor is more susceptible to oscillations because the stabilizing effect of the outer recirculation zone is lost at low equivalence ratios. At operating points near the transition where these stabilizing effects are lost, the Rayleigh criterion is more easily satisfied.

Albrecht et al. [51] have attempted to control the instability of a premixed swirl-stabilized combustor formed from a displaced half-cone. In addition to a direct suppression of the instability, the introduction of a pilot flame (like fuel staging) also allows the operating point to be changed to a condition that is more stable. This (thermoacoustically) more stable condition might even be nearer the lean blowout limit.

High Frequency, Transverse Oscillations

The study of flames exhibiting thermoacoustic oscillations can be generally categorized as self-excited studies [52, 53] (where there are no external perturbances) and forced-excitations studies [54-57] (where a loudspeaker or siren is used to generate acoustic waves); both approaches are found in experiments and numerical simulations. For can-type combustors, where the axial length is long relative to the diameter; the transverse (1T, 1T1L, 2T, etc.) modes in this type of hardware occur at much higher frequencies than the longitudinal modes; radial modes (1R, 1R1L, 1R1T) occur at even higher frequencies than tangential modes because the duct diameter is always smaller than the circumference (by a factor of π). Hence, in disciplines involving axially-long cylindrical/can-type combustors, acoustic modes are generally categorized as high frequency and low frequency modes. The transverse modes (1T, 1T1L,2T, etc.) are categorized as high frequency modes and the lowest order purely longitudinal modes (1L, 2L, etc.) are categorized as low frequency modes. Radial modes are technically categorized as a high frequency mode although the term "high frequency mode" is usually a connotation for the transverse mode. This imprecise reference to the acoustic mode type arises due to practical diagnostic reasons. The acoustic pressure is usually recorded as discrete locations from pressure transducers and analyzed in frequency domain to determine the presence of distinct frequencies, which are then correlated to specific acoustic modes. In other words, the first typical indicator of the presence of an acoustic instability is a frequency. Although the 1T mode in a cylinder has similar characteristics to the transverse modes (also denoted 1T mode) in a rectangular duct, it is also often called a transverse mode (despite being a tangential mode in a cylinder.) The two

terms (transverse or tangential) are often used interchangeably in this scenario. Conveniently, they have the same abbreviation (1T).

Hakim et al. [55] performed LES of a transcritical coaxial liquid oxygen and gaseous methane flame for liquid rocket engine applications; the liquid oxygen was injected through the central post and the gaseous methane was injected through the outer post. They explored three cases: a case without any external forcing, with the injector placed in a pressure node (velocity anti-node), and with the injector placed in a pressure anti-node (and velocity node). Two forcing frequencies were considered in their work: a low frequency forcing case at 2 kHz and a high frequency case at 8 kHz. The low frequency is chosen to be near the most amplified frequency (or natural frequency) of the denser core. They found that the flame was shortened, flattened, and periodically displaced by the acoustic field. For the case with the jet placed at the velocity anti-node, they recognized the bulk flame displacement but concluded that it did not contribute significantly to the acoustic energy growth. However, they noted that depending on the configuration, that mechanism might become important (although they hypothesized this for multiple-element burners).

Saurabh et al. [58] tested a generic premixed swirled flame under simultaneous transverse and axial acoustic forcing and found that the both of the magnitude and phase of the transverse forcing relative to the axial force were important factors affecting the flame response. In their configuration, the axial pulsations due to axial forcing were dominant, the transverse acoustics did not generate significant axial fluctuations on their own. The transverse acoustics interacted

with and could couple with the axial forcing, but their influence was secondary to the axial fluctuations.

O'Connor et. al [54] took measurements of a swirling annular jet flow with and without transverse acoustic excitations. In their configuration, without acoustic forcing, the shear layers generate Kelvin-Helmholtz instabilities that advect (and grow) downstream. With acoustic forcing, the acoustic instability drives a strong rollup of the vortical structures at the acoustic forcing frequency. The vortex roll-up causes large-scale wrinkles in the flame-front.

Many combustion experiments are performed for validating combustion models. (usually under atmospheric conditions). These burners are usually designed to be free of instabilities. An indicator that demonstrates the lack of awareness of the potential for thermoacoustic instabilities to occur is that the acoustic boundary conditions of the burners are seldom reported, whereas velocity and scalar concentrations at inlet boundaries are meticulously matched between numerical simulations and experiments. It is not uncommon for coupling with feed systems to occur because of a lack of attention to detail on the experimenters' part since the focus of their work is on combustion modelling or static flame stability and not thermoacoustic instability. In contrast, due to the challenges involved in the numerical simulation of acoustics, researchers in the field of aeroacoustics are acutely aware of the importance of well-defined acoustic boundary conditions, even for simple domains [59]. Coupling between distinct elements in a combustion system can provide numerous potential mechanisms as the cause/driver of the thermoacoustic instability. However, a flame can still be excited even without these complex and/or combination effects. To understand the inherent mechanisms of transverse instability, it is needed to study

more canonical flame configurations. The mechanisms for instability are still not entirely well-known for even simple, single-element combustors.

Single Jet Flame Studies

Schwing et al. [60, 61] tested a generic single swirl-stabilized burner at atmospheric pressure. The natural gas fuel was premixed with the air before their conical swirl generator. All the burner parts had a circular cross-section. Self-sustained thermoacoustic oscillations at the transverse mode frequency were found over a wide parameter variation, as long as the equivalence ratio was above the critical ratio. They therefore hypothesized that there exists a prevailing excitation mechanism tending to always drive the transverse mode towards instability. Schwing et al. observed that the entire flame brush moves periodically towards the location of the maximum acoustic pressure and proposed a model in [61] which explained how the periodic flame displacement could lead to a positive Rayleigh index, even with a constant burning rate. Berger et al. [62] and Hummel et al. [63] developed this model even further, adding that the flame can also be locally deformed by the acoustic field in addition to displacement. The burning rate can also be intensified (increased or decreased) due to a localized adiabatic compression/expansion of the flame brush under the action of the acoustic pressure (the same energy content is released over a smaller/greater volume, resulting in increased/decreased thermal power intensity).

Zellhuber et al. [56, 64] studied a premixed swirl combustor experimentally and a non-swirled reheat combustor numerically. Self-excited rotating 1T modes were found in the experiment but could not be self-excited numerically. In order to produce the acoustic behavior

in the combustor, the numerical simulation was forced using sources/sinks at the walls (a numerical implementation of a loudspeaker). The swirl combustor was stable at low equivalence ratios (low thermal power) and unstable at high equivalence ratios (high thermal power), but the high frequency instability occurred over a wide range of operating conditions with regard to the swirl number, preheat temperature, and mass flow rate. Even with the different configurations and different investigative means, both cases showed a similar behavior of the reaction zone dynamics (the same flame response to transverse acoustics). For both setups, Zellhuber et al. [64] noted that that high levels of transverse velocity fluctuations led to a coherent wrinkling of the flame front, which is transported downstream at the convective velocity, as well as a periodic displacement of the entire flame in the transverse direction at the acoustic frequency. Unfortunately, Zellhuber et al. did not focus on the process leading to the formation of wrinkles and studied only how the wrinkles interacted with the acoustic field. However, they noted that the wrinkles may not be a driving mechanism since the phase between the local displacement and acoustic pressure changes spatially: there are regions where the flame displacement is in-phase and out-of-phase with the acoustic pressure.

Romain et al. [65] have performed LES on the Purdue Continuously Variable Resonance Combustor (CRVB), a variable length combustor. The CRVB was experimentally investigated at Purdue in [66-71] for many lengths and operating conditions. Romain et al. chose the CRVB setup because the actual geometry is axisymmetric with well-defined acoustic boundary conditions (choked boundaries). Since it is costly to perform 3D LES for multiple operating points and determine stability maps of the transition from stable to unstable conditions, Romain et al. simulated a single unstable operating point with 3D calculations and a 2D axisymmetric

simulation for comparison. The 2D axisymmetric case qualitatively reproduced some features (it predicted the same frequency and acoustic modeshape) but could not predict the correct mean properties of the flow or the flapping movement of the flame due to the axis boundary condition: 2D LES cannot be substituted for 3D LES. The pressure fluctuation amplitude was also severely under-predicted by the 2D simulation compared to the 3D simulation (4.7 bar for 2D whereas the 3D case had an amplitude of 7.4 bar).

Detailed PIV flow measurement and Raman spectroscopy were performed at DLR-Stuttgart by Lammel et al. [72] on a single-jet perfectly premixed methane (also hydrogen) combustor, which is representative of a single main flame in a prototype combustor for a Siemens H-class engine. The combustion chamber length was 60 jet diameters. The inlet pipe duct was very long (more than 40 jet diameters). The combustion chamber was rectangular (4d by 5d) but the jet was off-centered (spacing was 3.5 d from the wall). The off-centering promoted a strong recirculation zone to intensify the mixing of hot burnt gases with fresh unburnt reactants, per the FLOX concept. Themoacoustic instabilities were not observed at any operating conditions reported by Lammel et al., notable because the geometry and conditions tested by Lammel et al. share many common characteristics with the combustor studied in this dissertation. Preheat temperatures of 473 K, 573 K, and 673 K were tested with jet velocities in the range of 90 to 150 m/s. The DLR-Stuttgart rig was operated under steady-state conditions and required a water-cooled jacket to maintain the metal wall temperatures below allowable limits.

The dataset collected by Lammel et al. was used to benchmark the flamelet generated manifold (FGM) model in Fluent by Patil et al. [73], by comparing the predictions of the FGM model with a detailed chemistry model and with the Raman spectroscopy measurements. The implementation of the FGM model in Star-CCM+ is similar to the implementation in Fluent, both are commercial CFD software packages. Patil et al. simulated an inlet duct length of only 15 jet diameters. For the wall thermal boundary condition, they used a uniform wall temperature of 1000 K. Patil et al. noted that the flame position was insensitive to the wall thermal boundary condition even when they considered additional heat losses from convective heat transfer and radiation losses, these heat losses had only a minor effect of the near-wall gas temperatures.

The configuration in this dissertation is a dump combustor with both the inlet premix duct and combustion chamber both having cylindrical cross-sections (whereas the cross-section was rectangular in the DLR setup). The inlet duct length is 18 diameters and combustion chamber length is around 29 diameters of the inlet duct. The experimental setup at Purdue is not actively cooled, the rig is passively heat sink cooled. The thermal boundary conditions in the numerical simulations are taken to be adiabatic walls. The fuel and air are perfectly premixed. The fuel used is natural gas instead of methane. The operating condition are similar, with similar preheat temperatures (680 K) and jet velocities (around 110 m/s). The jet in this study is centered (instead of the off-centered jet at DLR). Despite the centered jet and symmetry in the current setup, the conditions tested are thermoacoustically unstable and the non-axisymmetric 1T mode was excited. Another notable difference is that the current study is performed at a nominal pressure level of 8 bar (the DLR experiment was performed at 1 bar) and the setup is acoustically choked at the inlet and exit.

In this work, a canonical configuration was studied in order to better understand the inherent mechanisms of a the high-frequency transverse instabilities in a cylindrical combustion chamber. Fuel flow fluctuations or equivalence ratio fluctuations is a possible mechanism prevalent in practical combustion system; the flame in this study was premixed so that equivalence ratio fluctuations are not present. The injection system consists of a single unswirled jet flame so there isn't injector-to-injector coupling between multiple injectors. The non-swirling jet also does not impart any bias (to reduce likelihood that a helical vortical mode is present). Without the swirl, the swirl-induce vortex breakdown does not occur; the inner and outer recirculation zones do not form and the precessing vortex phenomenon is not present. Acoustically choked boundary conditions are used at the rig inlet and outlet to ensure well-defined acoustic boundary conditions, and to decouple the combustion chamber from other elements (i.e. no inlet mass flow oscillations due to coupling of acoustic instability with the intake feed). To study the inherent mechanisms, a self-excited approach was used and external forcing was not applied. Natural gas fuel and air as the oxidizer are were in this study, the same combination used in gas turbine engines for land-based power generation. The operating condition is nominally at an elevated pressure of 8 bar and preheat temperature of 680 K. The preheat temperature is representative of the compressor discharge temperature in a gas turbine engine. An experimental setup was designed and tested at Purdue University exhibiting the self-excited transverse instability. The same configuration was modeled using LES to corroborate the experimental findings and provide detailed flow field information not available from the experiment. Supplementary analysis in COMSOL was performed to support and explain some of the findings from the experiment and results from the LES calculation.

CHAPTER TWO: EXPERIMENTAL STUDY

A popular approach for investigating combustion instabilities is to instrument the test rig with loudspeakers or sirens and introduce external acoustic pulsations into the system. This forced excitation approach is common in atmospheric test rigs which do not reproduce the correct aerodynamic flow field to produce self-sustained oscillations. Another reason is that geometrically scaled test rigs cannot easily match the acoustic modeshape or frequency for the transverse or radial/azimuthal acoustic modes, because these modes scale with the chamber diameter or widths. The forced excitation approach was not preferred for the current investigation because of the desire to study scenarios that more accurately represent gas turbine engine conditions. Additionally, the forced excitation approach only reveals the response of the flame due to a given acoustic perturbation (along with a limited number of acoustic-flame interactions). In an actual engine, the thermoacoustic instabilities are self-excited at the operating condition; there are no speakers in actual engines. Personal preferences of the investigators also largely dictate the approach used. The forced excitation approach was not used in CVRC or the current VIPER-S; instead, the thermoacoustic instabilities are self-excited in order to allow an investigation into all physical mechanisms that potentially could be driving the instability.

The single element combustor, VIPER-S (Versatile Intermediate Power Experimental Rig- Single element), located at the Maurice J. Zucrow laboratories at Purdue University [74, 75], was designed to generate self-excited dynamics. The high-pressure combustor can operate with a mean chamber pressure up to 22 bar and pre-heat temperatures up to and exceeding 450 ˚C (the compressor discharge temperature). The VIPER setup was developed using the

experience from the past CVRC setup at Purdue & DLR. Whereas the CVRC setup was adapted for liquid rocket engines; VIPER was developed to study similar effects for a premixed natural gas combustor. The single element configuration (VIPER-S) contains only a single main jet-flame without any pilot. The combustion chamber is cylindrical in VIPER-S, in contrast to the rectangular cross-section at DLR. The jet flame of VIPER-S is also centered, whereas the location of the jet flame in the DLR setup was slightly biased. However, VIPER-S has the well-defined acoustic boundary conditions via a choked nozzle at the inlet and exit of the rig to ensure that the domain is decoupled from external acoustics. The choked nozzles also simplify the boundary conditions needed to model the setup. A schematic of the VIPER-S experimental setup is depicted in Figure 2.

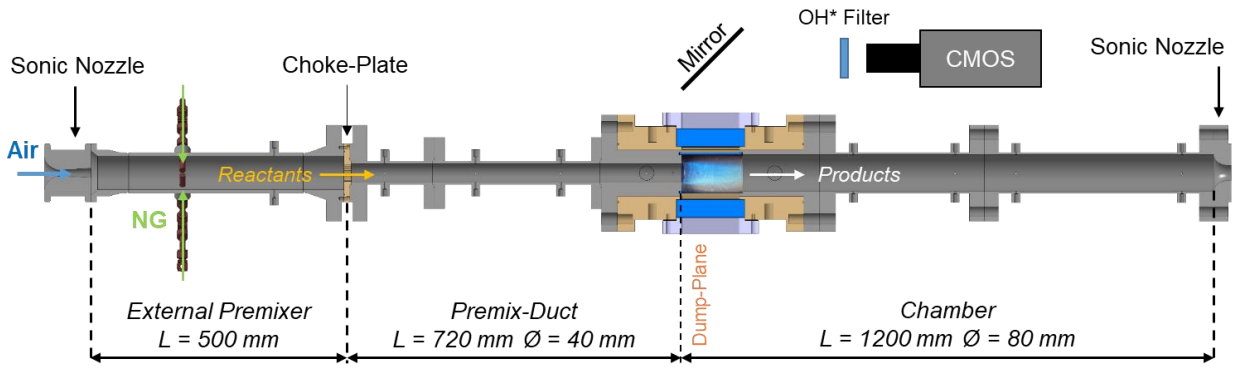

Figure 2: Schematic of VIPER-S setup

The selection of the combustion chamber length was initially guided by the in-house Generalized Instability Model (GIM) solver [76-79] and VIPER-S was originally designed to support 1L longitudinal instabilities, details of which were reported in the publication by Buschhagen et al. [80].

The integrated fuel injector lance from [80] was located in the premix duct. With a fuel injector located in the premix duct, equivalence ratio fluctuations can arise due to air or fuel flow fluctuations and/or unsteady fuel-air mixing rates. The driving differential pressure across the fuel holes in the injector can also become unsteady due to the acoustic pressure perturbation, causing an unsteady fuel flow fluctuation. Air-flow fluctuations can occur due to acoustic velocity perturbations in the premix duct. Either of these (both caused by coupling of the individual elements with the acoustic modes in the combustion chamber) can result in an unsteady mixing process. Even with a constant fuel and air mass flow rates, equivalence ratio fluctuations can potentially still occur if the mixing process is unsteady. In order to eliminate equivalence ratio fluctuations as potential driving mechanisms, the rig was redesigned. The injector lance was removed from the premix duct and instead the fuel was added and mixed with the air in the external premixer upstream, depicted in Figure 2.

Pre-heated air, at a temperature range of 350-500 ˚C enters from a choked inlet nozzle and first enters the external premixer. Natural gas is injected through four producing cylindrical lances, through several bored holes in a jet-in-crossflow style manner. The natural gas and air mix in the external premixer before encountering a multi-hole orifice plate, where the flow is choked again. The gas quality info reported by the utility (measured using gas chromatography) is listed in Table 1 on the test day of the reference experimental case. The natural gas composition is primarily methane, the typical level (across multiple days) is around 90-95% for this supplier. It is unlikely that the detailed chemical kinetics processes are an important driving mechanism for the thermoacoustic instability, since the chemical time-scales are much faster than the flow time-scales. Pure methane gas may be substituted for natural gas by other

experimenters, or a simpler fuel homogeneous composition may be assumed for CFD simulations, and still produce comparable results to this study. The most critical information needed from the fuel composition is primarily the heating value and thermophysical properties of the overall mixture; neither of these are atypical in this study compared to other sources of natural gas.

Table 1: PEPL daily average gas quality info for gas day 07-31-2017

Heating Value $\left[\frac{Btu}{ft^3}\right]$	CO_2 [%]	N_2 [%]	Methane [%]	Ethane [%]	Propane [%]	Ibutane [%]	Nbutane [%]	Ipentane [%]	Npentane [%]	C_6+ [%]
1043	0.267	1.649	92.132	5.697	0.206	0.018	0.020	0.004	0.003	0.004

Non-reacting RANS simulations were carried to design the external premixer. The simulation determined that the un-mixedness arriving at the orifice plate was as low as 2%. An additional increase in premixer length did not improve the un-mixedness significantly. The un-mixedness level could have been further improved by installing turbulators to improve the intensify the mixing rate in the premixer. However, the 2% un-mixedness level was considered low enough for the mixture to be considered premixed and these additional mixing enhancers were not installed.

The orifice plate has a 63-hole pattern: the holes are equally spaced apart, with individual bores of 2.54 mm (0.1 inch). The multi-hole orifice plate was selected (over a single-hole orifice plate) due to the smaller diameter bores of the individual holes. The smaller bore diameters

produce jets with smaller turbulent length scales that decay faster in the streamwise direction. The flow arriving at the combustor dump plane should be less sensitive to the flow structures generated by the orifice plate with multiple smaller bores. The number of bores and bore-size was selected for ease of manufacturability and machining cost.

The premixed natural-gas air mixture than passes through a premix duct of 720 mm length and 40 mm diameter before burning in the combustion chamber. The combustion chamber diameter is 80 mm and is constant throughout the entire ~1.2m length. The diameter ratio is 2, and the expansion area ratio is 4. The flow encounters a sudden expansion at the dump plane and the flame is stabilized by the recirculation, without any pilot, at the dump plane. A choked exit nozzle provides a clean exit acoustic boundary condition and maintains the rig back-pressure (which is nominally 8 bar). The high operating pressure allows VIPER-S to have flow fields that are more representative of actual engine conditions when compared to atmospheric pressure test rigs. There is a 135mm long optical access section. The optical access section is the same 80 mm diameter cylindrical shape as the combustion chamber and does not interrupt the combustion chamber contour. The highest Mach number between the choked inlet and outlet boundaries of the system occurs in the premixing duct: the velocity is on the order of 100 m/s in a cold flow with a sound speed on the order of 500 m/s, yielding a Mach number of around 0.2. Hence, frequency shifts caused by the mean flow can still be considered small.

Although the results with longitudinal instabilities are interesting, they are outside the scope of this dissertation. The current scope is focused only on the results of the configuration without the lance, presumably without equivalence ratio fluctuations and where self-excited

transverse modes were observed. The two primary differences in the hardware configuration exhibiting longitudinal instabilities to transverse instabilities is the removal of the injector lance, and the removal of the contoured inlet nozzle leading up to the premixing duct. In the current configuration showing transverse instabilities, there is a choked boundary condition ensured by a multi-hole orifice plate at the inlet of the premixing duct (which is now 720 mm length).The initial experimental findings with self-excited transverse instabilities were reported by Buschhagen et al. [81], a focused subset of which is utilized in this dissertation to provide a baseline to which the numerical results can be compared.

Thermocouples and low-frequency pressure transducers were implemented at various locations for condition monitoring; high-frequency pressure transducers are also mounted for monitoring the dynamic pressure. Figure 3 shows the relative locations of the instrumentation implemented in the VIPER-S rig: the red dots indicate thermocouples, green dots indicate low-frequency pressure transducers for condition monitoring, and blue dots indicate the locations of high frequency (dynamic) pressure transducers. The detailed locations of the high frequency pressure transducers are provided in Table 2. Sensors are generally located at 3, 6, 9, or 12 o'clock locations. The CUBE transducer was located just downstream of the quartz window section. The CH-04 measurement location is at the aft-most part of the 80 mm diameter combustion chamber, just before the flange for the exit nozzle. PD-03 is the most downstream location the premixing duct, just before the dump plane.

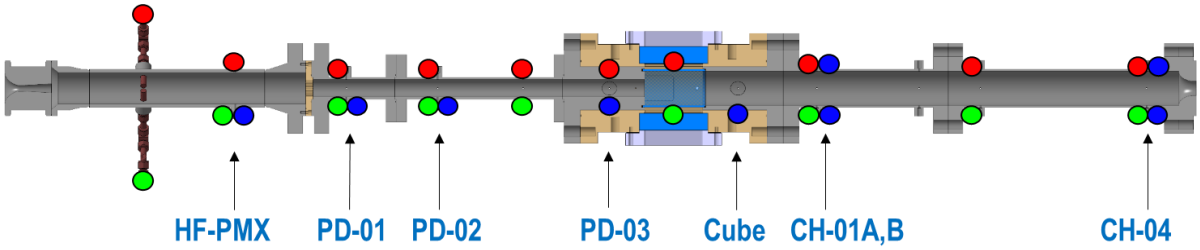

Figure 3: Schematic of high frequency pressure transducer locations

High frequency pressure transducers (Kulite WCT312M-17/35BARA) were installed at multiple axial and circumferential locations in the combustor and sampled at 180 kHz. The transducers were installed in a recessed cavity with a resonant frequency > 9 kHz to allow measurements of the high frequency instabilities in the chamber. A high-frequency transducer installed in the external premixer was monitored to ensure isolation of the premixed reactant flow entering the combustor from any chamber dynamics.

Table 2: Locations of high frequency pressure transducers

Probe Name	Coordinates (x, y, z) [m, m, m]
CUBE	(0.293, 0.000, 0.040)
CH-04	(1.092, 0.000, 0.040)
CH-01A	(0.375, 0.000, 0.040)
CH-01B	(0.375, 0.000, -0.040)
CH-01C	(0.375, -0.0282, 0.0282)
PD-01	(-0.660, 0.000, 0.020)
PD-02	(-0.451, 0.000, 0.020)
PD-03	(-0.295, 0.000, 0.020)
BP-01	(0.000, 0.000, 0.03556)
BP-02	(0.000, 0.03556, 0.000)
BP-03	(0.000, -0.03556, 0.000)

Figure 4: Photograph of the natural gas flame in VIPER (photo by collaborators at Purdue)

During pre-testing, the pre-heated air flows through the system long enough to achieve thermal equilibrium. During this stabilization, the air flowrate is at the desired operating condition, but fuel is not flowing. Because the chamber gases are cold, the chamber pressure is significantly lower than the target of 8 bar during this pre-test phase. Laser-spark-ignition is achieved with an external laser routed into the combustion chamber, through the quartz window used for flame visualization. Fuel flow is activated just before the laser spark is applied. Once the mixture is ignited and the gas temperature increases, the chamber pressure increases rapidly and settles to a nominal pressure around 8 bar. Figure 4 is a photograph of premixed natural gas flame typically occurring in VIPER.

The VIPER-S rig is heat-sink cooled (there is no active cooling). The metal temperatures during pre-test are at moderate temperature of ~450 ˚C. After ignition, the burnt gases (at temperatures on the order of 2000 K) heat up the chamber walls. However, the fired test duration is limited (typically not more than 2 seconds) to limit the metal temperature increase to stay within tolerable limits. The rig was cooled down and returned to the pre-heat temperature in-between tests. The heat-sink cooled nature of this setup and test procedure makes the task of modeling the thermal boundary condition uncertain and complex (since the temperature varies during the test).

A pressure time-trace of the transducer mounted at the CUBE located is provided in Figure 5. The pressure spike at a time near 0.25 seconds is a result of the ignition process. As can be seen, the chamber acoustics quickly enters a limit cycle in approximately 0.25 seconds after ignition. The natural gas fuel in this case stopped at around 1.8 seconds.

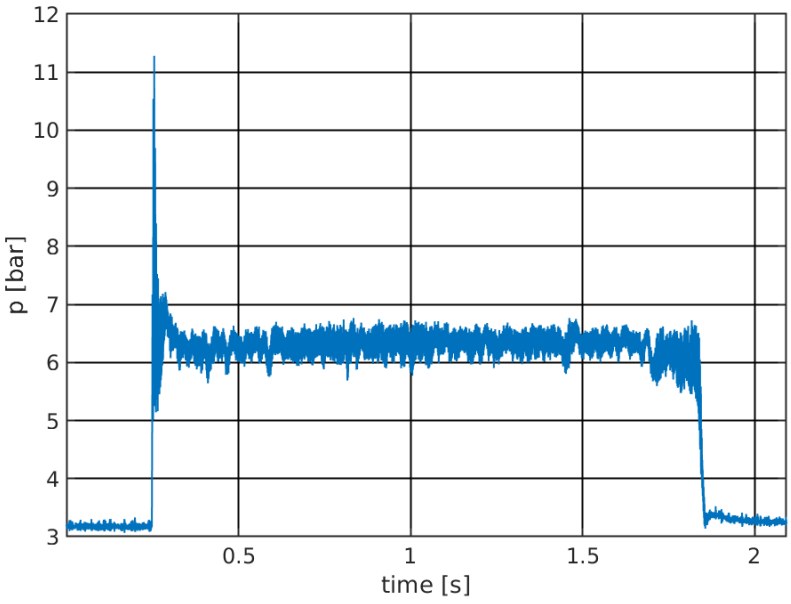

Figure 5: Typical pressure timetrace of CUBE transducer during a test

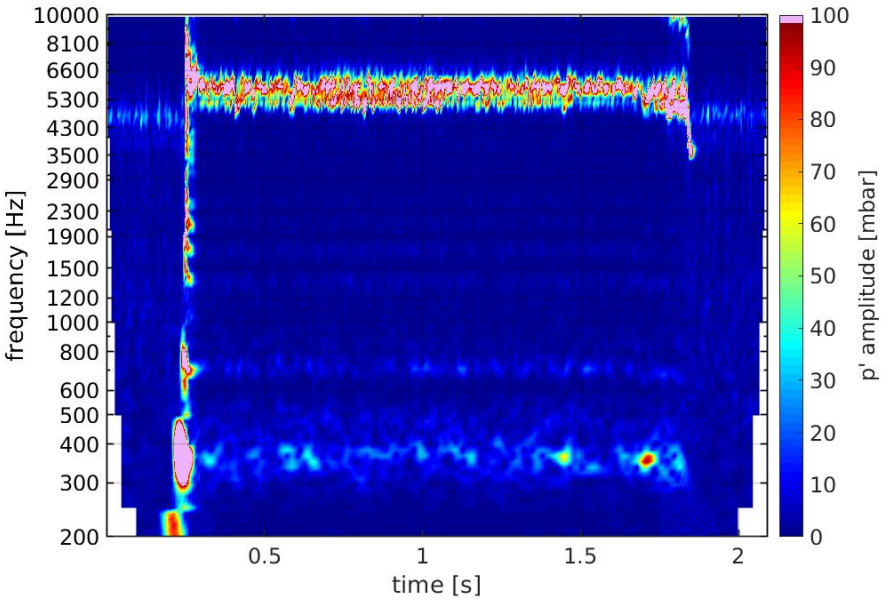

Figure 6: Typical spectrogram of CUBE transducer during a test

Inspection of the spectrogram in Figure 6 shows very minor levels of spectral content before 0.2 s (with very low amplitudes in the 4-5 kHz range). During the ignition process, all the frequencies appear in the spectrogram for a short duration (recall that a sudden spike in physical time domain is uniform function in Fourier domain). After this sort duration, nearly all the frequencies die out except for a few characteristic frequencies around 300-400 Hz, 600-800 Hz, and 5-7 kHz. However, the spectrogram is fairly consistent over time after the ignition transient, until fuel shut-off. This consistency indicates the test duration of ~2 s is sufficiently short to avoid slow thermal drift (from heating of the metal hardware), but sufficiently long to capture a large sample of cycles of each signal. Clipping the signal is necessary to remove any startup and shutdown transients since the flow conditions are drastically different at un-fired and fired conditions. At un-fired conditions, the combustion chamber pressure is on the order of 3 bar, whereas the chamber pressure is at 6 bar at fired conditions. For detailed analysis, since the interest is the thermoacoustic instabilities of the fired state, the signal in Figure 5 and Figure 6 are clipped accordingly and analyzed only over the interesting portion.

Reference Case

In this sub-section the amplitude spectra at each of the measurement locations in Table 2 are presented at representative operating condition from the VIPER-S measurements. The reference case selected is the case with an inlet mass flow rate of 0.553 kg/s (0.53 kg/s of air + 23 g/s of natural gas) and inlet gas temperature of 350 ˚C. This mixture ratio corresponds to an equivalence ratio of 0.75.

Figure 7 is a timetrace of the same signal recorded from Figure 5, but the signal duration has been limited to the interval of 0.6 s to 1.6 s. Figure 8 is the corresponding FFT of the shortened signal and Figure 9 is its corresponding spectrogram. The amplitude in the plot is taken from twice the complex magnitude of each Fourier coefficient at each positive real frequency. The spectrograms of all transducers at all locations (figures not provided) show consistent trends across time. Hence, the flow condition is confidently at a statistically stationary state with respect to the thermoacoustic instability during the plotted interval.

From the FFT in Figure 8, at the CUBE measurement location, peaks are found at 370 Hz, 490 Hz, and 700 Hz with amplitudes of 8 mbar, 3 mbar, and 3mbar, respectively. Significant amplitudes are also found at 5.2 kHz and 5.8 kHz, with amplitudes of 16 mbar and 21 mbar, respectively. CH-01A and CH-01B (in Figure 10 and Figure 11) also have peaks at 370 Hz, 490 Hz and 700 Hz but relatively weak peaks around 5 kHz (amplitudes on the order of a few mbar). Note that CH-01A and CH-02B are just downstream of the CUBE measurement location.Only the lower frequency peaks are detected at the CH-04 in Figure 15. At the aft most measurement location, the only peaks with significant amplitudes are 9 mbar at 370 Hz, 3 mbar @ 490 Hz, and 5 mbar @ 700 Hz. The high frequency peaks are difficult to distinguish from the FFT. From Figure 12, Figure 13, and Figure 14 (corresponding to PD-01, PD-02, and PD-03, respectively), each have peaks at 370 Hz, 500 Hz, and 700 Hz and a single peak around 5000 – 5200 Hz, these peaks have amplitudes just less than 5 mbar, which is still a significant acoustic amplitude. However, the amplitude of the 5 kHz peak is weakest at PD-01 (furthest upstream) and strongest at PD-03 (closest to the dump plane).

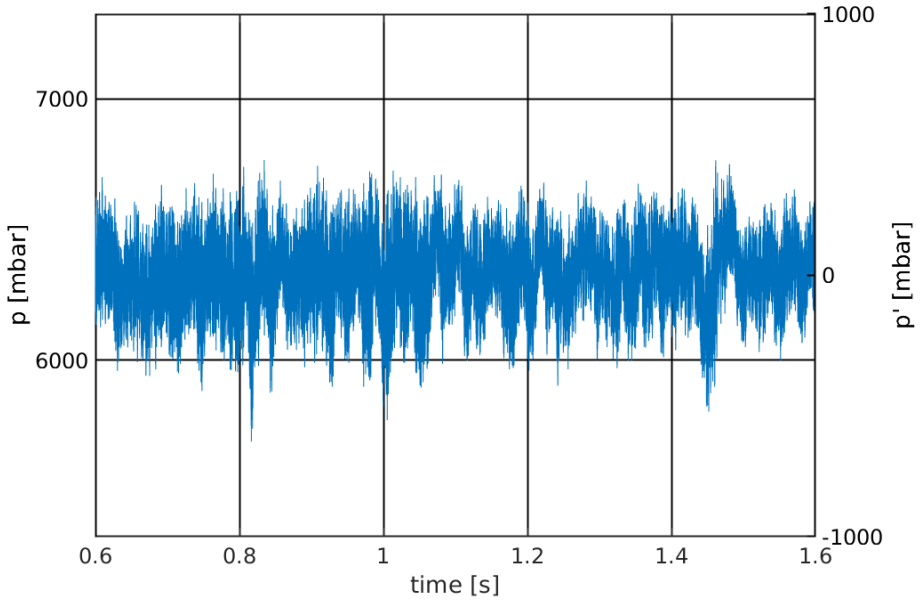

Figure 7: Pressure timetrace at CUBE location for inlet temperature of 680K and Φ= 0.75

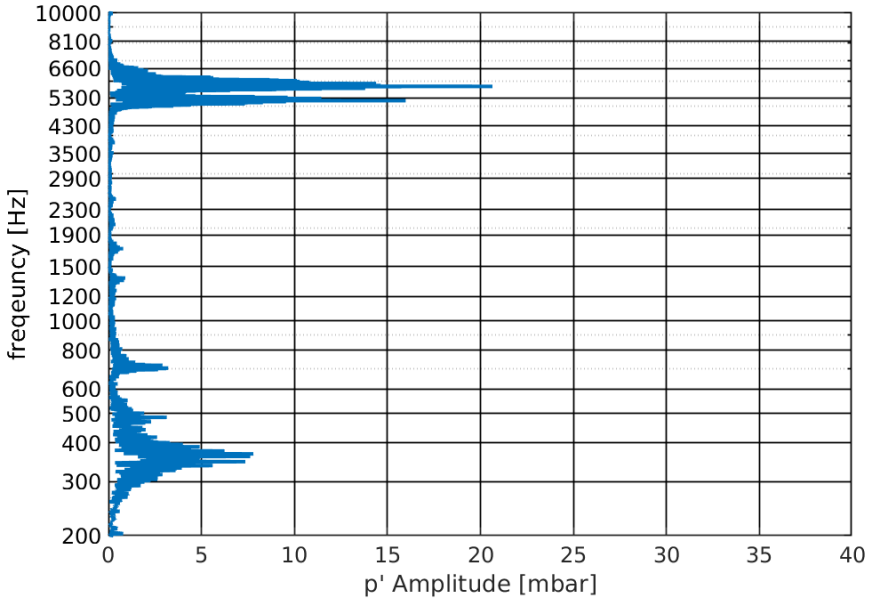

Figure 8: FFT at CUBE location for inlet temperature of 680K and Φ= 0.75

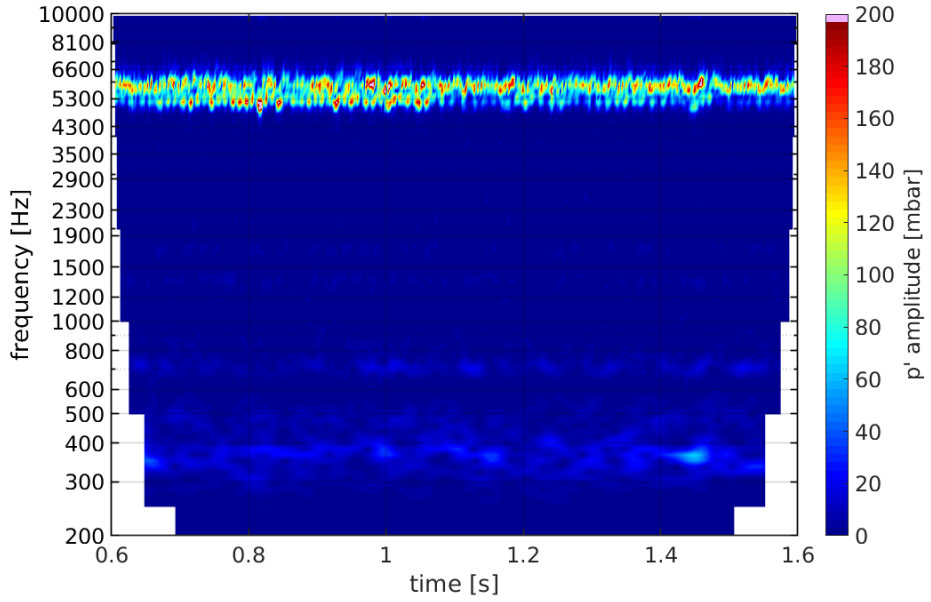

Figure 9: Spectrogram at CUBE location for inlet temperature of 680K and Φ= 0.75

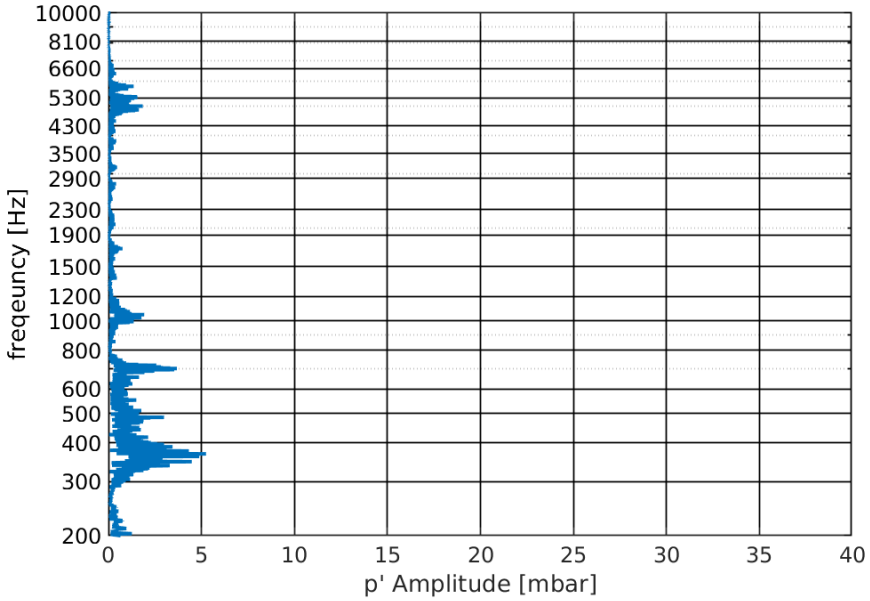

Figure 10: FFT at CH-01A location for inlet temperature of 680K and Φ= 0.75

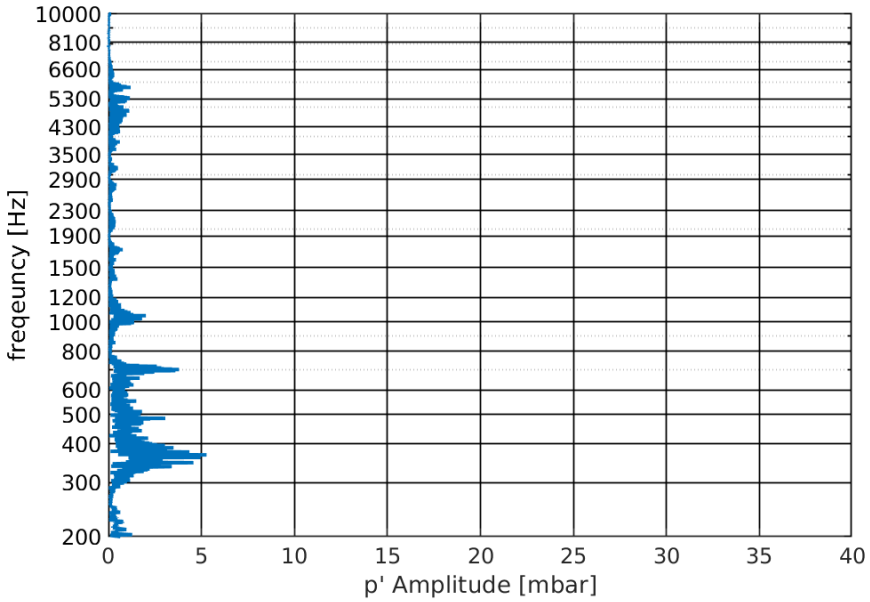

Figure 11: FFT at CH-01B location for inlet temperature of 680K and Φ= 0.75

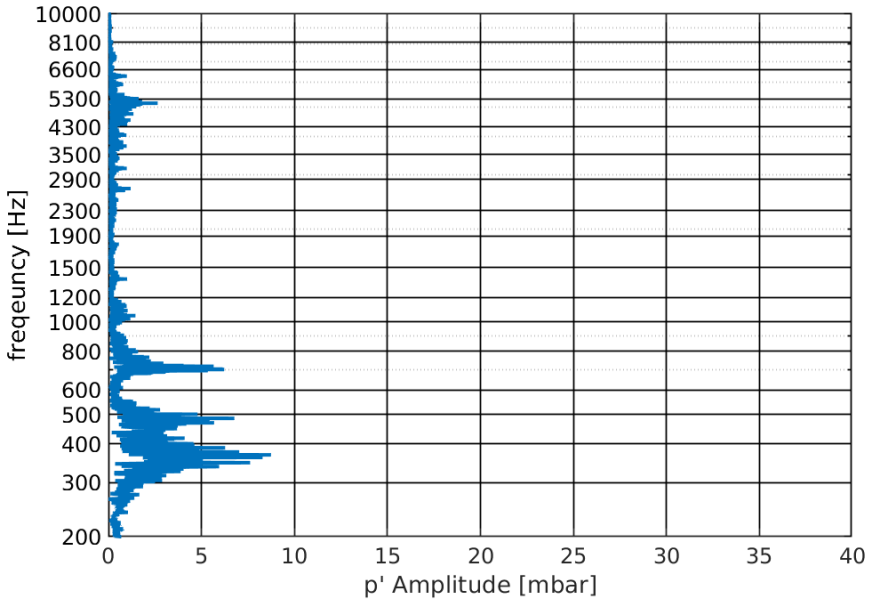

Figure 12: FFT at PD-01 location for inlet temperature of 680K and Φ= 0.75

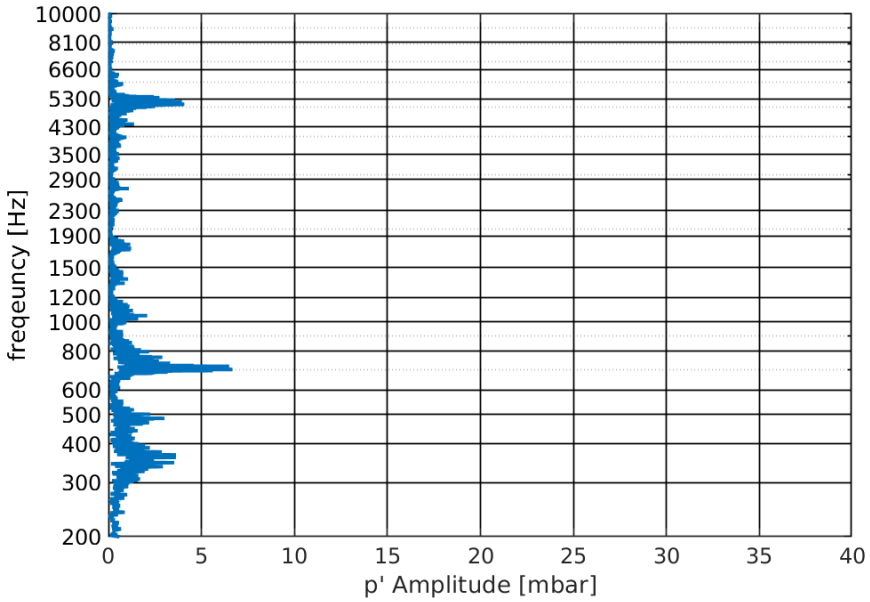

Figure 13: FFT at PD-02 location for inlet temperature of 680K and Φ= 0.75

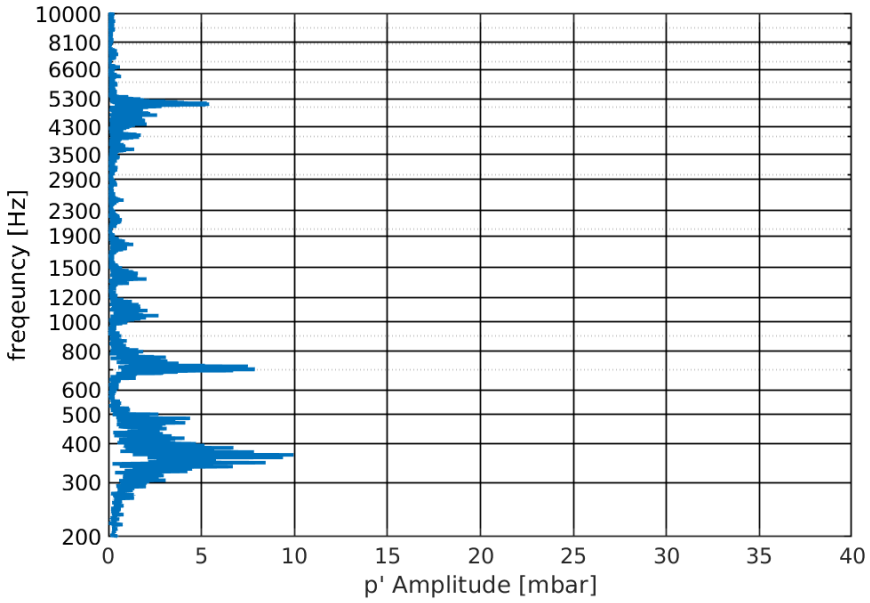

Figure 14: FFT at PD-03 location for inlet temperature of 680K and Φ= 0.75

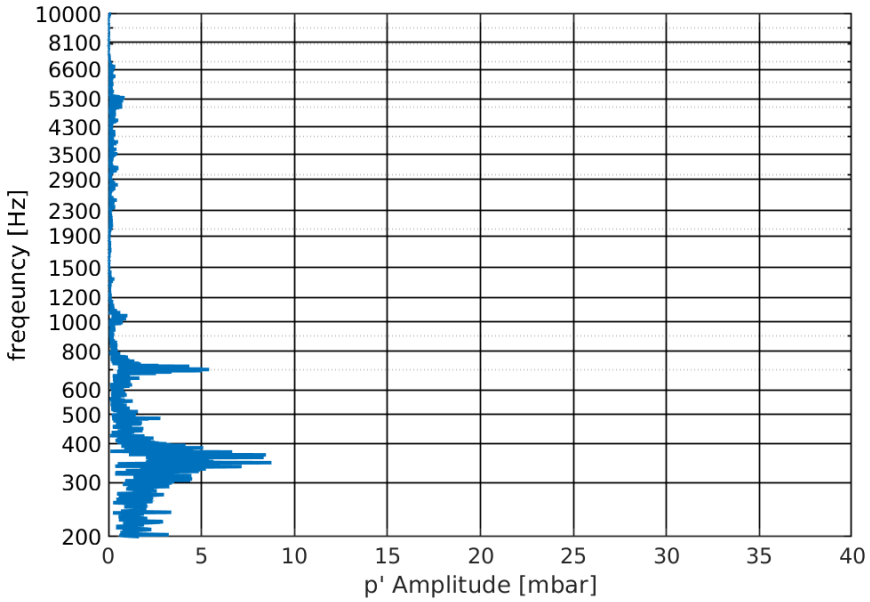

Figure 15: FFT at CH-04 location for inlet temperature of 680K and Φ= 0.75

To summarize, the 370 Hz, 500 Hz, and 700 Hz content is detected at various amplitudes at all measurement stations. On the other hand, the high frequency peaks at 5.2 kHz and 5.8 kHz are appearing only at the CUBE location. Some peaks are found for frequencies near 5 kHz for other transducer locations, but at low levels.

The sound speed of the hot gases in the combustion chamber is around 900 m/s. At this speed, the frequency of the 1T mode in a duct with an 80 mm diameter is around 5600 Hz. Thus the peaks in the spectra at 5.2 and 5.8 correspond closely to the expected frequency range of the transverse acoustic modes of the combustion chamber. If the 5.2 kHz and 5.8 kHz peaks are 1T or 1T1L modes, one would usually expect their presence in the spectra at the CUBE, CH-01, and CH-04 locations. Analysis of the LES results, which is also supported by the eigenmode analysis

in COMSOL, shows that the 1T mode is trapped near the baseplate for this configuration and can explain why the 5 kHz peaks were found only near the CUBE and not the other locations.

From FFT of the pressure spectra alone, it is difficult to rule out other phenomenon that might be occurring. For example, the 5 kHz peaks could be hydrodynamic vortex shedding or mechanical vibrations in the rig. Additional analysis is needed to deduce that these peaks correspond to thermoacoustic instabilities. The claim that these peaks are the signature of the acoustic modes is further supported by the large eddy simulations in the next chapter and COMSOL eigenfrequency analysis in the following chapter. Furthermore, the pressure data does not provide any information regarding the acoustic-flame interactions; the mechanisms for the excitation of these modes requires detailed flow field information, which can be computed readily in LES. It is a significant achievement however, that these modes are excited in this configuration.

The premixing of the natural gas fuel and air in the external premixer before arriving at the choked inlet nozzle should have removed equivalence ratio fluctuations as a driving mechanism in this case. The fuel and air have sufficient mixing length to be spatially uniform by the time they arrive at the orifice plate. The choked nozzle also prevents coupling of the chamber acoustics with the fuel injectors, so that the acoustic instabilities measured in the rig are not induced airflow fluctuations or fuel-flow fluctuations in the external premixer. No external perturbers (loudspeakers or sirens) are used in the rig to impose any acoustic perturbations; the high-frequency instabilities in this configuration are self-excited and the excitation mechanism is self-contained, it is an inherent/intrinsic property of the flow in this combustor.

Instability Trends with Operating Conditions

At very low equivalence ratios, the flame is susceptible to lean blow-off and cannot be sustained. Apart from lean blow-off, the VIPER configuration is generally unstable over a wide-range of operating conditions. In this sub-section, the amplitudes at the characteristic frequencies are reported at different inlet temperature levels and different equivalence ratios but only for the pressure transducer at the CH-04 (CUBE) location. The equivalence ratio was varied by changing the natural gas fuel flow rate (the air flow rate was fixed for all cases tested). The inlet temperature was controlled by adjusting the preheat. A similar procedure used to generate the pressure amplitude spectra in Figure 15 at the CH-04 (CUBE) location was repeated at the various other operating conditions. The peak amplitudes were extracted at the characteristic frequencies (around 350 Hz, 700 Hz, 5 kHz, and 6 kHz). The frequencies where the peaks occur vary with the operating condition but can generally be grouped into these four categories. The different frequencies are attributable to the change in sound speed with different inlet temperatures and equivalence ratio and it is unlikely that vastly different instabilities of another nature are being excited. The amplitudes are plotted for the 1L instability around 350 Hz in Figure 16, for ~700 Hz in Figure 17, for the 1T instability ~5 kHz in Figure 18, and for the 1T1L instability ~6 kHz in Figure 19.

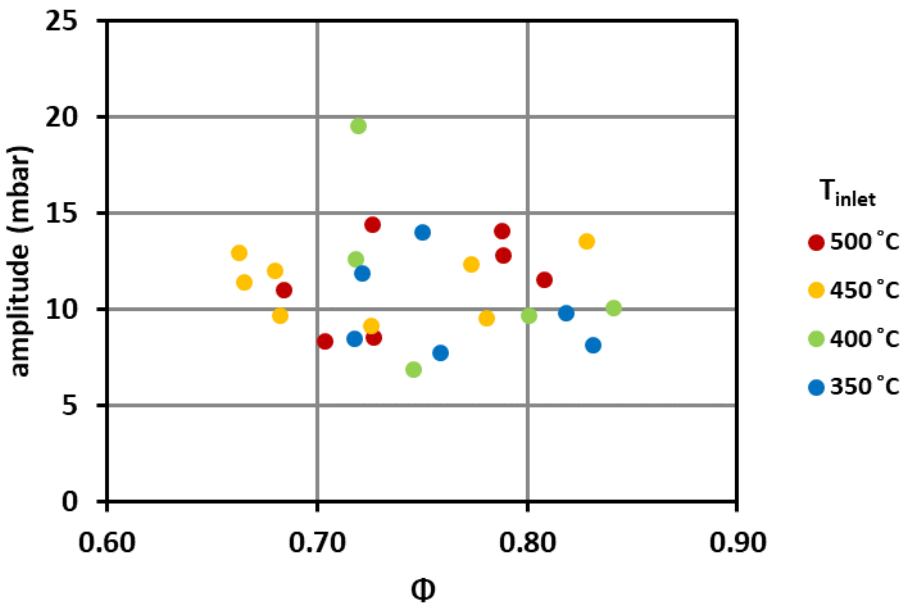

Figure 16: Pressure amplitude at~350 Hz at CH-04 location at various operating conditions

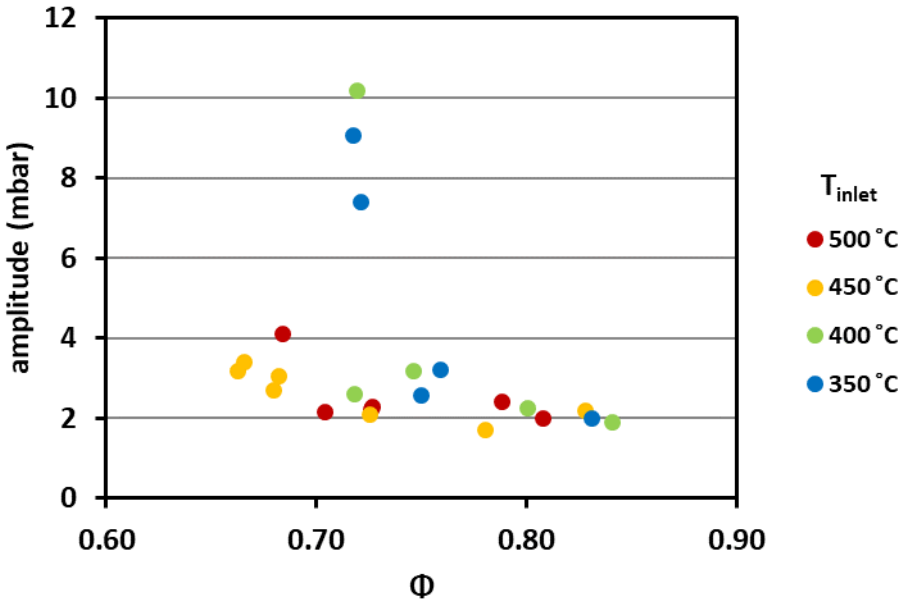

Figure 17: Pressure amplitude at~700 Hz at CH-04 location at various operating conditions

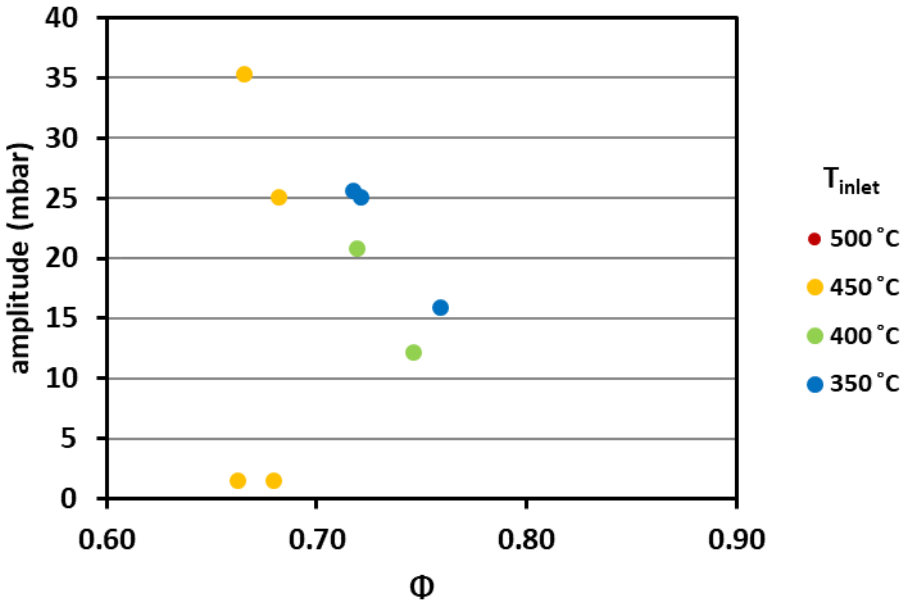

Figure 18: Pressure amplitude at~5 kHz at CH-04 location at various operating conditions

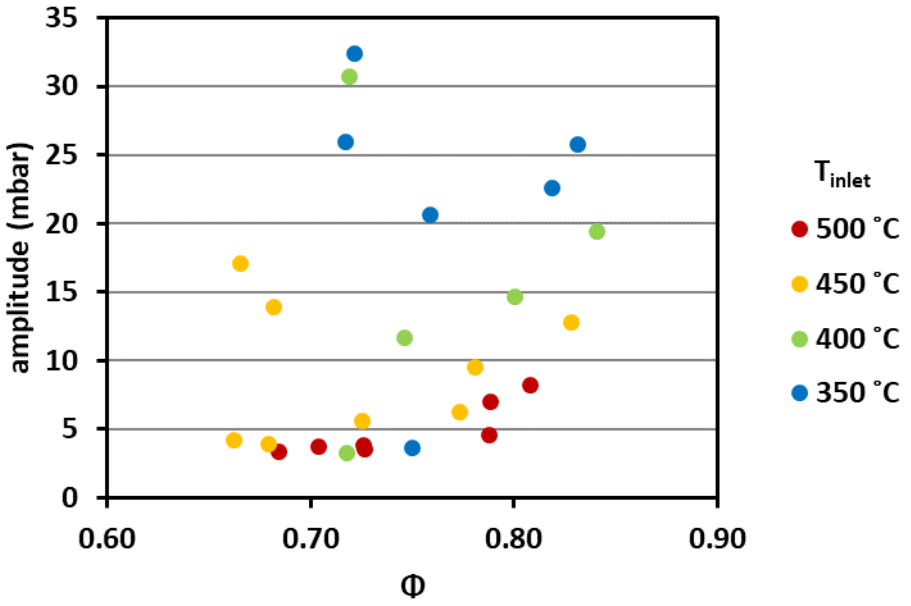

Figure 19: Pressure amplitude at~6 kHz at CH-04 location at various operating conditions

The amplitudes are plotted against the equivalence ratio on the horizontal axis. The symbols are loosely grouped and colored by the relative inlet temperature within a range of ± 25 ˚C. For example, the red circles indicate operating points with an inlet temperature exceeding 475 ˚C, the orange points correspond to an inlet temperature between 425- 475 ˚C, etc. Points are omitted when a peak in the spectrum was not clearly distinguishable, notice that only few points are plotted in Figure 18.

From Figure 16, the ~300 Hz instability is generally present at all operating condition., Although the amplitude varies between 5-20 mbar, one can say that the level of instability is similar for all cases. The variation is likely due to non-linear coupling between the 300 Hz mode and other modes, which is further supported by the observation that the highest level of instability at 300 Hz occur when the 700 Hz, 5 kHz, and 6 kHz modes are also highest. Similarly, in Figure 17, the 700 Hz amplitude is at a similar persistent level at most operation conditions except for a few points at the lower inlet temperatures.

The trends for the 5 kHz and 6 kHz modes can be roughly gleamed from Figure 18 and Figure 19. The 5 kHz mode is generally more unstable at lower equivalence ratios (the mode could not be identified at higher equivalence ratios). The 5 kHz mode was also not identifiable at the highest inlet temperatures (~ 500 ˚C). Analysis of the numerical results indicate that the 1T mode is a flame trapped mode. At higher equivalence ratios, the flame length is shorter and the axial extent of the 1T mode is less. The downstream position of the CH-04 transducer is probably unable to pick up the 5 kHz mode at the higher equivalence ratios and higher inlet temperature conditions. The trend for the 1T1L mode in Figure 19 is quite opposite the 1T mode,

with generally higher amplitudes occurring at higher equivalence ratios (although there are a number of exceptions). The reason for this trend is currently not clear. However, it is correlated with the increased thermal power at higher equivalence ratios.

The refence point at an equivalence ratio of 0.75 was chosen because this condition had peaks at all four frequencies. The peak at 5 kHz was not clearly discernable at higher equivalence ratios. Some cases near this operating condition also showed extremely high levels of instabilities.

Table 3: Pressure amplitudes at various operating points tested

#	$\dot{m}_{air}$ $\left[\frac{kg}{s}\right]$	$\dot{m}_{fuel}$ $\left[\frac{gm}{s}\right]$	Φ $[-]$	T_{inlet} $[^{\circ}C]$	f_1 $[Hz]$	$\lvert p' \rvert_1$ $[mbar]$	f_2 $[Hz]$	$\lvert p' \rvert_2$ $[mbar]$	f_3 $[Hz]$	$\lvert p' \rvert_3$ $[mbar]$	f_4 $[Hz]$	$\lvert p' \rvert_4$ $[mbar]$
1	0.52	21	0.68	499	357	11	699	4			6045	3
2	0.53	22	0.73	497	349	9	721	2			6361	4
3	0.52	22	0.73	495	359	14	699	2			6242	4
4	0.52	24	0.79	491	358	14					6295	5
5	0.52	24	0.79	487	366	13	723	2			6047	7
6	0.52	25	0.81	486	364	12	736	2			6062	8
7	0.54	22	0.70	478	361	8	713	2			6071	4
8	0.53	20	0.66	466	362	13	695	3	5165	1.5	5927	4
9	0.52	21	0.68	461	352	12	701	3	5185	1.5	5844	4
10	0.52	20	0.65	460	350	-	-	-	5297	-	5827	-
11	0.52	24	0.78	456	362	10	712	2	-	-	6084	10
12	0.52	20	0.65	456	354	-	-	-	5214	-	-	-
13	0.53	21	0.69	452	355	-	-	-	5303	-	6063	-
14	0.52	25	0.83	450	356	14	727	2	-	-	6143	13
15	0.52	24	0.77	448	324	12	-	-	-	-	5817	6
16	0.52	20	0.67	448	351	11	697	3	5248	35	5846	17
17	0.52	21	0.68	446	340	-	-	-	-	-	5878	-
18	0.53	21	0.68	445	357	10	707	3	5299	25	6026	14
19	0.53	22	0.73	445	355	9	698	2	-	-	5875	6
20	0.52	21	0.71	411	352	10	706	3	5306	28	5930	15
21	0.53	23	0.74	410	-	-	-	-	-	-	-	-

#	$\dot{m}_{air}$ $\left[\frac{kg}{s}\right]$	$\dot{m}_{fuel}$ $\left[\frac{g}{s}\right]$	Φ $[-]$	T_{inlet} $[^{\circ}C]$	f_1 $[Hz]$	$\lvert p' \rvert_1$ $[mbar]$	f_2 $[Hz]$	$\lvert p' \rvert_2$ $[mbar]$	f_3 $[Hz]$	$\lvert p' \rvert_3$ $[mbar]$	f_4 $[Hz]$	$\lvert p' \rvert_4$ $[mbar]$
22	0.53	22	0.72	402	350	13	594	3	-	-	5864	3
23	0.53	22	0.72	396	352	20	691	10	5288	21	5986	31
24	0.52	23	0.75	394	343	7	701	3	5264	12	5823	12
25	0.52	25	0.84	394	358	10	733	2	-	-	6077	19
26	0.52	24	0.80	392	353	10	710	2	-	-	5977	15
27	0.53	23	0.76	352	369	8	701	3	5193	16	5776	21
28	0.54	23	0.75	350	351	14	692	3	-	-	5845	4
29	0.53	22	0.72	350	363	9	683	9	5106	26	5650	26
30	0.53	22	0.72	350	352	12	678	7	5021	25	5830	32
31	0.53	26	0.83	350	353	8	711	2	-	-	5934	26
32	0.52	25	0.82	345	365	10	-	-	-	-	5936	23

CHAPTER THREE: LES STUDY

To supplement the experimental data, large eddy simulations were performed to provide the detailed flow-field information. Large Eddy Simulations are a numerical approach to fluid flow problems that solves the time-accurate but spatially-filtered Navier-Stokes equations. The filtered motions are directly computed so that they are temporally accurate and spatially resolved (hence they are often referred to as the resolved motions). The spatially unresolved motions are modelled using subgrid scale models. Large eddy simulations are a practical alternative to direct numerical simulations (DNS) which solve directly the unfiltered time-accurate Navier-Stokes equations. DNS requires extremely & prohibitively small cell sizes in order to resolve all the spatial scales of motions. In contrast to simulations based on the Reynolds-Averaged Navier-Stokes (RANS), the subgrid scale model in LES models only a fraction of the turbulence. RANS is a temporal filtering technique; a consequence of the temporal filtering is that there is an implicit assumption in RANS of a global separation of timescales. The consequence is that all of the turbulent velocity fluctuations (or Reynolds stresses to be precise) are modelled in a typical RANS simulation where the Boussinesq eddy viscosity hypothesis is invoked. LES is a practical compromise between the limited information available in RANS simulations versus the computational expense of DNS. Another benefit of LES over unsteady RANS is that the acoustic-hydrodynamic and coupling between flame and acoustics can be solved directly in LES (at least for the resolved scales). Excessive modelling is not attractive when the objective is to determine the underlying physical mechanisms that so-far has eluded investigators. It is possible using unsteady RANS to model thermoacoustic phenomenon if one formulates the primitive variables in RANS as the temporally coherent part of the flow (i.e. the phase-averaged velocity).

However, the flame-acoustic interaction must be prescribed in unsteady RANS using a suitable model, which presumes that the flame behavior is understood a priori. In the future, it may be possible to carry out simulations of thermoacoustic problems using unsteady RANS. Currently, there is insufficient knowledge of the dynamic flame behavior and mechanism of thermoacoustic instability to carry out these simulations. LES and other high-fidelity tools must be relied upon until these models have been formulated.

Just as experimenters have the choice of providing external acoustic forcing in their experiments, these options are also available numerically. In situations where the actual experiment is forced, it makes sense to adopt the same procedure and provide the same forcing in the numerical simulation. Forced excitation in LES is still often performed when there are difficulties obtaining self-excited instabilities, when the acoustic boundary conditions of the actual hardware are complex (or unknown), or when the domain has been oversimplified. Only a section of the experimental hardware is modeled in the numerical study, the truncated rig segment is depicted in Figure 20. The LES is un-forced and self-excited, similar to the VIPER-S experiment.

Computational Mesh

The actual computational domain considered in this study is depicted in Figure 21, involving only the primary combustion flow path. The domain consists of a 720 mm length circular pipe of 40 mm diameter, followed by a 1162 mm length of 80 mm diameter pipe. The domain is terminated in an elliptic contoured nozzle with an exit throat diameter of 33.22 mm (1.308 in) matching the exit nozzle used in the VIPER-S rig setup.

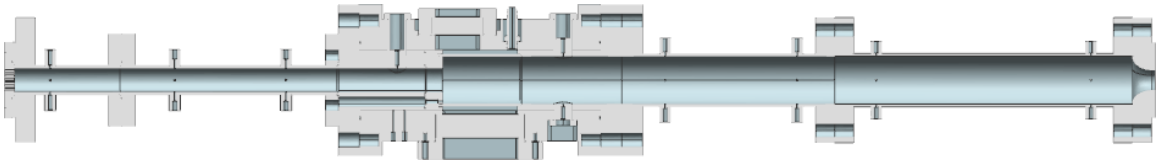

Figure 20: Modeled rig segment for LES study

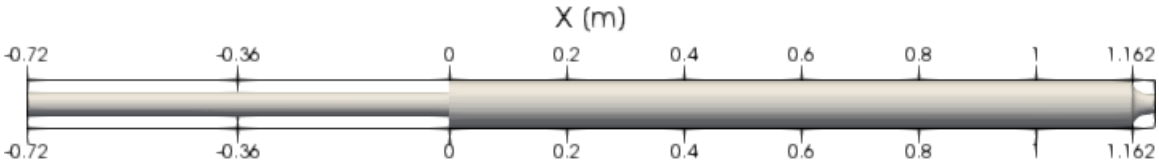

Figure 21 Computational domain

The multi-hole orifice plate from the experiment is not simulated and is modeled as a uniform inlet. The inlet of the computational domain is circular in cross-section. The orifice plate and upstream mixing section from the experiment are not included in the computational model. Estimations based on non-reacting CFD of the mixing section suggests the fuel-air mixture is well-mixed at the entrance to the orifice plate. The orifice plate provides a choked boundary condition. The 720 mm inlet duct is 18 diameters long, long enough for the velocity boundary layer to be presumed to be fully developed by the dump plane. For turbulent flows in pipes, the boundary layer is typically considered to be fully developed after roughly 10 diameters. Thus, neglecting the orifice plate geometry and using a simple circular inlet in the numerical model is likely not crass. Neglecting the upstream mixing section has an advantage of significant savings in computational cost due to the reduced geometry; a perfectly premixed model may also be applied, and the fuel-air mixture can be treated as a homogeneous substance.

The computational domain is terminated at the end of the exit nozzle. The long exhaust duct (a few meters length) which eventually dumps the hot combustion products into the ambient

environment is not modeled. Since the flow in the exit nozzle is choked, it is not expected to have any impact on any of the results in this study.

Only the flow regions are modeled from the experimental setup. The surfaces are treated as thermally adiabatic everywhere and the thicknesses of the solid walls are not included in the model. A conjugate heat transfer analysis was not performed.

Tay-Wo-Chong & Polifke [82] used LES to study the impact of different thermal boundary conditions and effect of confinement on the flame transfer function of a perfectly premixed axial swirl burner. They found that these boundary conditions had a noticeable impact on the flame response due to the different resulting flow field and flame shape produced. The adiabatic wall produced a flame with significant heat release in both the inner and outer shear walls. In their case, the different boundary conditions lead to a very different flame configuration and thereby resulted in a different flame response. For an unswirled premixed jet flame, there is no inner/outer recirculation and the flame stabilization mechanism does not change. Thus, the VIPER configuration should be less susceptible to variations in wall thermal wall boundary conditions than other configurations.

A purely hexahedral mesh was generated using GridPro v6.6 by Program Development Company. GridPro forms unstructured arrangement of blocks (the individual blocks are structured). The user defines the grid topology and number of cell divisions along edges of blocks. The GridPro algorithms then performs optimization to automatically generate a smooth grid with high orthogonal quality, resulting in curvilinear-style grids. The mesh near the dump plane is depicted in Figure 22. Visible in Figure 22 in the mesh is the grid pattern in the 40 mm

diameter as well as the 80 mm diameter combustion chamber. The grid structure is similar upstream and for the length of the combustion chamber. The mesh near the exit nozzle is depicted in Figure 23. The cross-sectional views of the mesh are given at the inlet and outlet in Figure 24 and Figure 25, respectively. Wall clustering is applied to better resolve the near wall flow. A grid stretch ratio is 1.05 and wall cell height is on the order of 0.4 mm (0.2 mm for the fine grid) on all walls (the pre-mixing duct, baseplate, combustion chamber, and exit nozzle).

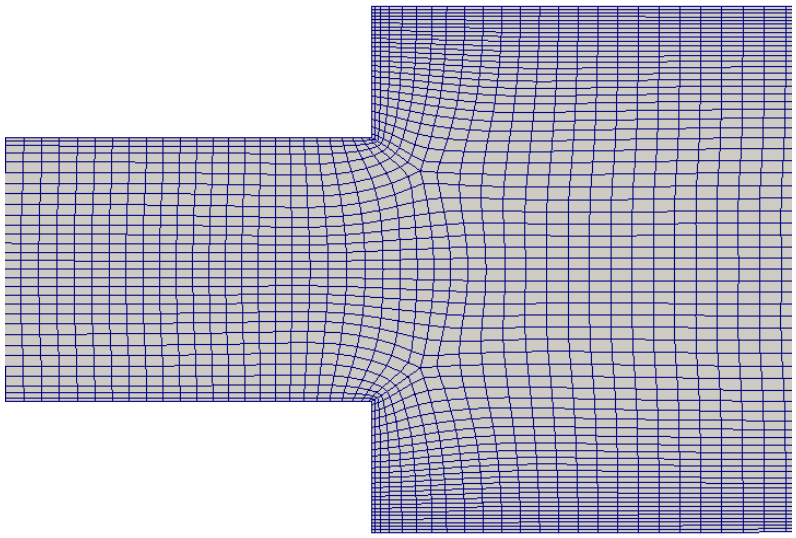

Figure 22 Slice of computational mesh near dump plane

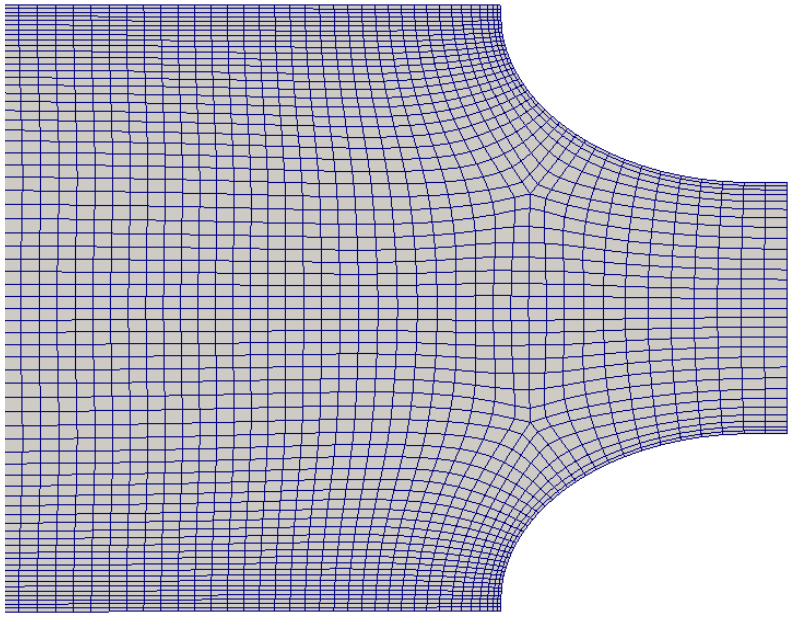

Figure 23 Slice of computational mesh at exit nozzle

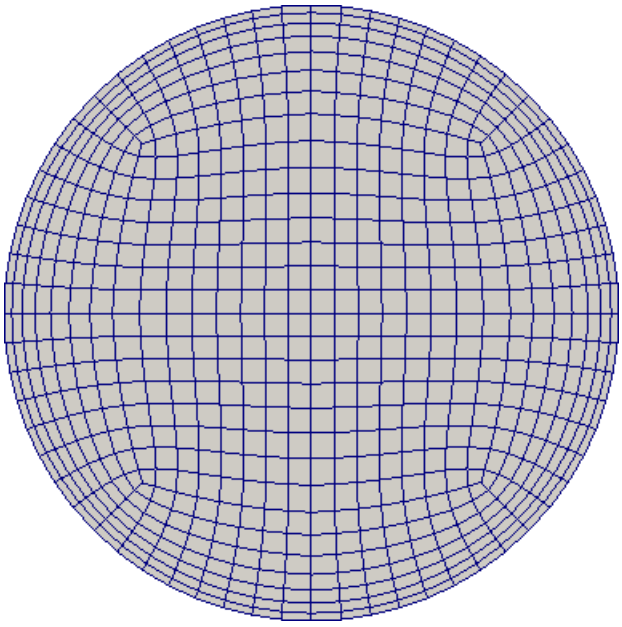

Figure 24 View of mesh at inlet boundary

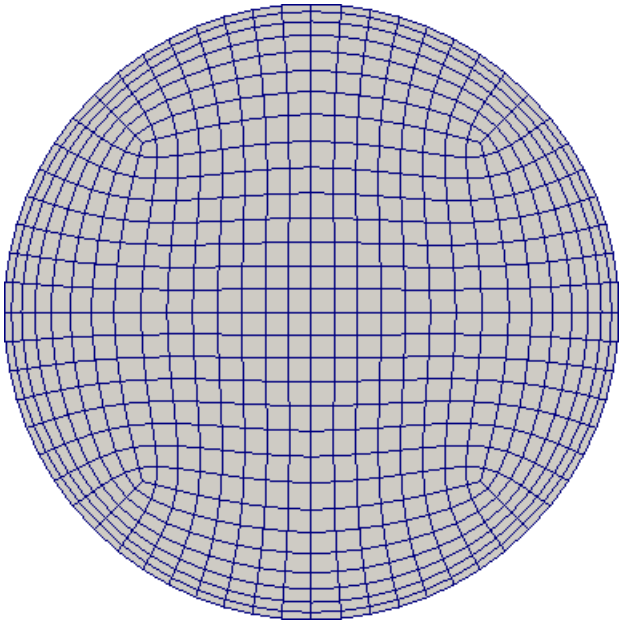

Figure 25 View of mesh at outlet boundary

To study the mesh sensitivity, two denser grids were generated with a similar topology. The nominal cell size in the axial direction was halved for the medium grid. The number of cells per circumference was also doubled for with the density change. Table 4 lists the key mesh metrics for each grid type along with the total hexahedral cell count. If the number of divisions on each edge of a cube are doubled then the total cell count would increase by a factor of 2^3=8. The cell count does not increase by a factor of x8 with each density level due to the topology of the block arrangement. The baseline case, from which most of the analysis was performed on, is the coarser grid with approximately 700 000 cells.

Table 4: Summary of mesh grades

Relative Density	Cell Count	Nominal Δx	# cells / circumference
Baseline	715,264	4mm	64
Medium	3,218,072	2mm	128

Numerical Model & Methods

The large eddy simulations were carried out using OpenFOAM v2.4. The packaged XiFOAM solver is an unsteady RANS-based solver using the b-Ξ combustion model and not directly suitable for LES. For carrying out LES, the wrinkled flame model of Weller et al. [83] is implemented, using XiFOAM as a basis, in a Siemens in-house custom solver.

One of the model inputs is the unstrained laminar flame speed of the mixture, which is calculated using Gene-AC and GRIMECH 3.0. The combustion chemistry is defined by GRIMECH 3.0. The fuel composition is taken from the daily average of gas chromatograms taken by the PEPL utility and is used to compute the burning velocity. The estimated laminar flame speed for the reference case is 598 cm/s.

The Crank-Nicolson scheme is used for the temporal discretization with an off-centering coefficient of 0.9. An off-centering coefficient of 0 corresponds to a pure first order upwind scheme and a coefficient 1 corresponds to a pure Crank-Nicolson scheme. A greater off-centering coefficient tends towards higher accuracy but is also prone to numerical oscillations. A time-step size of 0.2 μs is used which corresponds to a maximum acoustic Courant number of approximate 0.85 on the coarse grid. The average Courant number is 0.25. The PIMPLE (merged

PISO-SIMPLE) algorithm is used with nOutCorrectors set to 3 (3 iterations per time-step). Underrelaxation factors for pressure and velocity are 0.9 for the SIMPLE steps and 1 for the final PISO steps. All other underrelaxation factors are 1.

The advective term for momentum is discretized using the filteredLinear2V 0.5 0 scheme. The first coefficient, when 0 is fully linear and when 1 is fully limited. The 2nd coefficient set to 0 means no overshoots. The other advective quantities are discretized using a the fully limited limitedLinear 1 scheme (bounded central differencing scheme). Diffusive fluxes are discretized using a linear scheme.

Boundary Conditions

For the model setup used, boundary conditions are needed for pressure, velocity, temperature, reaction regress variable, flame wrinkling factor, as well as the subgrid-scale kinetic energy. Additional trivial boundary conditions are needed for the subgrid-scale viscosity and diffusivity which are set to the molecular quantities. The regress variable (b) at the inlet is 1 (for a completely unburned mixture). The inlet boundary condition for the flame-wrinkling factor is 1 (no strain at the inlet). The inlet pressure boundary condition is the zero-gradient type. The inlet velocity is uniform and calculated to achieve the desired targeted total massflow rate of the premixed air-fuel mixture (0.550, 0.553, & 0.556 kg/s for the Φ=0.65,0.75, and 0.85, respectively). The inlet temperature is 680K for the baseline case but set to 675K for Φ=0.85 and set to 685K for Φ=0.65 cases. The small change in temperature is to account for the mixing between the pre-heated air (nominally at the same temperature) mixed with different quantities of cold (ambient temperature) natural gas fuel. Two additional cases are also simulated for

Φ=0.75 at reduced pre-heat temperatures by reducing the inlet temperature to 635K and 590 K. These boundary condition combinations follow the parametric survey in VIPER-S experiment, where the air flow rate was nominally fixed to 0.53 kg/s; the natural gas flow rate was adjusted to alter the equivalence ratio and air pre-heat temperature was varied between 300-500 ˚C.

The boundary condition at the outlet for all variables except pressure is of the outflow type or zero gradient type. For the pressure boundary condition, a Siemens proprietary implementation of an acoustic non-reflecting boundary condition is used. The implementation is based the methodology developed by Polifke et al.[84]. This approach is often referred to as the NSCBC (Navier-Stokes characteristic boundary condition) approach. The ambient pressure setting is 1 atm (101 325 Pa) and a timescale factor of 0.01 is used for all cases.

The zero gradient boundary condition for pressure corresponds to an acoustic pressure anti-node at the inlet. The fixed flowrate boundary condition in principle should correspond (nominally) to a velocity node (except that density fluctuations can allow some velocity fluctuations). In practical, the fixed flowrate boundary condition behaves closer to an acoustically non-reflecting boundary than a fully reflecting boundary.

On walls, zero gradient boundary conditions were applied for pressure, temperature, regress variable, & wrinkling factor. The no-slip boundary condition were applied for velocity on walls. Suitable wall functions were applied for the subgrid-scale kinetic and turbulent viscosity.

In VIPER, the flow in the exit nozzle is choked (which is acoustically reflecting). The flow-path through the nozzle is also a small bore in a larger flange. Thus, the acoustic condition near the rig outlet is a combination of reflection off solid surfaces and a reflection near the throat

of the nozzle. The distance between the nozzle throat to the exit flange is small compared to the wavelength of the acoustic modes so that the exit nozzle is acoustically compact. Because the flow in the exit nozzle is choked at the outlet, the pressure boundary condition at the exit is not important numerically.

Data Sampling

Fields are sampled globally at every time-step for mean and rms statistics. For post-processing, selected data are sampled from individual points and on characteristic planes. The locations of the point probes are listed in Table 5, shown diagrammatically in Figure 26. The point names and locations are consistent with the relative placement of the high frequency pressure transducers from the VIPER-S experiments. Results are sampled on the mid-plane (Z=0) and at a cross-sectional cut of the domain downstream of the dump plane (at X = 160 mm). The CUBE and BP (baseplate) locations are the most indicative of the tangential acoustic modes. The CH-# measurements are similar to the CUBE measurements but are located slightly downstream. The PD-0# locations give information on the acoustic characteristics in the premixing duct. The AFT location is nearest the pressure anti-node of any longitudinal modes. The most upstream measurement location in the combustion chamber is the CUBE location, which is 293 mm downstream of the dump plane, the AFT location is 70 mm from the start of the exit nozzle.

Table 5: Summary of point probe locations (Table 2 + BP-04 probe added)

Probe Name	Coordinates (x y z) [m m m]
CUBE	(0.2930, 0.0000, 0.0400)
AFT	(1.0920, 0.0000, 0.0400)
CH-01A	(0.3750, 0.0000, 0.0400)
CH-01B	(0.3750, 0.0000, -0.0400)
CH-01C	(0.3750, -0.02820, 0.02820)
PD-01	(-0.6600, 0.0000, 0.0200)
PD-02	(-0.4510, 0.0000, 0.0200)
PD-03	(-0.0760, 0.0000, 0.0200)
BP-01	(0.0000, 0.0000, 0.03556)
BP-02	(0.0000, 0.03556, 0.0000)
BP-03	(0.0000, 0.0000, -0.03556)
BP-04	(0.0000, -0.03556, 0.0000)

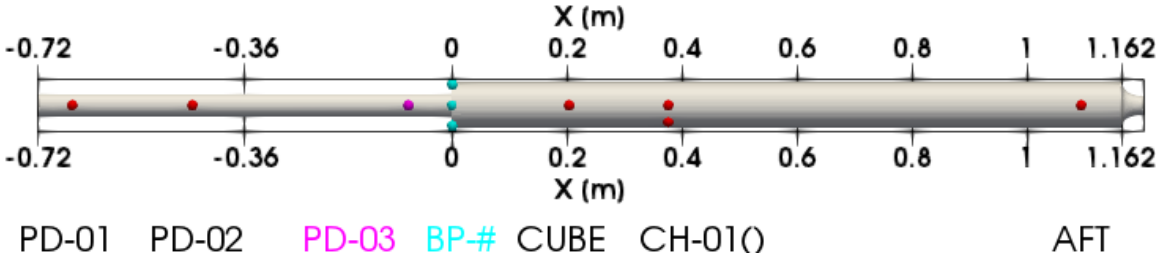

Figure 26: Schematic of probe sampling locations for data extracted from LES

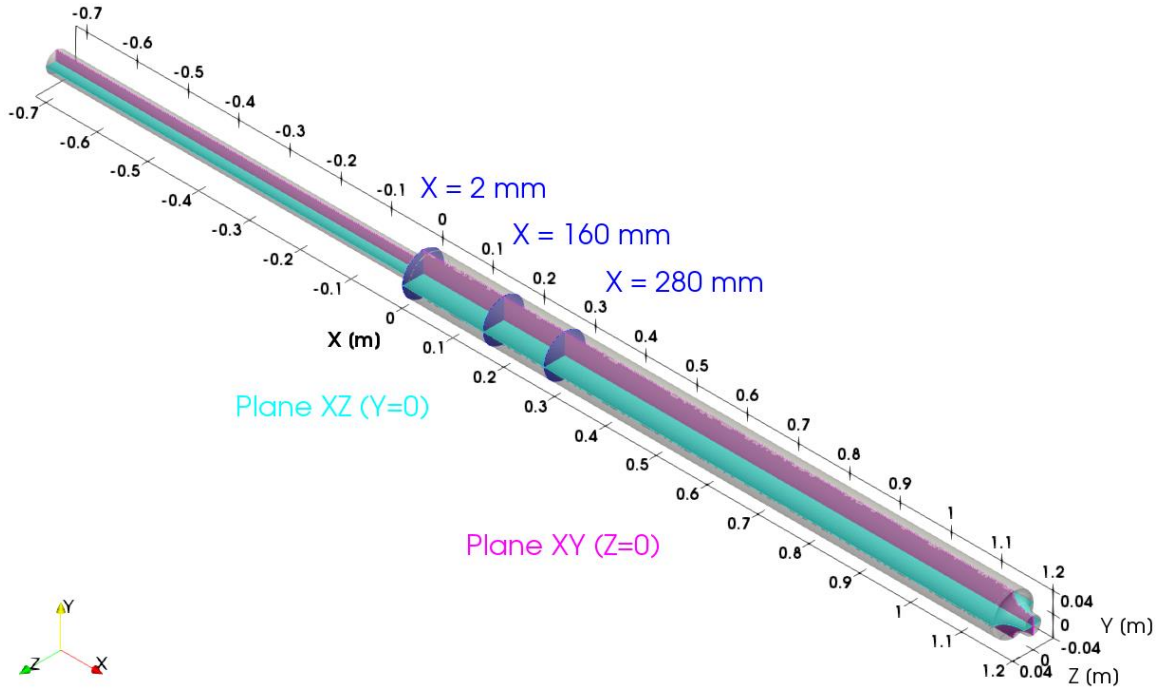

Figure 27: Schematic of plane sampling locations for data extracted from LES

Calculations were carried out primarily on the Siemens in-house compute cluster located in Orlando, FL. The Orlando compute grid, for CFD usage, consists of 448 nodes dual socket tetradeca-cores (2x14 cores per node). A typical calculation on the baseline grid was run on 10 nodes (280 processes). The typical run could calculate 100 ms of solution time in roughly 24 hours of physical time (~ 1 compute year per 100 ms). Mean fields were averaged (using every time step) over a duration of 100 ms. which is more than 500 acoustic cycles of the transverse modes.

Although the LES is time-accurate, Fourier analysis does not scale linearly with the number of samples. Even when accelerated using a fast Fourier transform (FFT), the calculation of the discrete Fourier transform (FFT) is still at best $O(n \log n)$ compared to the $O(n^2)$ of calculating the FFT directly. Hence, even when disk storage is not limiting, significant economy in the subsequent analysis is achievable through sub-sampling. Point probes are sampled every 5 time-steps (a sampling frequency of 1 MHz), yielding a signal length of 100,000 samples.

Reference Case

It is helpful to describe the characteristics of a configuration completely for at least a single reference case. Comparisons of the behavior at different operating conditions (or boundary conditions) or even comparisons between simulations run with different settings are more easily facilitated by comparison of same probe across different simulations. In this sub-section, the spectra for all the probes listed in Table 5 are presented in detail for only the reference case.

The reference case selected is the case with an inlet mass flow rate of 0.553 kg/s (0.53 kg/s of air + 23 g/s of natural gas) and inlet gas temperature of 680 K (the mixed temperature of 723 K air with 300 K natural gas). This mixture ratio corresponds to an equivalence ratio of 0.75.

Time-averaged Fields

Although they contain no information on the fluctuating fields needed to assess the dynamic effects of acoustics and turbulence, the mean (time-averaged) fields are critical to establish a benchmark for the mean state of the system. The mean pressure on the Y=0 plane is presented in Figure 28. The mean pressure is nominally 7.2 bar and does not vary significantly compared to the rapid decrease in static pressure as the flow accelerates and passes through the sonic nozzle at the exit. The mean pressure of 7.2 bar is slightly higher than the value of 6.8 bar measured experimentally for a similar condition. The discrepancy is due to a combination of modeling effects (deviations of the material properties applied numerically from real-world properties) and the exit nozzle. The combustion chamber pressure is not imposed as a boundary condition in the numerical simulation, only the rig mass flow rate is applied at the inlet. The chamber pressure adopts its value based on the flow through the choked exit nozzle (this phenomenon occurs in both the numerical simulation and the VIPER experiment). Therefore, any inaccuracies in the choked flow processes occurring at the exit nozzle will impact the combustion chamber pressure. In the numerical simulation, the computational domain is terminated at the end of the sonic nozzle throat, and the flow expansion into the exhaust piping is not calculated. The numerical grid is not fine enough to resolve the wall boundary layer in the exit nozzle (the boundary layer accelerates the flow through the sonic nozzle). It is expected that the discrepancy between the mean pressures can be remedied by improving the modeling efforts.

However, the deviation in the mean chamber pressure should not invalidate the findings presented here.

The mean reaction regress variable is presented in Figure 29. The regress variable is 1 in the unburnt region and 0 in the burnt region. Intermediate values of the regress variable highlight the burning zone. The tapered shape of the regress variable field is typical of unswirled jet flames; it can be determined from Figure 29 that the flame length is on the order of 30 to 40 cm (8-10 jet diameters). The mean temperature field is shown in Figure 30 which closely resembles the regress variable field. The temperature is slightly lower than 680 K in the premixing duct due compressible flow effects and reaches a temperature of 2100-2200K in the post-flame region. Consequently, the mean density field is plotted in Figure 31 which also resembles the regress variable and temperature fields (due to the pressure field variation being negligible).

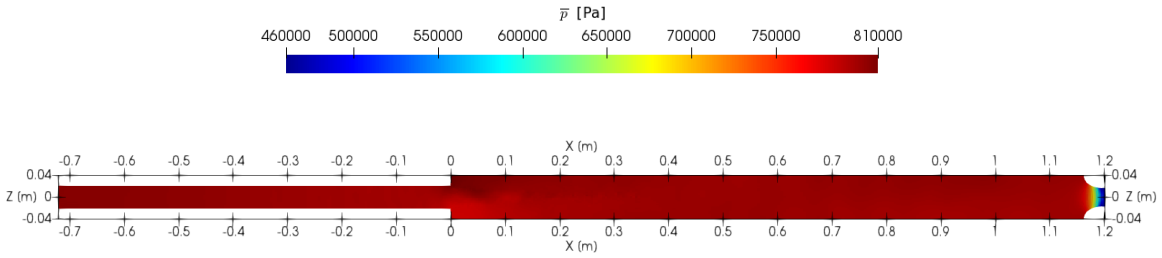

Figure 28: Mean pressure (p) field on XZ-plane

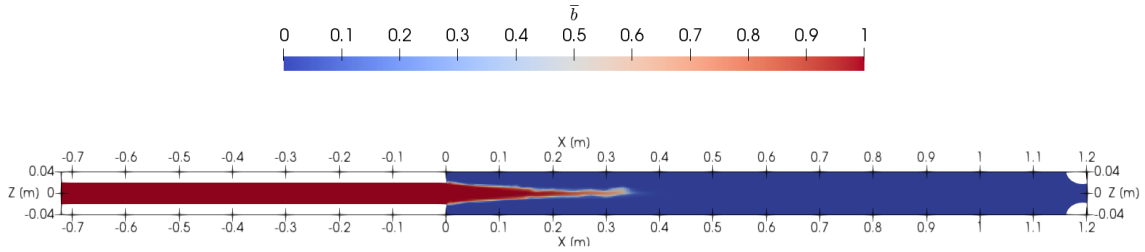

Figure 29: Mean reaction regress variable (b) field on XZ-plane

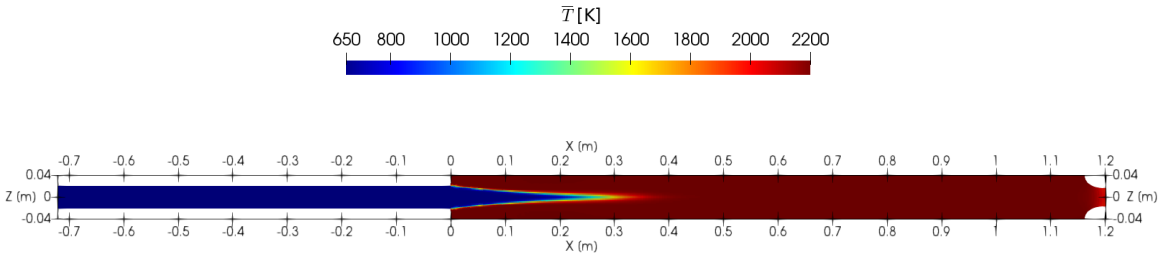

Figure 30: Mean temperature (T) field on XZ-plane

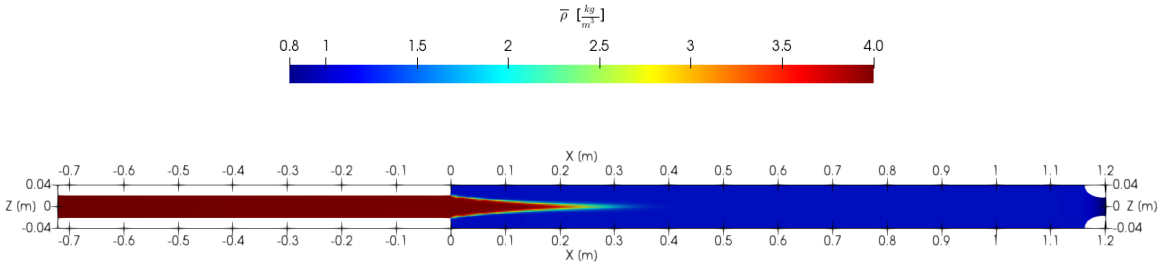

Figure 31: Mean density field (ρ) on XZ-plane

Constant-Q Transform

Monitoring the temporal development of acoustic signals is important to verify that the acoustics are statistically stationary. A time-series plot showing a nearly constant peak-to-peak amplitude is usually a quick visual indicator that the system has reached a limit-cycle condition. That is, the unstable modes (if any) are not growing and/or decaying. However, in a raw time-series plot of a signal, it is difficult to differentiate the strength of individual frequencies. The FFT of a signal, while capable of providing the amplitude at each frequency, maps the entire signal onto a single spectrum. The entire time-series is incorporated into a single FFT.

Spectrograms provide a representation of the frequencies in a signal and how the frequencies (and their amplitudes) vary with time. A spectrogram can be generated by splitting the data into time-segments (they can be overlapped and windowed, if desired) and calculating the FFT on the segments; the magnitude and frequency spectrum of each segment provides the amplitude for each frequency at each given moment in time (usually taken to be the center of the time-segment).

A disadvantage of constructing a spectrogram using regular FFT's is that the bandwidth is constant for each frequency bin, resulting in a different Q-factor for each bin. Brown introduced a method to generate a spectrogram with the constant Q-factor for each frequency bin, the so-called Constant-Q transform [85, 86]. Since the Constant-Q transform was developed for musical applications, it is often plotted on a logarithmic-frequency scale; the frequencies are spaced apart exponentially in the Constant-Q transform method (compared to the constant spacing of the FFT). A log-frequency representation has the visual benefit that harmonics of

signals are equally spaced apart. Although a linear-frequency FFT can be mapped onto a log-frequency plot, the linear-frequency FFT has fewer bins at low frequencies and more bins are higher frequencies compared to the Constant-Q transform.

The pressure at the CUBE location for a 100 ms simulation duration is assessed. The raw pressure trace is in Figure 32. Recall that the results are sub-sampled compared to the time-step of the LES, but the temporal resolution is sufficient to resolve the acoustic time-scales. The left vertical axis is the absolute static pressure in units of mbar. The right vertical axis is the deviation of the pressure from the mean. The mean pressure is 7.88 bar. The maximum pressure and minimum pressure in this interval is 8.5 bar and 7.3 bar, respectively; the peak-to-peak amplitude (maximum to minimum) is therefore 1.2 bar. From the pressure trace, it is evident there are both high and low frequency oscillations present in the signal. Approximately 4-5 cycles of a low frequency oscillation can be determined based on the envelope of the pressure trace. Upon inspection, the envelope of the low-frequency oscillation appears to be consistent over the duration, suggesting that the oscillations are stationary. Using only human eye-vision (i.e. assessing only the raw pressure trace), only the quality of the low frequency oscillations can easily be determined, and these are subject to beat frequency effects. That is, the constructive and destructive interference of several high frequency phenomenon can result in beat frequencies, their interaction appears as an envelope in the time-trace at the difference in their frequencies. The (actual) high frequency oscillations are embedded in the pressure trace, but difficult to process without additional tools & methods of presentation. Furthermore, it is difficult to determine how many high distinct high frequency oscillations are present. Fourier analysis (or frequency domain analysis) is therefore a vital tool to processing acoustic results.

Figure 33 is a spectrogram calculated using the Constant-Q transform method. The horizontal axis is the time at the center of each segment. The frequencies are labeled on the vertical axis and the plot is colored by the amplitude of the frequency bin. Signals with constant frequency and amplitude appear as horizontal stripes in the spectrogram, an example is the 500 Hz stripe. A thick red band occurs around the frequency range of interest, in the vicinity of 6 kHz. Unlike the 500 Hz stripe, the band near 6 kHz is spotty, indicating short periods of growth and decay. It will be evident from the FFT of the signal that multiple distinct frequencies are present in this vicinity. A possible explanation could be non-linear interactions between different frequencies (where one weakening frequency feeds energy and strengthens another frequency); and these interactions occur in tandem for multiple pairs of frequencies. A complete understanding of these interactions is well-beyond the scope of the current study. However, it is pertinent to highlight the complexities of self-excited studies where multiple frequencies are excited; and also, to note that the acoustic instabilities in industrial hardware are also self-excited and also exhibit a plethora of excited frequencies.

Only once the signals appear as stripes or bands the spectrogram can the frequencies be considered stationary. Otherwise, the oscillations at those frequencies would be growing or decaying in time. Although the envelope shape can yield information with regards to the growth-rate or decay-rate, Fourier amplitudes are not appropriate for growing/decaying signals. Having inspected the spectrogram, additional confidence is established to proceed with FFT analysis.

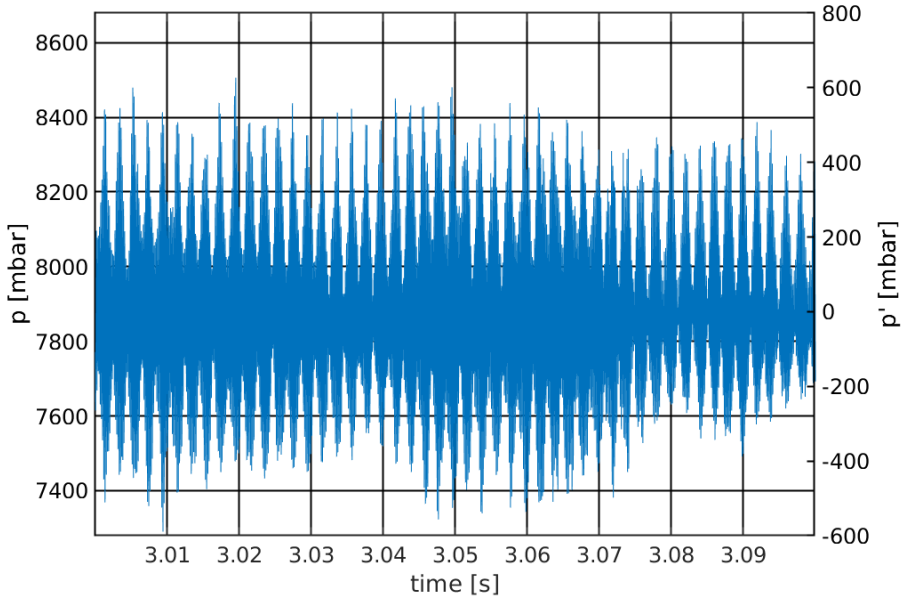

Figure 32: Pressure timetrace at CUBE location for inlet temperature of 680K and Φ= 0.75

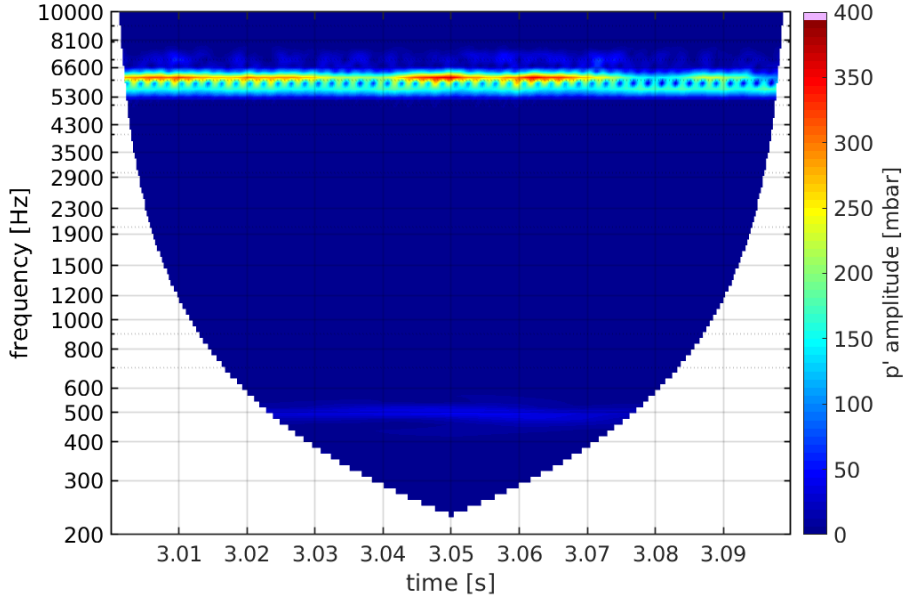

Figure 33: Spectrogram at CUBE location for inlet temperature of 680K and Φ= 0.75

Pressure Amplitude Spectra

The single-sided amplitude spectrum of the same signal from Figure 32 is presented in Figure 34. The calculation was performed in MATLAB using 2*fft(S)/length(S), where S is the pressure signal vector. The signal length of 100 ms (at a sampling frequency of 1 MHz) yields a frequency bin resolution of 10Hz when performing an FFT. Although the Nyquist cut-off frequency is at 500 kHz, the spectrum is plotted only up to 10 kHz to focus on the frequencies of interest. The most notable peaks in the Fourier spectrum are 34 mbar at 500 Hz, 125 mbar at 5590 Hz, 238 mbar at 6090 Hz.

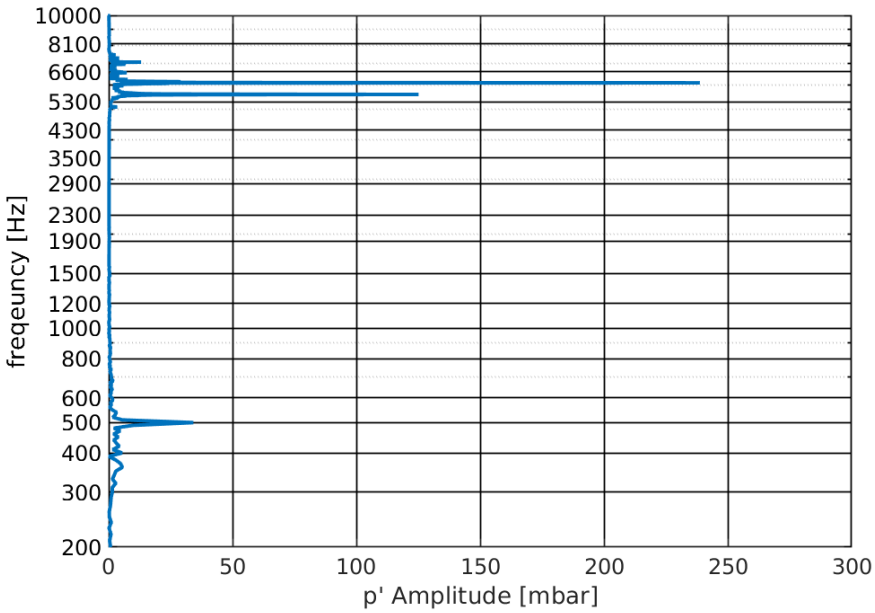

Figure 34: FFT at CUBE location for inlet temperature of 680K and Φ= 0.75

The amplitude spectra when calculated using this method (taking 2*fft(S)/length(S) without any averaging and without any filtering) is a poor estimator for the general spectrum (it is the statistical equivalent to a single sample estimate of a population parameter). However, this

method is preferred as it is unambiguous. The entire signal length is used always at the sampling frequency, with the highest Nyquist frequency and minimum bin resolution. Although windowing and averaging provide better statistics of the amplitude spectrum, a simple FFT approach is sufficient when the objective is to identify the presence of peaks and gauge their relative amplitudes. However, it should be noted that the amplitude spectra are sensitive to the input signal quality and the amplitudes have relatively high uncertainties due to not applying any statistical averaging.

Figure 35, Figure 36, and Figure 37 are similar plots of the FFT but in the premixing duct for PD-03, PD-02, and PD-01 respectively. For all three of the probes in the premixing duct, there is only a strong peak at 500 Hz; the 5600 Hz and 6090 Hz modes do not appear in the premixing duct.

The four probes on the baseplate at the dump plane are presented in Figure 38, Figure 39, Figure 40, & Figure 41. A 500 Hz peak is detected in all four BP locations with amplitudes around 20 mbar. BP-01 and BP-03 have similar content, showing strong peaks at 5600 Hz, 6090 Hz, and 6590 Hz in the order of dominance (with amplitudes of 485 mbar, 210mbar, and 50 mbar respectively). On the other hand, BP-02 and BP-04 also have similar content to each other, but much weaker signal amplitudes compared to BP-01 and BP-03. The 5600 Hz peak has an amplitude of only ~25 mbar, compared to the 490 mbar at BP-01 and BP-03. Instead of a 6090 Hz or 6590 Hz peak, instead a peak at 6300 Hz found at the BP-02 and BP-04 locations.

The amplitude spectrum for probes at locations labeled CH-01A, CH-01B, and CH-01C are depicted in Figure 42, Figure 43, and Figure 44 respectively; all three CH-01 probes the same

dominant frequencies of 500 Hz, 6090 Hz, and 6590 Hz. The strength of the 500 Hz frequency is the same 17 mbar for all three probes. There is a peak of 29 mbar at 6090 Hz and 91 mbar at 6590 Hz for CH-01A and CH-01B; the same signals at the CH-01C location is slightly weaker, 20mbar at 6090 Hz and 58 mbar at 6590 Hz. The probes at the CH-01 locations are just slightly downstream of the CUBE location.

The FFT for the AFT location is presented in Figure 45 showing 18 mbar at 500 Hz and 30mbar at 6610 Hz. The 5600 Hz and 6090 Hz frequencies are not observed at the AFT location. sThe 500 Hz frequency is found throughout, it also has consistent amplitudes at all the BP locations and CH-01 locations, which suggests that the 500 Hz frequency is a longitudinal mode (if it is an acoustic mode). The 5600 Hz and 6090 Hz frequencies do not appear in the premixing duct or in the AFT section of the rig; the 5600 Hz mode is limited to only near the baseplate and cube location, even more so than the 6090 Hz frequency.

Compared to the CUBE location, the BP-# locations all have higher amplitude for the high frequency peaks. On the other hand, whereas the CUBE showed the strongest peak at 6090 Hz, the 5600 Hz peak was the strongest for the BP-# locations. The 5600 Hz peak is also much greater at the BP locations than the CUBE. It demonstrated in subsequent chapters that this feature a result of the axial extent of the acoustic modes and its orientation in the theta direction (from eigenmode analysis in COMSOL and phase-averaging of the fluctuating pressure).

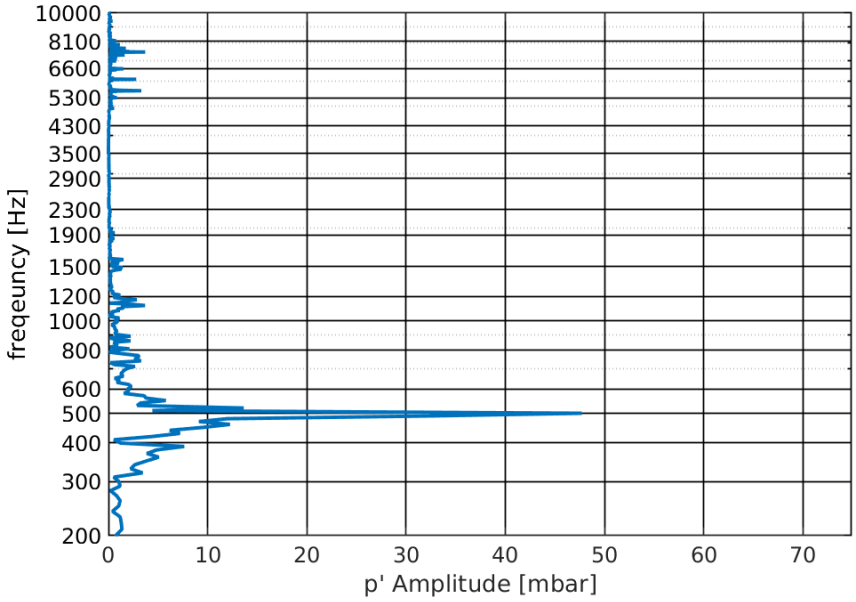

Figure 35: FFT at PD-03 location for inlet temperature of 680K and Φ= 0.75

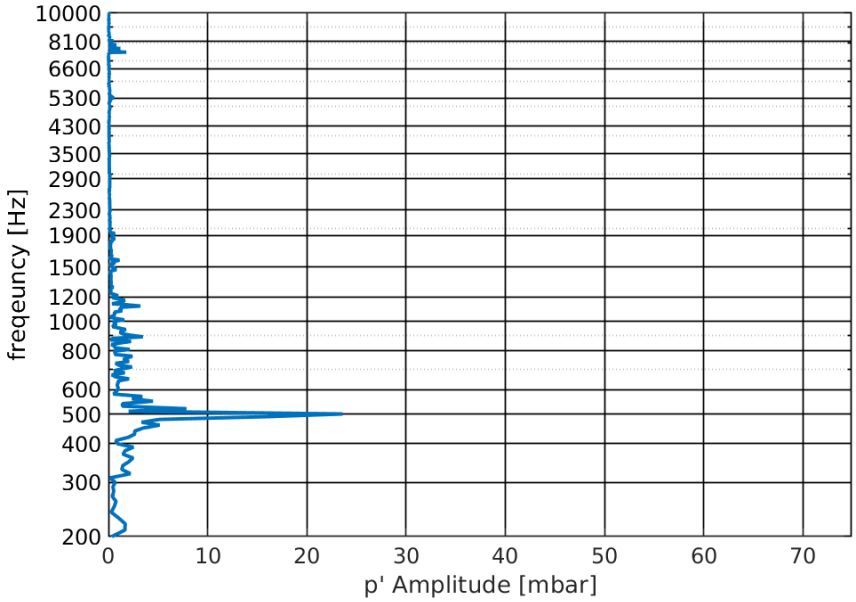

Figure 36: FFT at PD-02 location for inlet temperature of 680K and Φ= 0.75

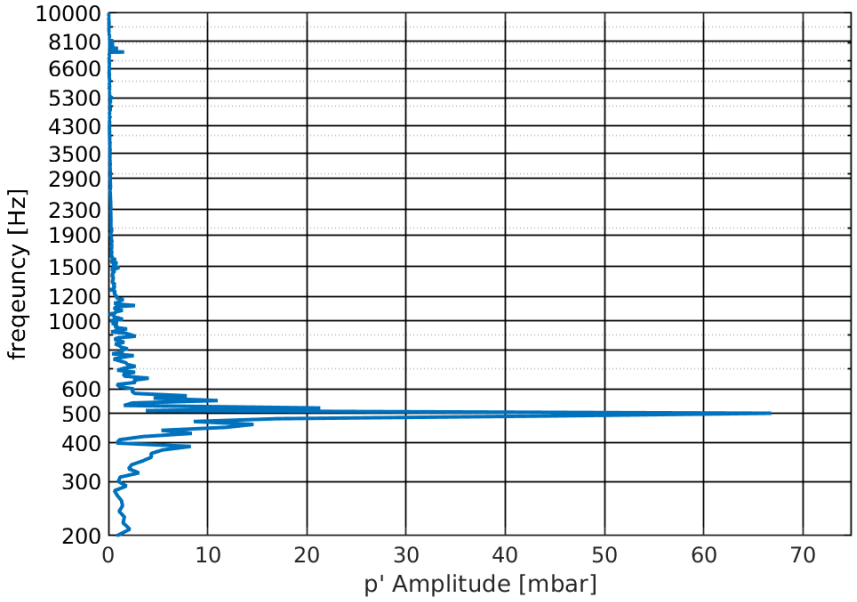

Figure 37: FFT at PD-01 location for inlet temperature of 680K and Φ= 0.75

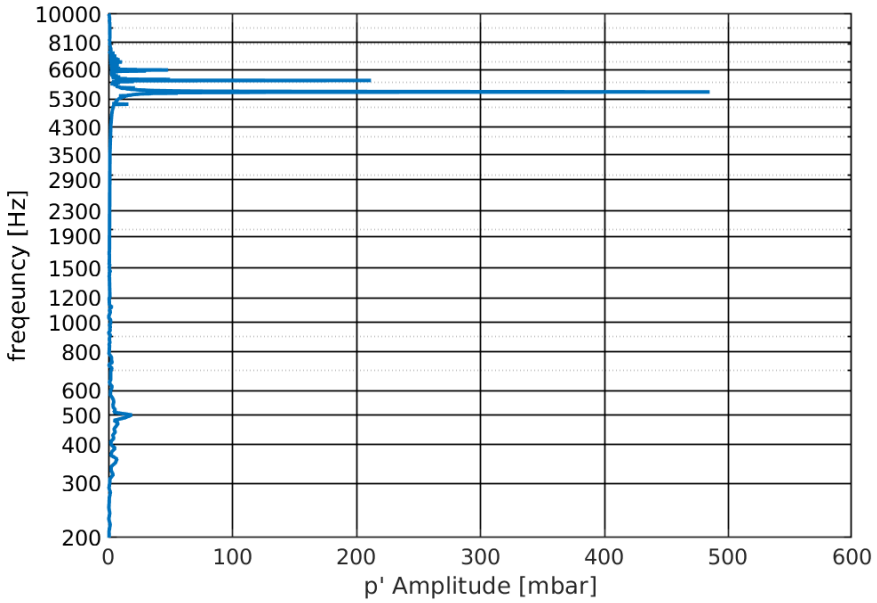

Figure 38: FFT at BP-01 location for inlet temperature of 680K and Φ= 0.75

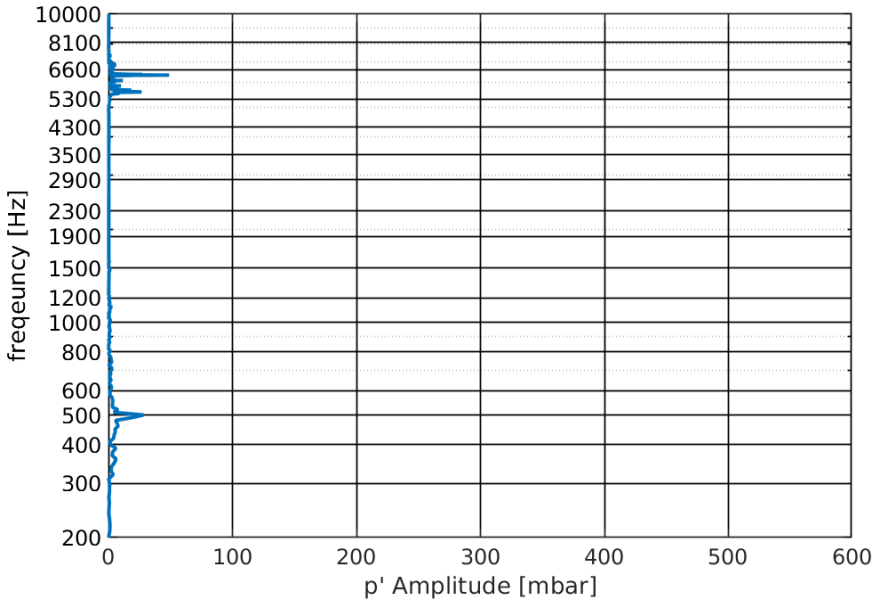

Figure 39: FFT at BP-02 location for inlet temperature of 680K and Φ= 0.75

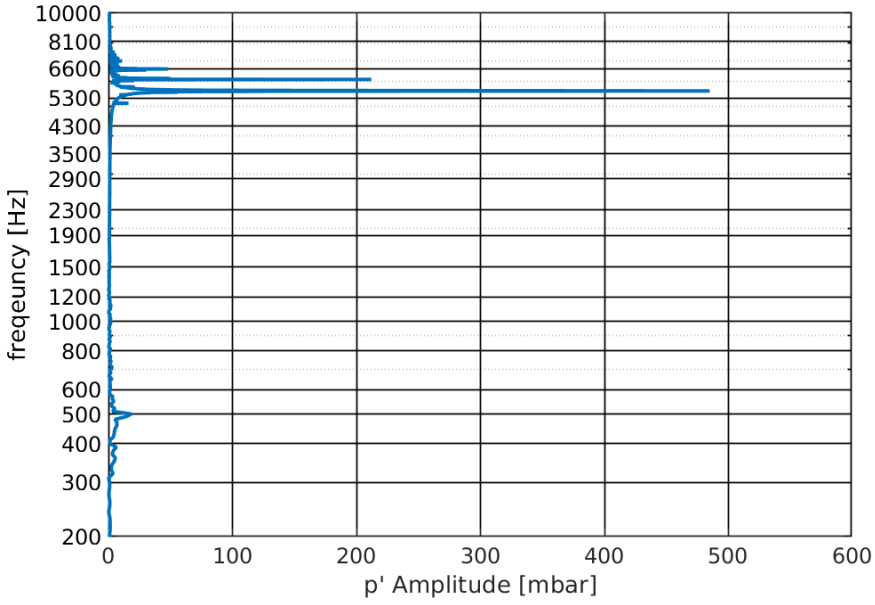

Figure 40: FFT at BP-03 location for inlet temperature of 680K and Φ= 0.75

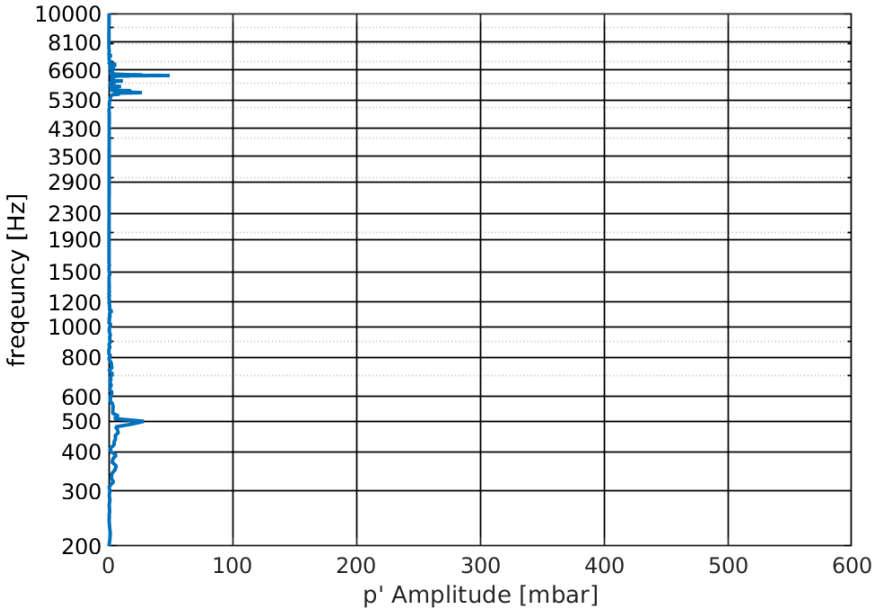

Figure 41: FFT at BP-04 location for inlet temperature of 680K and Φ= 0.75

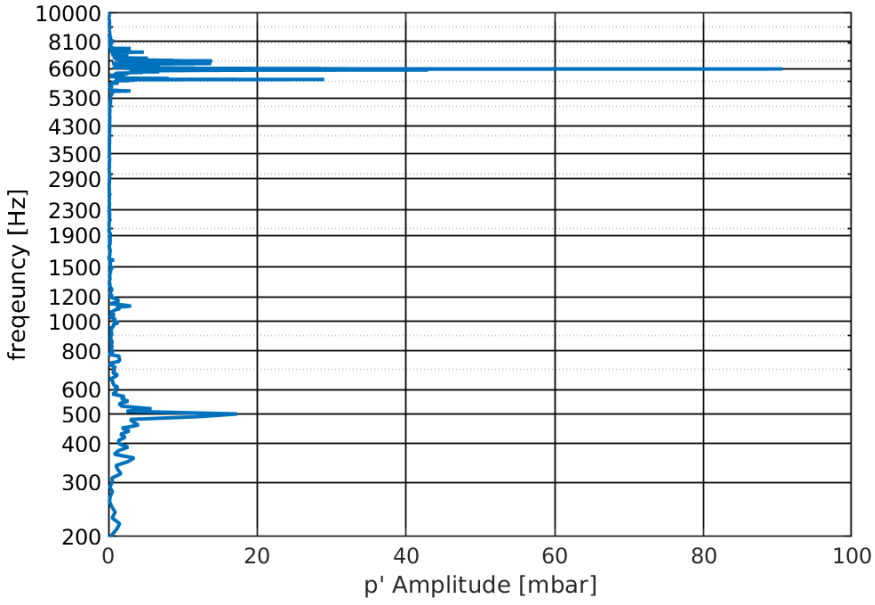

Figure 42: FFT at CH-01A location for inlet temperature of 680K and Φ= 0.75

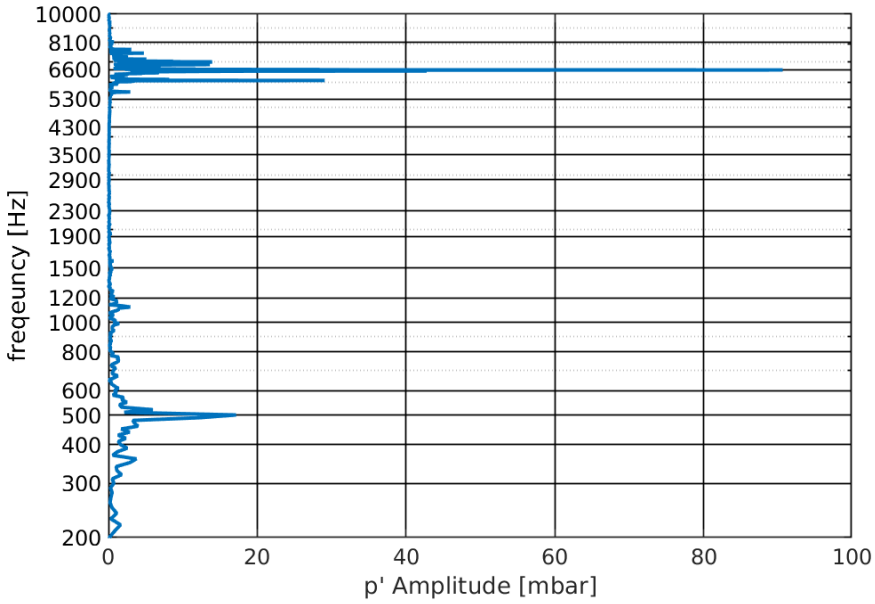

Figure 43: FFT at CH-01B location for inlet temperature of 680K and Φ= 0.75

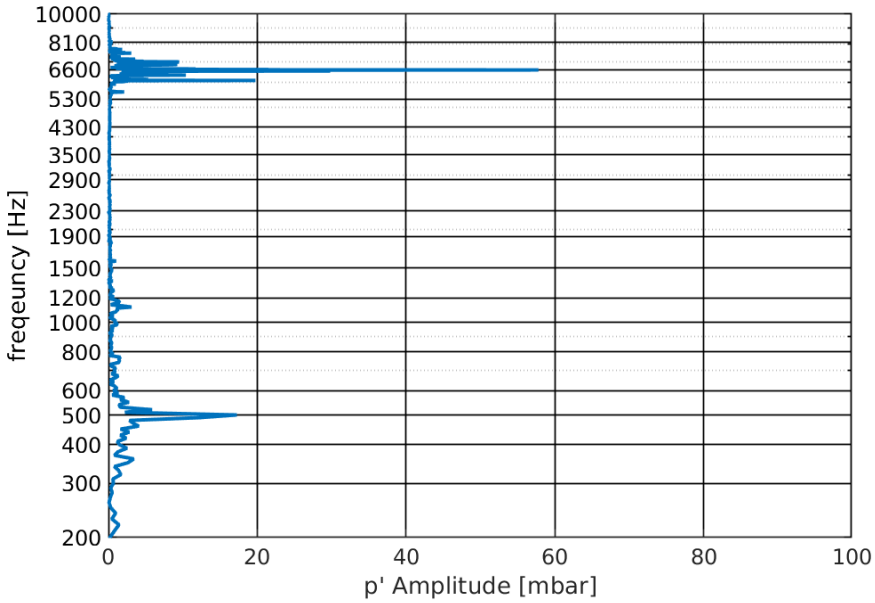

Figure 44: FFT at CH-01C location for inlet temperature of 680K and Φ= 0.75

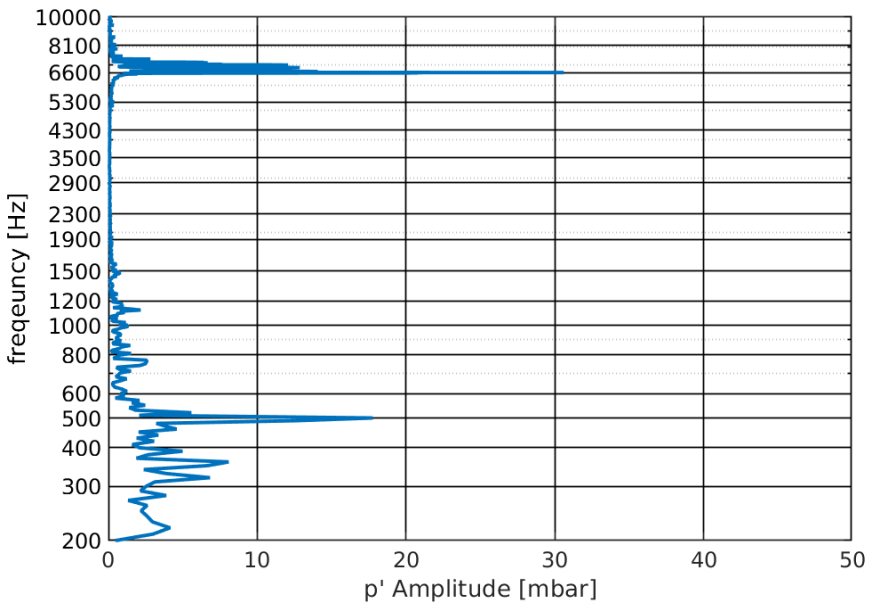

Figure 45: FFT at AFT location for inlet temperature of 680K and Φ= 0.75

Discrete Window and Sampling Sensitivity

Figure 46 and Figure 47 are amplitude spectra similar to Figure 34 except that only the first 50 ms and latter 50 ms of the signal are used respectively. In Figure 46, the peaks are now 37 mbar at 500 Hz, 128 mbar at 5600 Hz and 166 mbar at 6100 Hz. In Figure 47, the peaks are 35 mbar at 500 Hz, 121 mbar at 5600 Hz, and 170 mbar at 6100 Hz. The differences in the amplitudes (which can be interpreted as uncertainties) are quite significant (most noticeably for the ~6 kHz peak). However, the un-averaged FFT yields the desired frequency peaks (to within the bin resolution) and the acoustic state is well-represented: there are instabilities at 500 Hz, 5590 Hz, and 6090 Hz.

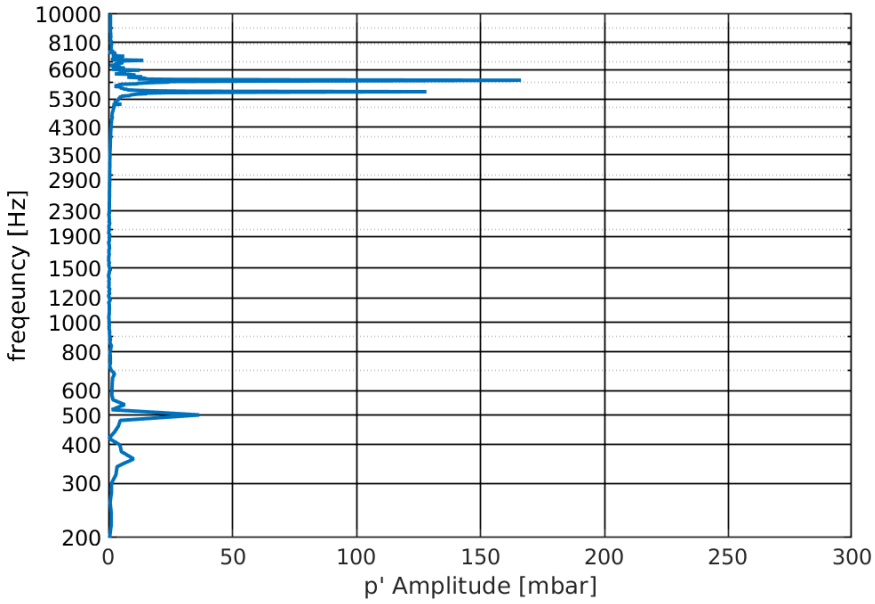

Figure 46: FFT of only the earlier 50 ms of the signal in Figure 32

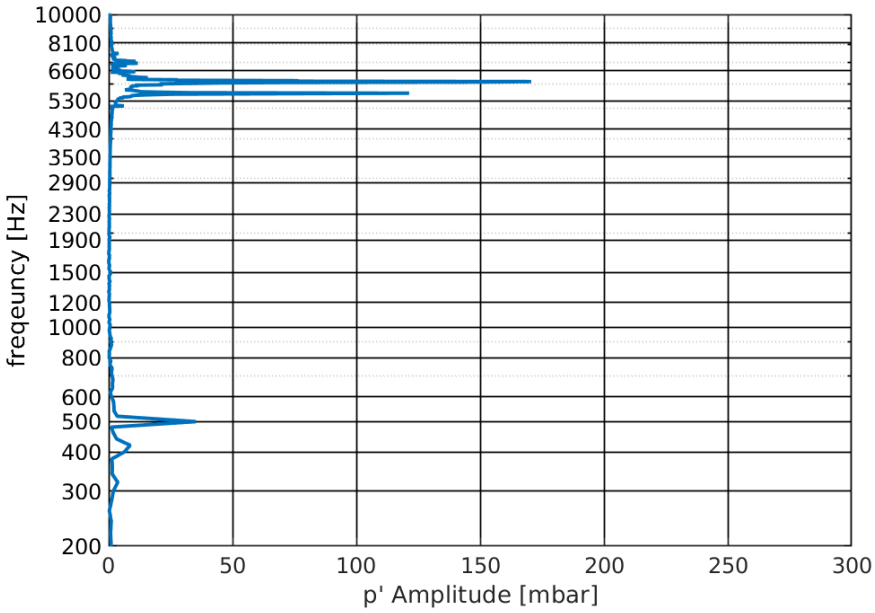

Figure 47: FFT of only the latter 50 ms of the signal in Figure 32

The different spectra are a result of both signal variation as well as discrete sampling variation. The different amplitudes in the earlier and latter parts of the signal are a result of the different states appearing in the signal at these times. The earlier and latter signals are not identical and may be interpreted as coming from different signals, resulting in slightly different spectra. However, even the same continuous signal can have different spectra when sampled differently.

The continuous-time Fourier transform of an unwindowed single sinusoidal function of infinite duration is zero for all but the sinusoidal frequency. A sampled signal is both windowed and discrete, the finite duration signal can be interpreted as a rectangular window applied to the infinite length signal whereas sampling discretizes the continuous signal. The continuous-time Fourier transform of the continuous but windowed signal (also called the discrete-time Fourier transform) will have valleys and crests proportional to the number of cycles contained in the finite-duration signal. Due to spectral leakage, the peaks of the discrete-time Fourier transform (DFTF) may be at different frequencies than the Fourier transform of the infinite duration continuous signal. A windowed but continuous signal has an infinite sampling frequency. When the windowed signal is sampled at a finite sampling frequency, the discrete Fourier transform (DFT) of this windowed and discretized signal is equivalent to a sampling distribution of the DFTF of the windowed but continuous signal. Hence, the same continuous signal, when sampled differently (resulting in different discretizations) may have different DFT's.

The different bin frequencies in the spectra are of course due to the different frequency bin widths (due to different signal lengths). The higher/lower amplitudes of the 100 ms signal

versus the 50 ms signals are also influenced by spectral leakage (the frequencies leak into and out of particular bins) with different applied windows. In this case the frequency bin resolution (due to the shorter signal duration of 50 ms) is increased to 20 Hz instead of 10Hz. Hence the peaks occur at a frequency of 5600 Hz and 6100 Hz instead of 5090 Hz and 6090 Hz. Although there are no bins at 5090 Hz nor 6090 Hz with a bin resolution of 20 Hz, there are bins at 5100 Hz and 6100 Hz for all three cases. Although the true, precise frequency is unknown, the spectrum leaking out of the 5600 Hz and 6100 Hz bins and leaking into the 5590 bins and 6090 Hz bins is mostly due to spectral leakage since the same 5600 and 6100 Hz peaks were found in the spectra for both of the short signals (strong peaks were not found at the 5580 Hz or 6080 Hz bins). To further illustrate the spectral leakage, the signal in Figure 32 is sampled at lower rates. The original FFT in Figure 34 was sampled at a rate of 1 MHz, the amplitude spectrum of the same base signal, keeping the same start time, but sub-sampled at 500 kHz is plotted in Figure 48 and 200 kHz in Figure 49. The peaks in Figure 48 and Figure 49 are essentially the same for both: 34 mbar at 500 Hz, 125 mbar at 5590 Hz, and 238 mbar at 6090 Hz. For brevity, figures are not repeated but, the same amplitudes and frequencies were found when the start time was shifted by 1 or a few indexes. The sampling frequency does not affect the bin width; since the signal duration was also 100 ms, the frequency bin resolution is the same 10 Hz and peaks are found at the same frequencies for all three sampling frequencies. On the other hand, the amplitudes being identical indicates that the sampling frequency (and number of samples) is sufficiently high to be considered free from signal aliasing effects. The insensitivity to the signal start time also indicates that enough samples have been taken and a sufficient number of cycles are contained in the interrogation window of 100 ms to be insensitive to sampling alias. Hence,

the most crucial and most limiting parameter for analyzing the amplitude spectra is the simulation time (the sampling frequency is naturally high due to the small time-steps).

To further illustrate the importance of signal duration on the bin width, the simulation history of 1000 ms was used and the amplitude spectra computed in Figure 50. With a bin resolution of 1 Hz, the peaks in this figure are 28 mbar at 497 Hz, 74 mbar at 5593 Hz, and 165 mbar at 6091 Hz. With the higher frequency resolution afforded by the 1000 ms signal length, these frequencies are closer to the true frequency.

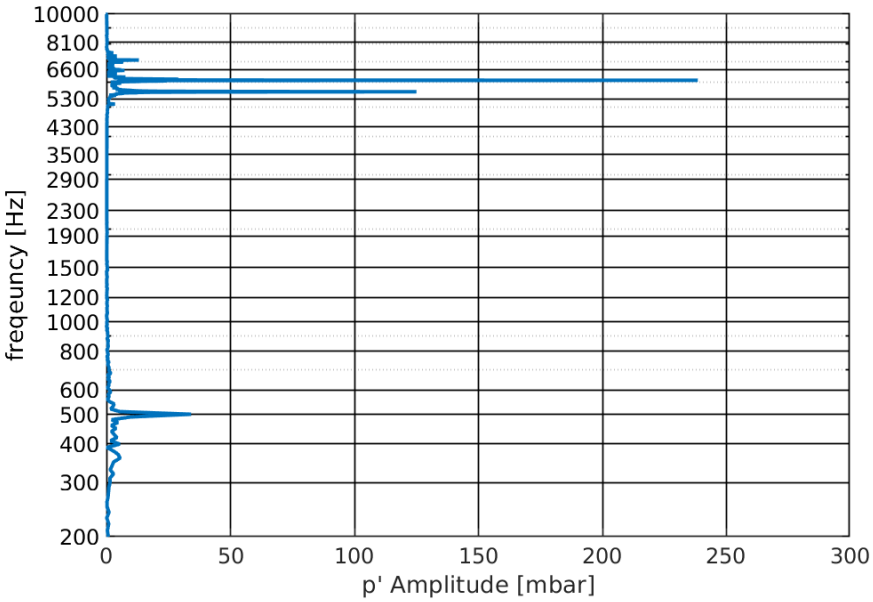

Figure 48: FFT of full 100 ms of the signal in Figure 32 sub-sampled at 500 kHz

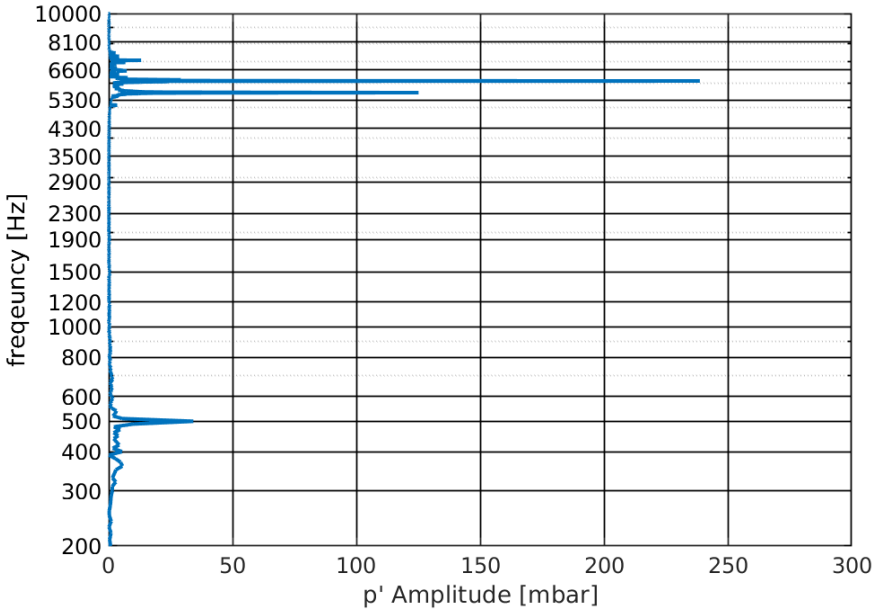

Figure 49: FFT of full 100 ms of the signal in Figure 32 sub-sampled at 200 kHz

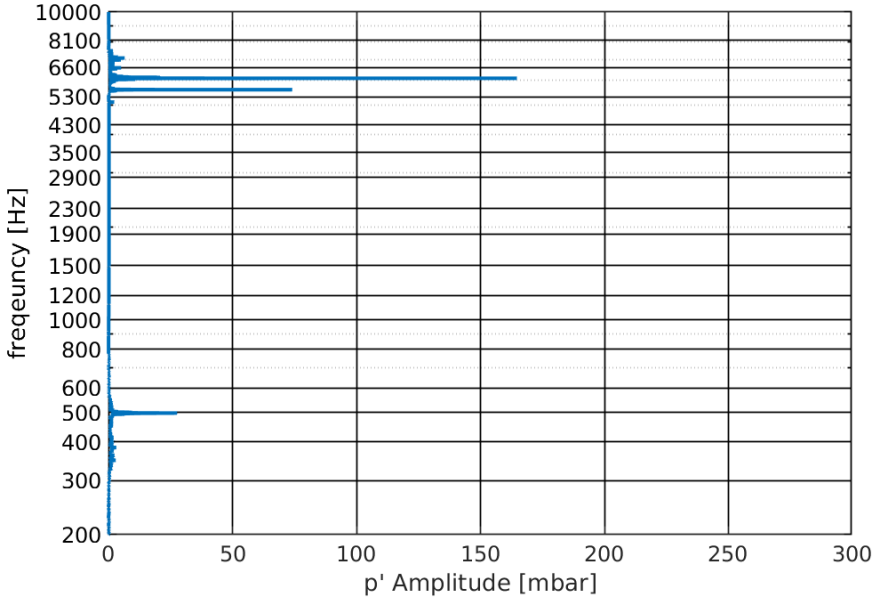

Figure 50: FFT of 1000 ms simulation history sampled at 1 MHz

In general, the frequency content of a signal can be determined to within a bin width, which is limited by the signal duration. If the goal is to determine the frequency of a phenomenon to within a certain range, then the bin width can be pre-selected. For example, if it is desired to determine the frequency to within 100 Hz, then only a 100 Hz bin resolution is needed, implying that only 10 ms signal is required. However, the signal duration is important not only because of the bin width but for statistical accuracy. With longer signal durations, more (acoustic) cycles are captured and the spectrum can be more accurately computed. Additionally, to obtain the correct spectrum requires spectral leakage to be controlled. Hence, it is recommended to always calculate spectra using the maximum available length to limit spectral leakage although this maybe costly due to the computational costs required to simulate longer times.

The amplitude from spectra with different input signals are summarized in Table 2. The pressure amplitudes can vary significantly (around 50%) when different signals are used. The un-averaged spectra are reasonable indicators of active frequencies and gauging their relative strengths compare to one another within a signal. The causes for the different amplitude spectra are due to both discretization (windowing and sampling) of continuous signals as well as due to changes in the flow solution during the transient simulation. The latter effect can be considered a sampling error if the temporal solution can be considered statistically stationary (this presumes however that the solution is spatially stationary). Practically, numerical solutions slowly drift over time so that the error is more often considered to a statistical sampling error (the observation of an instance from a statistical ensemble, probably with random error and possibly with bias error) and not a discrete sampling error. Estimating amplitude spectra using FFT's

without averaging makes the spectra obtained susceptible to noise. Other methods were considered, including averaged periodigrams. In Welch's method, the signal is split into (overlapping) segments, a window function is applied to each segment, the periodiagram is computed for each segment, and then the periodiagrams are averaged. Due to windowing however, Welch's method generally overpredicts the amplitudes compared to a direct amplitude spectrum calculating from an FFT. Although the averaging in Welch's method affords better confidence intervals, there is a trade-off between accuracy and uncertainty and an improved accuracy in estimating amplitudes is not guaranteed.

This analysis was performed (for the CUBE probe only) in order to quantify the sensitivity of the amplitude spectra (or FFT) to the input signal parameters (number of samplings & sampling frequency). The preferred settings for the FFT is always the one with minimum frequency bin width (or maximum frequency resolution) and using all the available signal and plots are generated at other probe locations (i.e. a sampling frequency of 100 MHz and duration of 100 ms, corresponding to a frequency bin width of 10 Hz).

Table 6: Pressure amplitudes with different signal lengths and sampling rates

Signal Length (ms)	Sampling Rate (MHz)	Amplitude (mbar)	Frequency (Hz)	Amplitude (mbar)	Frequency (Hz)	Amplitude (mbar)	Frequency (Hz)
100	1	34	500	125	5590	238	6090
50	1	37	500	128	5600	166	6100
50	1	35	500	121	5600	170	6100
100	0.5	34	500	125	5590	238	6090
100	0.2	34	500	125	5590	238	6090
1000	1	28	497	74	5593	165	6091

Mesh Sensitivity Study

Figure 51 is the FFT of the pressure fluctuations at the BP-01 location for the baseline 4mm grid. Figure 52 is the corresponding plot, but for the 2mm grid. The signal length (100 ms), sampling rate (1 MHz) is the same for all cases. The same time-step size of 0.2 μs was used for the 4mm and 2mm grids. The maximum acoustic Courant number encountered was about 0.8 for the 4mm grid and 0.9 for the 2mm grid. The maximum Courant number did not change much because a similar wall clustering was applied to both grids; the smallest cells were similar for both grids, the change in the grid spacing was mostly in the core mesh. The compute cost for the 4mm grid (typically run on 280 processes) is about 0.8 compute years per 100 ms. The compute cost for the 2mm grid (typically run on 560 or more processes) is about 3 compute years and 8 compute years for the 1mm grid. The FFT peaks for the 4mm grid are: 19 mbar at 500 Hz, 485 mbar at 5590 Hz, 212 mbar at 6090 Hz, 48 mbar at 6590 Hz. The peaks for the 2mm grid are: 16 mbar at 490 Hz, 572 mbar at 5540 Hz, 243 mbar at 6030 Hz, 78 mbar at 6510 Hz. Both grids show the same dominant frequencies, with similar frequencies with similar fluctuation levels. Given that LES is spatially filtered and that the same spectra were obtained for both the 4mm and 2mm grids (with high levels of fluctuation amplitudes), it can be concluded that the 4mm grid resolution was sufficiently fine (despite its coarseness compared to the 2mm grid) to resolve the acoustic-flame interactions.

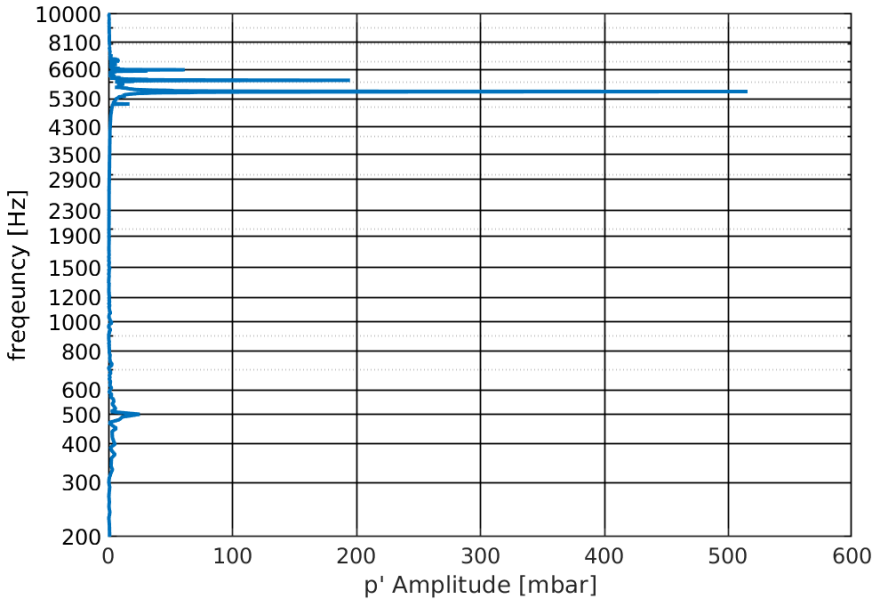

Figure 51: FFT of BP-01 probe on 4 mm grid

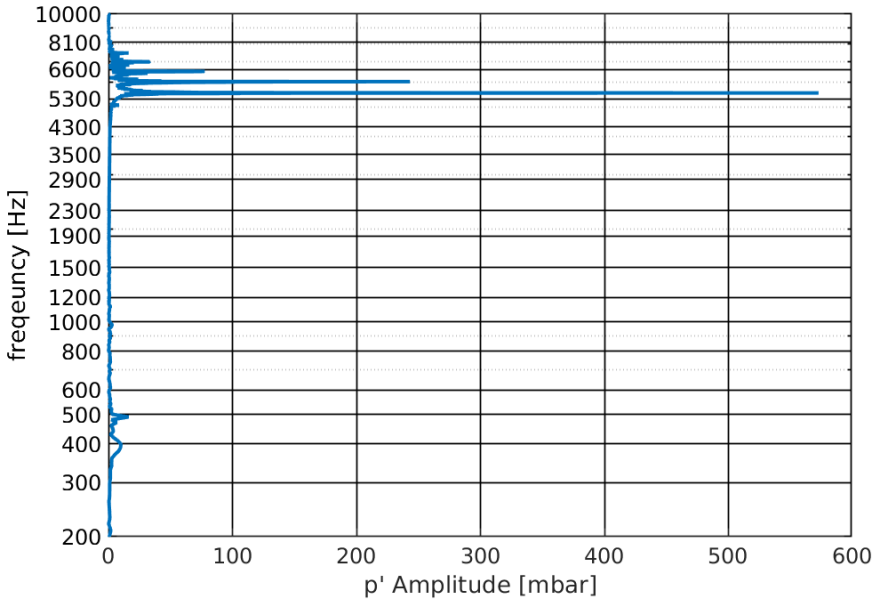

Figure 52: FFT of BP-01 probe on 2 mm grid

The rig measurements recorded peaks primarily at 5.2 kHz and 5.8 kHz. It is hypothesized that these frequencies are corresponding to the 5.6 kHz and 6 kHz found in the spectra from LES based on the trends discussed. The difference in frequencies measured versus calculated from LES are likely due to the modeled gas properties of the mixture. That is, the equation of state and specific heat of the mixture settings applied in the LES might not match (closely enough) to the real gas properties. Raw natural gas fuel is a complex substance with many chemical constituents, which has been modeled as a much simpler mixture of only a few compounds. The effect of heat loss to the combustor walls was also neglected in this model, the thermal boundary condition was adiabatic for all walls in the LES. The gas temperature would be colder when these thermal losses are taken into account and this is consistent with the lower frequencies observed in the spectra from rig measurements compared to the spectra obtained from LES.

Much larger pressure amplitudes were found in the LES compared to the rig measurements; pressure amplitudes of 100 mbar and 200 mbar at 5.6 and 6 kHz were observed in the spectra at the CUBE location, compared to the 10 mbar and 20mbar amplitudes observed in the experiment. The location of the CUBE probe in the numerical simulation is at the pressure anti-node, where the pressure amplitude is a maximum (at this axial location). There isn't any indication whether the pressure transducers in the experiment are placed at a pressure anti-node. If the CUBE transducer was nearer the pressure nodes in the VIPER experiments at Purdue, that would immediately explain the lower amplitudes observed in the rig.

It should not be understated that the LES results are predicated on the flame-wrinkling model that was applied. It is possible that the flame-wrinkling model does not accurately predict the correct physical processes. However, it is noteworthy that similar trends are observed in the LES as found in the experiment. Further tuning of the model is possible (the wrinkling factor coefficient is a tunable parameter in the flame-wrinkling model). More robust models will provide better (more accurate) predictions, but the flame-wrinkling model seems appropriate for this problem. The current LES approach produced the most important qualitative results and the differences between the rig pressure measurements and spectra from LES are within the realm of reasonable expectations.

As noted in the previous chapter, the FFT of point probes at these various locations can be correlated to acoustic frequencies and modeshapes. The acoustic eigenfrequencies and modeshapes are calculated using COMSOL in the next chapter. The phase-averaging of the time-resolved velocity and pressure fields in the subsequent chapter will also demonstrate that these frequencies are indeed the acoustic modes and confirm the presence of a self-excited thermoacoustic instability.

Sensitivity to Outlet Boundary Condition

In order to demonstrate the insensitivity of the condition to the acoustic boundary conditions at the domain exit, a simulation was carried out on a modified domain with the exit nozzle removed. The original domain and modified domain are depicted in Figure 53. The modified domain terminates at the start of the exit nozzle and end of the straight 80 mm diameter cylindrical section of the combustion chamber. At this truncated boundary, the non-reflecting

boundary condition was applied (the same non-reflecting boundary condition was also used at the exit boundary condition for the original domain with the sonic nozzle). This acoustic condition for the truncated domain is vastly different compared to the original domain with the exit nozzle. With the choked exit nozzle, acoustic waves arriving at the nozzle are reflected by the solid walls of the nozzle and partially reflected by the sonic condition at the nozzle throat (i.e. reflected by the Mach disc). With the exit nozzle removed, the sonic condition is no longer being a feature in the simulation and walls are no longer present. With non-reflecting boundary conditions being applied at the exit boundary the acoustic waves arriving at the exit are now able to freely exit the domain instead of being reflected by the nozzle walls and at the nozzle throat. A possible criticism is that numerical implementation of the non-reflecting boundary condition is partially reflecting. However, the implementation tends to reflect low-frequency perturbations and is non-reflecting for high frequencies (this behavior is controlled by the timescale factor, which is a numerical setting). Hence, the non-ideal behavior of the numerical non-reflecting boundary condition should not be an issue for the high frequency transverse modes (although it may impact some lower frequency modes).

Figure 53: Computational domain with exit sonic nozzle (top) and truncated domain with exit nozzle removed (bottom)

A new mesh was generated for the truncate domain, which was similar to the 4mm baseline grid. The mesh topology was nearly identical, and the mesh did not deviate much from the baseline grid except for the at the domain exit. The simulation with the truncated domain was performed for the same condition as the reference case (an inlet gas temperature of 680 K inlet temperature, total mass flow rate of 0.553 kg/s and equivalence ratio of 0.75). The solution for the reference case was used as the initial condition of the new case. Another 500 ms of flow time was simulated to allow the flow to adjust to the new boundary conditions and attain its new statistically stationary state. After this additional 500 ms transient, the pressure was analyzed over a duration of 100 ms using the same post-processing procedure as previously. The pressure amplitude spectra at the CUBE location is given in Figure 54 and at the BP-01 location in Figure 55. At the cube location, there is a 16 mbar peak at 510 Hz, 172 mbar at 5590 Hz, and 165 mbar at 6100 Hz. At the BP-01 location, there is a peak of 741 mbr at 5590 Hz and 158 mbar at 100 Hz. The amplitudes are generally greater than with the original domain with the sonic nozzle. Although the amplitudes differ, these frequencies are essentially the same as those with the sonic nozzle, demonstrating that the acoustic instabilities in this configuration are insensitive to the acoustic boundary condition at the exit. The same unstable modes are found with and without the sonic nozzle similar trends are observed at both the BP-01 and CUBE locations: namely peaks at 500 Hz 5600 Hz and 6100 Hz appearing at the CUBE location and peaks at 5600 Hz and 6100 Hz at the BP-01 location, with a stronger 5600 Hz peak than 6100 Hz at the BP-01 location. It is demonstrated in the next chapter than the eigenfrequencies and eigenmodes of this configuration are unaffected by the acoustic boundary condition at the outlet. Hence, for the purpose of studying the high frequency transverse modes in this configuration, either acoustically reflecting

or non-reflecting boundary condition may be applied with minor impact. This insensitivity of the instability to the outlet boundary condition is desirable since non-reflecting boundary conditions are not widely implemented in CFD codes. The simpler constant pressure boundary condition (which is acoustically reflecting) may even be applied. This insensitivity, however, is limited to only the high frequency transverse modes. Although the 1T1L mode at around 6100 Hz has a longitudinal component and was found to be insensitive to the exit boundary condition, the lower (purely) longitudinal modes (which have a lower frequency for this configuration) are expected to be sensitive to the acoustic boundary condition at the exit (both the modeshape and frequency of purely longitudinal modes will be affected).

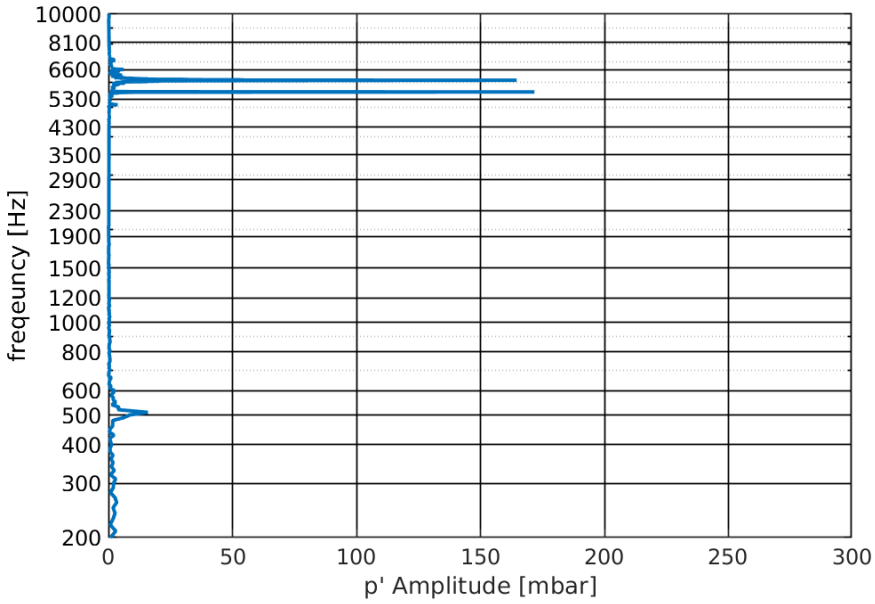

Figure 54: FFT at CUBE location for inlet temperature of 680K and Φ= 0.75 on truncated domain with nozzle removed and non-reflecting BC at exit

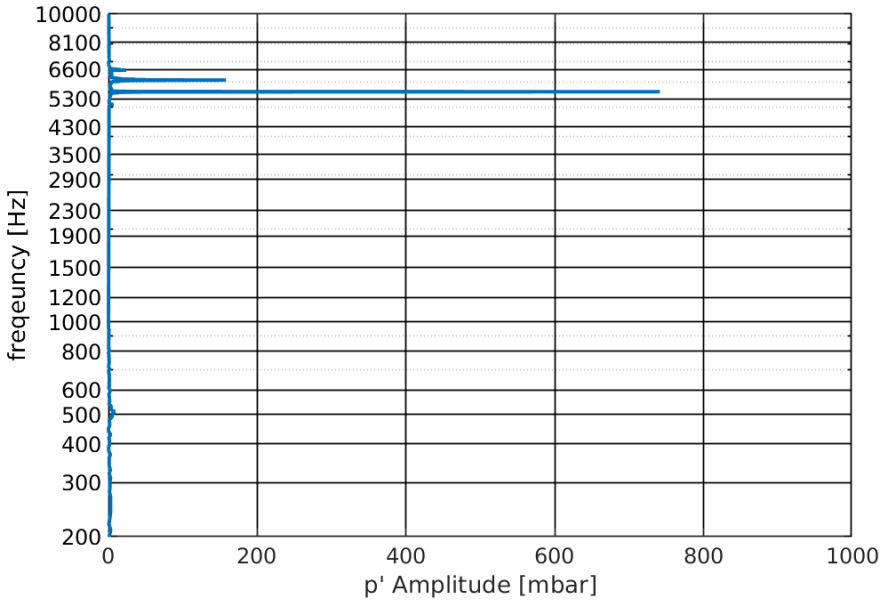

Figure 55: FFT at BP-01 location for inlet temperature of 680K and Φ= 0.75 with nozzle removed and non-reflecting BC at exit

Sensitivity to Numerical Settings

The impact of various solver settings in OpenFOAM was explored by re-running the reference case and systematically altering the settings. In this subsection, the amplitude spectra at the BP-01 location are compared for each case. The BP-01 location shows the most distinct peaks and is the best candidate for comparing multiple cases.

The treatment of the advection terms (as opposed to diffusive terms) is a major challenge in CFD and where the available options are most extensive. Since the underlying advective flux in all transport equations is the velocity, obtaining an accurate solution to the velocity is paramount and requires the most care when selecting the discretization scheme for the advection term. The filteredLinear2V scheme was primarily used in this dissertation, which is a linear (central difference) which is bounded and limited to prevent overshoots. Two other similar and widely used schemes are the limitedLinearV scheme and filteredLinear scheme. The filteredLinear2V scheme (is a secondary adaptation to the original filteredLinear scheme) is a more scheme. It is an interesting exercise therefore, to benchmark what the results with these other schemes would look like not only to but also to test the sensitivity of the thermoacoustic instabilities to a particular scheme. A potentially detrimental result could be, that thermoacoustic instabilities arise only when a particular scheme is being used. When this occurs, the driving mechanism of the instability becomes questionable, since it may be due to numerical oscillations generated by the spatial discretization scheme. A simulation with only the discretization scheme for the advection term in the momentum equation (the div(phi,U) term), all other settings were left the same as the reference case, with the same deltaT = 0.2 μs, PIMPLE-based solver, and Crank-Nicolson 0.9 scheme.

The limitedLinear scheme is a limited version of the second order linear scheme (i.e. central differencing) but with upwind biasing. The limitedLinear scheme tends towards the 1st order upwind scheme in regions with rapidly changing gradients (the upwind scheme is 1st order and bounded). The coefficient in the limitedLinear scheme controls the aggressiveness of the limiter. A coefficient of 1 was used in this study, which guarantees bounded so that there are no non-physical overshoots/undershoots. Unbounded spurious oscillations are detrimental because they yield non-physical results. A scheme that is less accurate (lower order of convergence) but maintains the solution boundedness is preferred for LES. Hence, bounded schemes like the limitedLinear scheme are often used over the linear scheme. Despite the loss of convergence order, the boundedness property is much more physically accurate. The pressure amplitude with the limitedLinearV 1 scheme in Figure 56. The filteredLinear schemes are also bounded central differencing based schemes but with a filtering operation in the gradient interpolation and was designed to be less dissipative than the limitedLinear scheme (the upwind biasing of the limitedLinear scheme is prone to numerical diffusion, the same as an upwind scheme). The results with the filteredLinear scheme are presented in Figure 57.

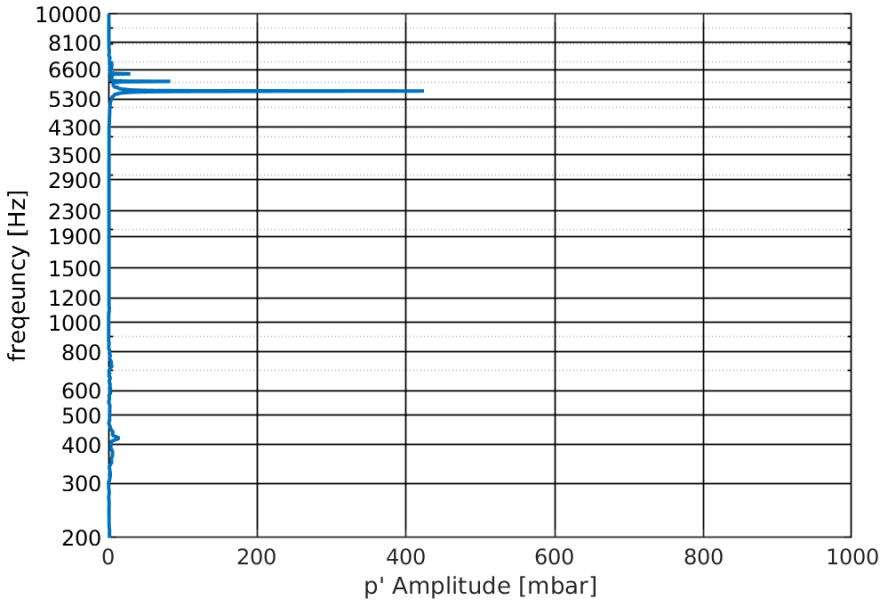

Figure 56: FFT at BP-01 location for inlet temperature of 680K and Φ= 0.75 with 0.2 μs time-step, PIMPLE solver, Crank Nicolson 0.9 scheme and limitedLinearV 1 scheme

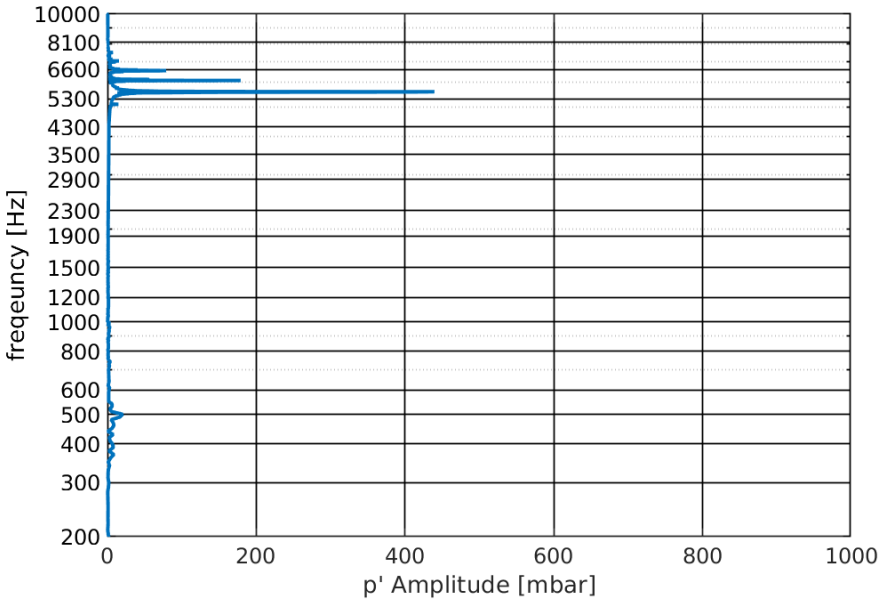

Figure 57: FFT at BP-01 location for inlet temperature of 680K and Φ= 0.75 with 0.2 μs time-step, PIMPLE solver, Crank-Nicolson 0.9 scheme, and filteredLinear scheme

It is well known that although the Crank-Nicolson method is stable, it is susceptible to spurious numerical oscillations whenever the Courant number exceeds 0.5. The baseline time-step size (specified OpenFOAM using deltaT) was 0.2 μs and corresponds to a maximum Courant number of around 1.0. Recall that the mean and typical Courant number is much smaller than the maximum Courant number (which occurs for only a few cells). Significant reduction in computational costs can be realized if larger time-steps can be used safely. Furthermore, the temporal discretization scheme used blends the classical Crank-Nicolson scheme with a backward Euler scheme (a blending coefficient of 0.9 was used for the cases in this dissertation). The blending makes the solver much more robust against oscillations and more tolerable of larger time-steps (the Courant number of 1 exceeds classical limit of 0.5 from von Neumann stability analysis). However, it is must verified that spurious oscillations are well controlled. Hence, simulations were carried out with smaller time-step size (0.1 μs) and a larger time-step size (0.5 μs) to quantify the influence of the time-step size on the results. The maximum acoustic Courant number of thee case with smallest time-step of 0.1 μs was less than 0.4 and the case with a time-step of 0.5 was globally less than 2. Only the time-step size was changed, all other solver settings were left unchanged. The simulation with altered time-steps was run with a PIMPLE solver, Crank-Nicolson 0.9, and filteredLinear2V 0.5 0 scheme, Although the differing time-step sizes affords different temporal resolutions, the sampling rate of 1 MHz was maintained for all cases by adjusting the number sampling frequency relative to the number of time-steps. That is, the simulation with deltaT = 0.2 μs simulation was sampled every 5 time-steps. The sampling interval for deltaT = 0.1 μs was every 10 time-steps and the sampling interval for deltaT = 0.5 μs simulation was every 2 time-steps. Keeping the same sampling rate

and simulation time ensures the effect of windowing is the same for all cases when calculating the amplitude spectrum. The amplitude spectrum for the largest time-step size of 0.5 μs is given in Figure 58 and the smallest time-step size of 0.1 μs in Figure 59. Comparing these two cases, with altered time-step sizes, with the original baseline simulation, which had a time-step size of 0.2 μs, all three cases showed peaks at the same high frequency peaks, but with slightly different amplitudes. In general, the amplitudes at the acoustic frequencies of interest increased as the time-step was reduced. However, the low frequency 500 Hz peak was not found in Figure 58 for the simulation performed with the larger time-steps. Although the results with a time-step of 0.5 μs did not appear to be adversely affected by spurious oscillations (these spurious oscillations would appear as noise in the amplitude spectrum) and still produced thermoacoustic instabilities, the lack of the 500 Hz peak indicates a different solution state. Without looking deeper, it is not clear the cause for the presence of lack of a 500 Hz peak. Although a time-step size of 0.2 μs results in a cell Courant number exceeding the 0.5 limit of the CFL condition, this condition is violated only in a few cells. Most of the computational cells in the domain still satisfy the CFL condition. Hence, it is acceptable to run larger time-steps provided that the oscillations in these few cells do not adversely affect the overall solution. Hence, the time-step size of 0.2 μs was selected and used throughout this dissertation for the self-excited LES since it is computationally less expensive than, but still producing the same acoustic content (although the amplitudes differ slightly) as, the more accurate simulation with a time-step of 0.1 μs. Ideally, with unlimited resources and time, the simulation with a deltaT of 0.1 μs (or even smaller) would still be preferred.

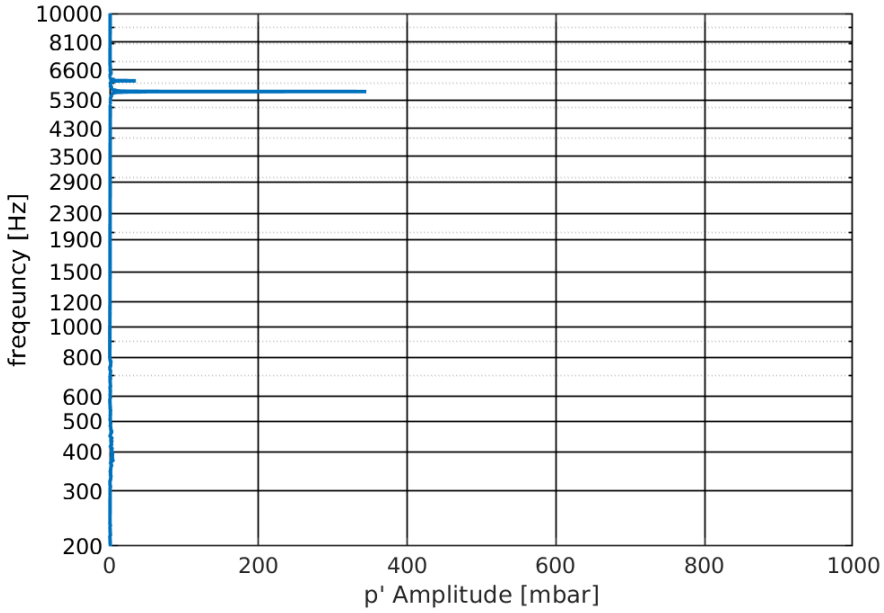

Figure 58: FFT at BP-01 location for inlet temperature of 680K and Φ= 0.75 with 0.5 μs time-step, PIMPLE solver, Crank-Nicolson 0.9 scheme, and filteredLinear2V scheme

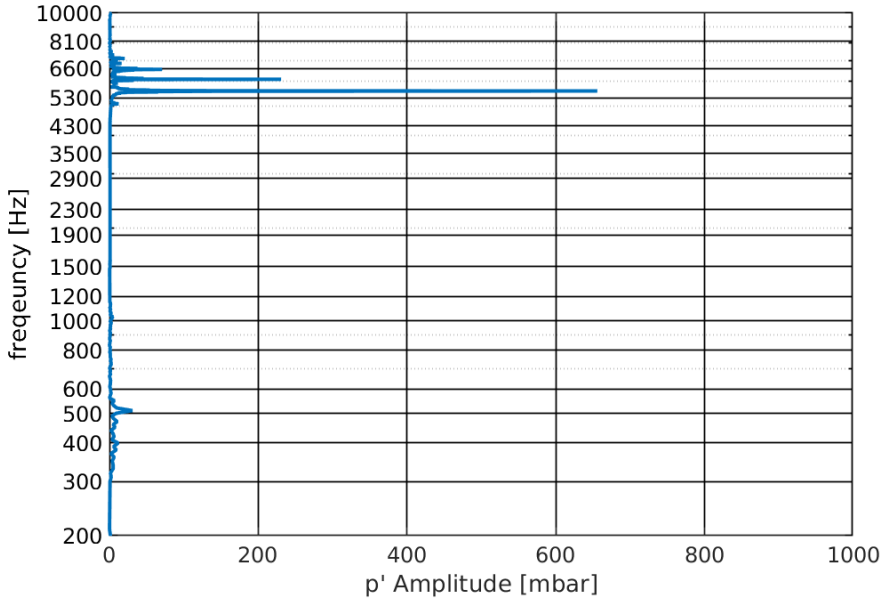

Figure 59: FFT at BP-01 location for inlet temperature of 680K and Φ= 0.75 with 0.1 μs time-step, PIMPLE solver, Crank-Nicolson 0.9 scheme, and filteredLinear 2V scheme

The PIMPLE solver combines several SIMPLE-like iterations with a final PISO-like iteration. In this dissertation, nOuterCorrectors was set to 3: corresponding to two SIMPLE sweeps followed by a PISO sweep. Implicit under-relaxation is applied in the SIMPLE steps, allowing PIMPLE to be a flexible solver that can handle both small and large time-step sizes by tuning the under-relaxation factors. In this dissertation, the under-relaxation factors for all equations was set to 1 except for the pressure and velocity variables. The under-relaxation factor for pressure and velocity was set to 0.9 for the SIMPLE steps and returned to 1 for the final PISO step.

When solving relaxed equations in a purely SIMPLE-based approach, the convergence of each time-step would normally need to be verified. However, the final PISO sweep in PIMPLE recovers the proper "steady-state" solution at each time-step. Steady state here refers not to the temporal derivative of the flow being 0, but refers to the iterative convergence of the solution at a particular time-step. After temporal discretization has been applied to the differential equation involving temporal derivatives, the resulting discretized equation is analogous to a steady differential equation. That is, steady-state (in this context) does not mean that the flow becomes stationary in time, but that the numerical solution of the implicitly under-relaxed and discretized equations has become steady with respect to the solver iteration.

Because the PIMPLE method combines the iterative SIMPLE approach with under-relaxation with a non-iterative PISO approach without any relaxation, it is difficult to say beforehand whether the proper steady-state solution is achieved due to the multiple influences of time-step size, number of iterations, and under-relaxation factors. The influence of the time-step

size has already been presented. A simulation was carried out using the PISO scheme instead of the PIMPLE scheme with the smallest time-step size of 0.1 μs (since this setting also gave a maximum Courant number less than 0.5) to gauge whether the settings used properly advances the solution in time. The pressure amplitude spectra with the PISO-based simulation is given in Figure 60. Unsurprisingly, the same frequencies are found in the spectrum, but also at similar amplitude levels when comparing PISO and PIMPLE or the same deltaT = 0.1 μs. At such small time-steps, the performance of both solvers is similar since the maximum Courant number at this time-step was globally less than 0.5 for both simulations and the only underrelaxation applied to the PIMPLE-based simulation was 0.9 on pressure and velocity.

Since the PISO approach requires only two sweeps, it can be more computationally less expensive than the PIMPLE approach (since 3 sweeps were performed). This benefit can be exploited when running simulations with very small time-steps (when the Courant number is less than 0.5). However, the faster speed of PISO is limited to problems where convergence is limited by the pressure-velocity coupling problem (the solution of the continuity and momentum equation pair to obtain both a velocity and pressure variable). For thermoacoustic problems, there is stronger coupling with the energy equation, and convergence is also limited by the coupling with the energy equation (rather than only the pressure-velocity coupling). The multiple sweeps of the PIMPLE-based approach are better suited for handling the momentum-energy coupling (coupling between velocity/pressure with temperature) than PISO. Hence, the PIMPLE approach can be more efficient than PISO overall, especially when run with the larger time-steps that PISO cannot handle (PISO is numerically unstable for larger Courant numbers).

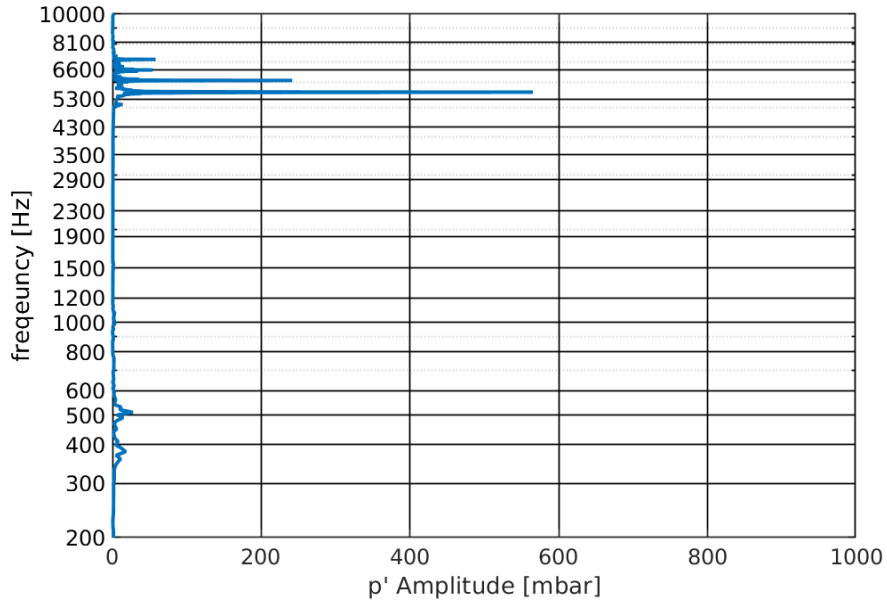

Figure 60: FFT at BP-01 location for inlet temperature of 680K and Φ= 0.75 with 0.1 μs time-step, PISO solver, Crank-Nicolson 0.9 scheme, and filteredLinear2V scheme

As already mentioned, the pure Crank-Nicolson scheme is prone to spurious numerical oscillations. For this reason, the implementation of this scheme in OpenFOAM includes a blending coefficient, blending the pure Crank-Nicolson scheme with the 1st order upwind Euler scheme. A blending coefficient of 1 corresponds to a true Crank-Nicolson approach and a blending coefficient of 0 corresponds to a true Euler approach. A blending coefficient of 0.9 is often recommended in user manuals for controlling the spurious oscillations while maintaining the higher-order convergence of Crank-Nicolson scheme. A blending coefficient of 0.9 works well when there are not other sources of numerical oscillations. Practically however, a blending coefficient of 0.9 is often not enough to control the spurious oscillations. For unstructured polyhedral grids, the oscillations arising from the spatial discretization as well as interpolation errors from gradient calculations are compounded with the oscillations associated with the

Crank-Nicolson scheme. For CFD of industrial problems on these unstructured grids, even blending factor of 0.5 is considered ambitious. The loss of accuracy with lower blending factor probably limits the ability of typical LES to capture the thermoacoustic instabilities. Since the VIPER configuration is geometrically simple, it was possible to generate a well-structured mesh and have stable solutions with a blending factor of 0.9. However, the risk of spurious oscillations is prevalent even when the solution is stable. A common fear amongst CFD user is that peaks in the pressure spectra are caused by the numerical oscillations and are not representative of the actual flow solution. In other words, the seemingly thermoacoustic instabilities are driven by numerical instabilities rather than coupling between the acoustic oscillations and unsteady heat release. A simulation as run with the same settings as the reference case, using the time-step of 0.2 μs and original PIMPLE scheme, but changing the blending coefficient to 0.8 to verify that the using a blending coefficient of 0.9 was not brazen. The amplitude spectrum for the case with a blending coefficient of 0.8 is given in Figure 61. The same 5600 Hz peak and 6100 Hz peak are found with similar levels of amplitude and trends as previous (a much stronger 5600 Hz peak compared to the 6100 Hz peak). Although the lower blending coefficient tends to damp more the numerical oscillation, the 5600 Hz peak is a higher amplitude and the 6100 Hz peak is a lower amplitude than the reference case, which is inconsistent with a reduced level of spurious oscillations. Although some impact of the temporal discretization scheme can be seen, the 5600 Hz and 6100 Hz modes do not appear to be driven entirely by numerical oscillations (since the 6100 Hz peak was stronger, even with a more damped scheme).

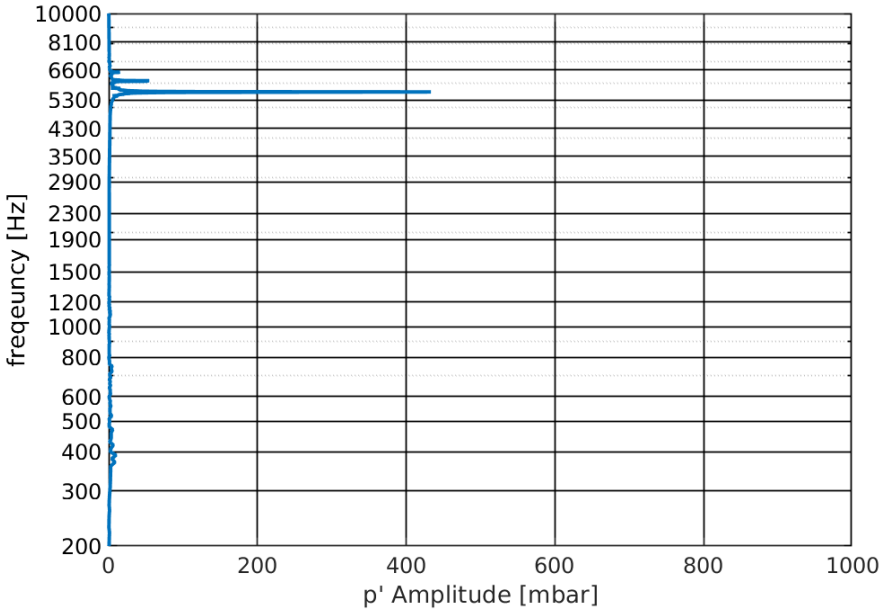

Figure 61: FFT at BP-01 location for inlet temperature of 680K and Φ= 0.75 with 0.2 μs time-step and PIMPLE scheme and Crank Nicolson scheme with a 0.8 blending factor

Table 7: Pressure amplitudes with different numerical settings and schemes

dt $[\mu s]$	ddtScheme	solver	div(phi,U)	f_1 $[Hz]$	$\|p'\|_1$ $[mbar]$	f_2 $[Hz]$	$\|p'\|_2$ $[mbar]$
0.2	CrankNicolson 0.9	PIMPLE	Gauss filteredLinear2V 0.5 0	5590	392	6090	132
0.2	CrankNicolson 0.9	PIMPLE	Gauss limitedLinearV 1	5630	424	6050	83
0.2	CrankNicolson 0.9	PIMPLE	Gauss filteredLinear	5590	440	6080	179
0.2	CrankNicolson 0.8	PIMPLE	Gauss filteredLinear2V 0.5 0	5620	433	6100	55
0.5	CrankNicolson 0.9	PIMPLE	Gauss filteredLinear2V 0.5 0	5635	345	6098	35
0.1	CrankNicolson 0.9	PIMPLE	Gauss filteredLinear2V 0.5 0	5580	656	6090	231
0.1	CrankNicolson 0.9	PISO	Gauss filteredLinear2V 0.5 0	5580	565	6090	242

The results are summarized in Table 7. Recall that the settings varied in this sensitivity study were: the temporal discretization scheme (ddtScheme), the pressure-velocity coupling solve, the spatial discretization scheme for the advection momentum term (the div(phi,U) term), as well as time-step size (deltaT). In general, the same frequencies were found across all simulations with some variations in the amplitudes at each frequencies. Namely, a peak around 5600 Hz and another peak around 6100 Hz. The differences between frequencies observed between each simulation with different settings are explainable by the frequency bin resolution of the fft algorithm. For most cases the variation of the peak amplitude was visible but negligible. It has already been seen that even the same simulation run for different times and sampled over different durations can produce amplitude spectra with quite different amplitude levels. However, the cases with the larger time-steps had appreciable and consistently lower amplitudes (especially for the 6100 Hz mode). The presence of the same frequencies appearing across a wide variety of different numerical settings further validates that these peaks represent the actual physics of the flow and not driven by some spurious numerical instabilities.

The most accurate results are with the smallest time-step size (0.1 μs) with the PISO scheme since it avoids any under-relaxation. Results with PIMPLE and PISO were similar with the smallest time-step size of 0.1 μs. However, PIMPLE is more stable and allows large time-steps to be run with only minor effect on the quality. The reference case (the highlighted row in Table 7) was chosen based on these findings and preferences: a PMIPLE-based solver using the most-accurate Crank-Nicolson 0.9 scheme with the filteredLinear2V scheme and time-step size of 0.2 μs.

CHAPTER FOUR: COMSOL STUDY

Complementary analysis is required to demonstrate that the frequencies observed in the experiments at Purdue in the VIPER rig and the LES are corresponding to acoustic modes (and not other physical phenomena such as hydrodynamic instabilities or turbulence). Hence, analysis is done in COMSOL Multiphysics v5.3 using the acpr solver (acoustic pressure solver from the acoustics module) on the same domain as the LES. The governing equations for the acpr solver in COMSOL are given in Eq. (1), which is a Helmholtz equation. The total acoustic pressure is defined as the sum of the acoustic pressure and background pressure according to Eq. (2). The dispersion relation for the eigenvalues and eigenfrequency are given in Eq. (3). The COMSOL mesh is depicted in Figure 62, which was generated using the built-in predefined "finer" profile, consists of approximately 40 000 elements. It was found that the finer profile yields reasonably accurate eigenfrequency calculations. The "fine," "normal," and "coarse" profiles predict significantly different frequencies, whereas the "extra fine" and "extremely fine" profiles increases the solution time dramatically without appreciable change in the eigenfrequencies. The eigenvalue solver execution time is approximately 5 minutes.

$$\nabla \cdot \left(-\frac{1}{\rho_c} (\nabla p_t - q_d) \right) - \frac{p_t}{\rho_c} \left(\frac{\omega}{c_c} \right)^2 = Q_m \qquad (1)$$

$$p_t = p + p_b \qquad (2)$$

$$\lambda = -i\omega \qquad (3)$$

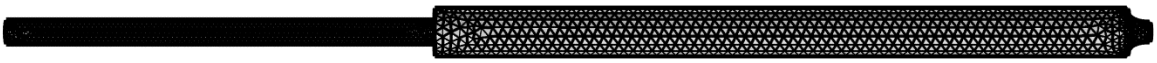

Figure 62: COMSOL mesh generated using predefined finer profile

Eigenfrequencies: Using Mean Fields from LES

The 3D fields of mean (time-averaged) pressure and temperature from the LES calculation are imported into COMSOL for analysis; the pressure and temperature are plotted on a 2D planar-cut in Figure 28 and Figure 30, respectively. The background density field is calculated from this pressure and temperature using the ideal gas relation and the speed of sound is taken as from a calorically perfect gas undergoing an adiabatic process. An acoustic hard reflection is applied to the outlet to in place of the choked outlet boundary condition. Both an acoustic soft and hard boundary condition is applied to the inlet in two different analysis cases. The results with the soft boundary condition are given in Figure 63 and the hard boundary condition are given in Figure 64. The eigenfrequencies are denoted to the right of the acoustic pressure eigenmodes. Many eigenvalues can be found for this configuration, only the most relevant ones are presented: the 1L mode at ~300 Hz, the 1T mode at ~5600 Hz, ~6200 Hz, and the 1T2L mode at ~6600 Hz. These eigenmodes are labeled (1L, 1T, 1T1L, and 1T2L) according to the eigenmodes of a simple cylinder. Lower frequency eigenmodes for this system (a combination of two connected cylinders) so that the label of 1L or example does not indicate that the ~300 Hz mode is the first longitudinal mode of the system (it is the first de-coupled longitudinal mode of the combustion chamber with hard boundary conditions on both ends).

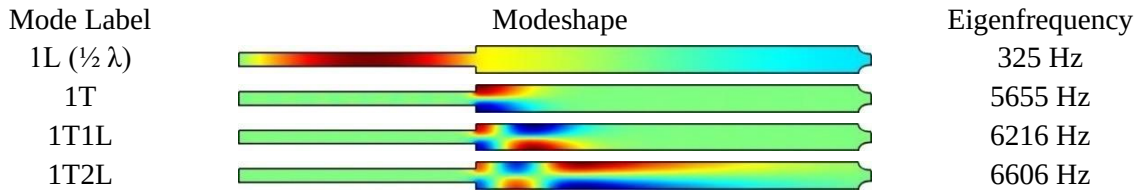

Figure 63: Acoustic eigenmodes using mean fields from LES with acoustic soft inlet

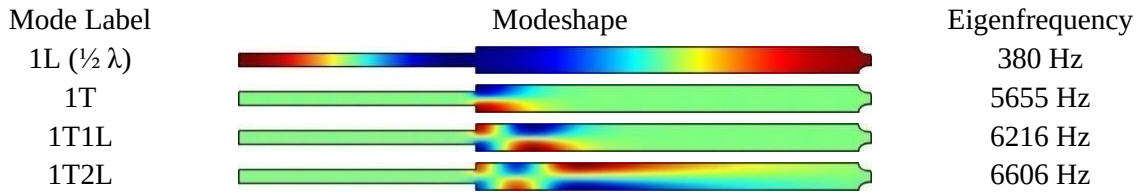

Figure 64: Acoustic eigenmodes using mean fields from LES with acoustic hard inlet

The frequencies of these eigenmodes (5660 Hz, 6220 Hz and 6610 Hz) agree very well with the frequencies found in the spectrum obtained from LES (5600 Hz, 6090 Hz, and 6960 Hz), only a 5% difference for the 1T2L eigenfrequency. Some difference in the eigenfrequencies in COMSOL should be expected with the ones observed in the LES since the COMSOL analysis solves only the Helmholtz equation; the only information provided to the COMSOL analysis is the background pressure and temperature field. More complex analysis can be performed using the Euler equations or linearized Navier-Stokes equations incorporating the influence of the mean flow (in the case of the Euler equations) or viscous effects (in the case of the linearized Navier-Stokes equations). The benefit of using the acpr solver is that the Helmholtz equation is a steady wave equation, the eigenfrequencies and eigenmodes are the acoustic frequencies and acoustic eigenmodes. Thus, it is more tractable to confirm that the frequencies the LES and VIPER experiment are corresponding to acoustic phenomenon since the eigenfrequencies obtained in an analysis using the Euler-equations or linearized Navier-Stokes equations (or the

filtered Navier-Stokes equations in the case of LES) can belong to various other phenomena (vortex shedding for example).

A notable feature of Figure 63 and Figure 64 is that the 1T, 1T1L, and 1T2L modes (and many other modes not presented) are trapped modes (exponentially decaying or evanescent modes) in the combustion chamber. This feature can explain why the 5kHz and 6kHz modes appeared at the CUBE location, but not at the AFT location in the pressure spectrum of the VIPER rig since these frequencies seem to correspond to the 1T and 1T1L modes. A peak at ~6600 Hz was observed at the AFT location in the LES, which seems to be corresponding to the 1T2L mode. The longer axial extent of the 1T2L mode allows mode to the present on the AFT location in the LES. No high frequency peak was found at the AFT location in the VIPER experiment, potentially because this mode was not excited, or they were not detected by the pressure transducer (due to the location of the transducer and/or the damping effect of the pressure transducer cavity).

It is noteworthy to compare the influence of the acoustic boundary condition at the inlet by comparing the eigenfrequencies and eigenmodes in Figure 63 with Figure 64. When the acoustic boundary condition is changed, the 1L frequency and modeshape changes as expected but those of the 1T, 1T1L, and 1T1L modes remain unaffected. The change in the inlet acoustic BC is performed without recalculating the LES and updating the mean fields. For the unchanged background mean flow, the transverse modes in the combustion chamber are insensitive to changes in the inlet acoustic boundary condition; that is, the combustion chamber mode is decoupled from the premixing duct. Of course, a change in the acoustic boundary condition in

the LES can still influence the flame shape (via enhancing the combustion) which would result in a different eigenfrequency and modeshape and perhaps vastly different flame dynamics. However, these figures demonstrate and it should be further emphasized that the eigenfrequency is more strongly associated with the mean fields in the combustion chamber than with the acoustic boundary condition at the inlet and outlet (not in general, but for the transverse modes occurring in this VIPER configuration).

Eigenfrequencies: Using Prescribed Profiles

Additional analysis cases have been performed in COMSOL on the same geometry, but simplified background mean flow properties. The inlet and is set to a hard (reflecting) boundary condition. The influence of a hard vs soft acoustic boundary condition has already been demonstrated previously. The mean chamber pressure is set to a uniform level of 7.2 bar in the entire domain. Two temperature profiles are considered which vary only in the axial direction and are uniform at each radial cross-section. In the first case, the gas temperature in the pre-mixing duct before the dump plane ($X < 0$) is set to 680 K. The gas temperature in the 80 mm combustion chamber is set to 2190 K (for all $X > 0$) so that there is a discontinuous jump in temperature from 680 K to 2190 K at $X=0$.

In the second case, the gas temperature is set to 2190 K after 1 jet diameter downstream of the dump plane ($X > 40$ mm). The temperature ramps linearly from 680K to 2190K in the intermediate transition region (0 mm $< X < 40$ mm). The acoustic eigenfrequencies and eigenmodes calculated with the step-wise temperature variation is in Figure 65; corresponding eigenmodes and eigenfrequencies with the temperature ramp is in Figure 66. When the

temperature in the combustion chamber is uniform throughout), the eigenmodes resemble those of a simple cylinder. Most importantly, the acoustic negative and positive regions of acoustic pressure for the 1T mode persist until the very end of the combustion chamber until the exit nozzle is encountered. The 1T, 1T1L, and 1T2L modes also have eigenfrequencies similar to one-another (~6600 Hz).

However, when there is a region of cold gas in the combustion chamber, the 1T mode becomes trapped in the cold region (near the dump plane) which can be clearly seen in Figure 66 and the eigenfrequencies decreases significantly from ~6600 Hz to 5940 Hz. The 1T1L and 1T2L modes are not as affected by the presence of the cold gas because they contain a longitudinal component and these acoustic waves are able to propagate axially; the first pressure anti-nodes for the 1T1L and 1T2L mode are also trapped near the dump plane, but the eigenfrequencies for these modes are not significantly affected compared to the 1T mode. The presence of cold gas (in a hot environment) can significantly influence and alter the acoustic modeshape for even the basic 1T mode.

One can compare the modeshapes and frequencies obtained in Figure 66 with the previous analysis using the background mean fields from LES in Figure 64. The geometry and boundary conditions are identical for these two cases, the only difference is the background temperature field provided for the analysis. However, the eigenfrequencies are still quite far from the ~5600 Hz frequency for the 1T mode and ~6200 Hz frequency for the 1T1L mode and there are notable (qualitative) differences between the modeshapes predicted. In the case of the 1T1L mode for example, whereas the pressure anti-nodes near the dump plane are much weaker than

the subsequent ones downstream in Figure 66, the 1T1L mode persists throughout the entire combustion chamber. On the other hand, both sets of pressure anti-nodes are trapped to roughly the first half of the combustion chamber in Figure 64. Accurate background fields (in addition to geometry and boundary conditions) are required in order to accurately predict the acoustic eigenfrequencies and eigenmodes.

Although these effects on the acoustic modeshapes can be captured in simplified tools, the separation of cold and hot gases in the combustion chamber are determined by the mean flame location (and to some degree the dynamic flame behavior). For case studies where the flame configuration is well-understood, a presumed flame shape may be applied. A presumed flame shape provides the most critical information, the demarcation between the cold and hot gas regions. For example, the single unswirled jet flame can be reasonably approximated by a conical shape (the cone length would also need to be pre-determined from the typical flame length). It is expected that a conical flame shape can reasonably predict the acoustic eigenmodes and eigenfrequencies for this configuration. In general, however, combustion models will need to be applied to accurately predict the flame location and accurate temperature fields for the background flow. Hence, low-order tools cannot do without input from higher-fidelity CFD simulations such as (U)RANS or LES.

Mode Label	Modeshape	Eigenfrequency
1L (½ λ)	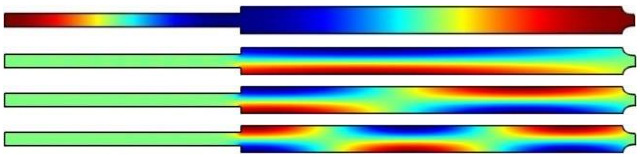	382 Hz
1T		6627 Hz
1T1L		6647 Hz
1T2L		6687 Hz

Figure 65: Acoustic eigenmodes from acpr and piecewise profile

Mode Label	Modeshape	Eigenfrequency
1L (½ λ)	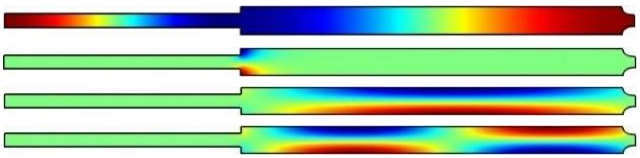	382 Hz
1T		5940 Hz
1T1L		6632 Hz
1T2L		6664 Hz

Figure 66: Acoustic eigenmodes from acpr and piecewise profile with linear ramp

CHAPTER FIVE: FLAME DYNAMICS

Previous chapters discussed the spectrum found at point probe locations measured in the experiment and simulated in the LES and correlated these to the acoustic modes acoustic modes observed from the experiment and LES. Additional analysis is performed in this chapter to dynamic motions.

Mean Flame Results

The mean (time-averaged) reaction regress variable is plotted in Figure 68 at several cross-sectional cuts and the Z = 0 cut-plane in Figure 67. Recall that a regress variable value of 1 corresponds to a completely unburned region and a regress variable of 0 corresponds to a burned region. Hence the region in the premixing passage has values of regress variable near unity because the mixture is unburnt whereas the regions downstream of the combustion chamber are almost entirely 0. Intermediate values of the regress variable (between 0 and 1) indicate regions where reactions are occurring and can be used to visualize the flame.

Figure 67 show the axial extent of the flame persists for nearly 400 mm downstream of the dump plane (10 jet diameters). Figure 67 also contains a V-shaped (or inverted-V shape depending on nomenclature) characteristic of unswirled jet flames. Swirling jet-flames have (M or W shapes due to the establishment of an inner and outer recirculation. However, Figure 68 reveals that the flame shape is not conical as might be expected of a jet-flame issuing from a cylindrical duct into a cylindrical duct. The flame contour near the dump plane is circular, but rapidly but distorts into a non-circular shape as it progresses downstream.

The mean flame shape is important for low-order modeling tasks such as COMSO, because the flame front demarcates the cold and hot regions where gas properties change dramatically (most notably the gas temperature and sound speed). The mean flame shape can be visualized using an isosurface of the mean reaction regress variable, a level of 0.5 was chosen and plotted in Figure 69 in a view normal to the minor axis and normal to the major axis. The width of the flame is approximately constant with respect to the major axis. Only along the minor axis does the flame cross-section decrease continuously with axial extent and terminates in a tip. Thus, rather than terminatnig at a tip-point for a cone, the flame terminates in a flat brush-like shape (it looks like a common house-hold vacuum cleaner nozzle). That is, rather than contracting in an axissymmetric fashion in all directions, the flame contracts one-dimensionally. The flame shape suggests that flapping motions are a possible mechanism. This behavior of the flame shape has been noted before in the study of co-axial jet flames located near pressure nodes and velocitty anti-nodes for liquid rocket engines by Hakim et al. [55]; they noted that for high frequency forcing (greater than the natural frequency of the jet) the flame is flattened and takes on a bulk motion (with no large scale deformation).

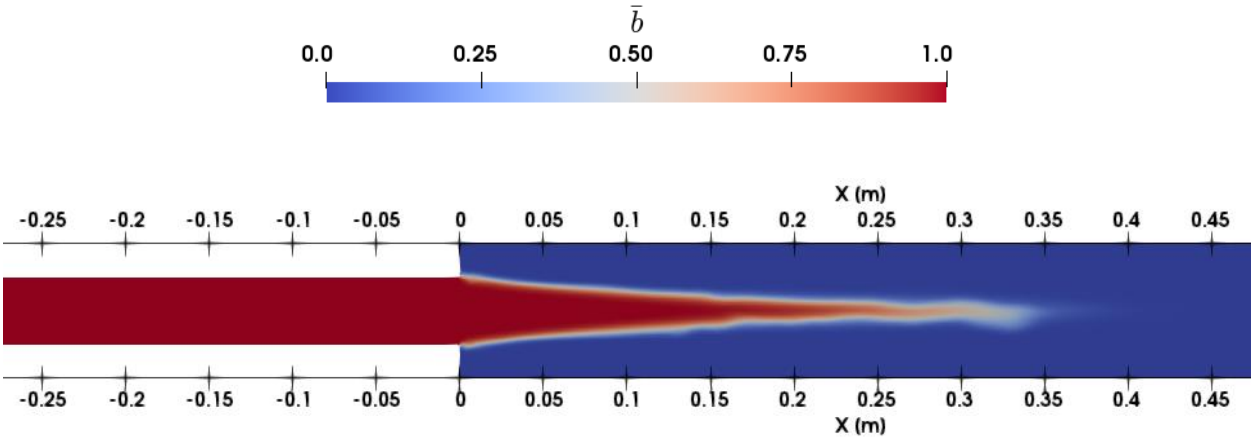

Figure 67: Mean reaction regress variable at Z = 0 cut-plane

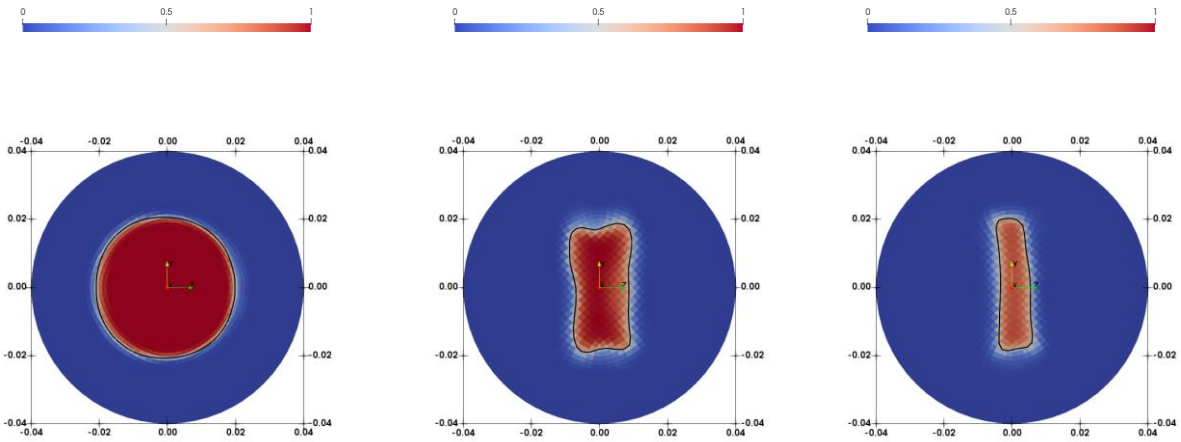

a) X=2 mm b) X=160 mm c) X=280 mm

Figure 68: Mean reaction regress variable at cross-sections a) X=2 mm, b) X=160 mm, and c) X=280 mm

a)

b)

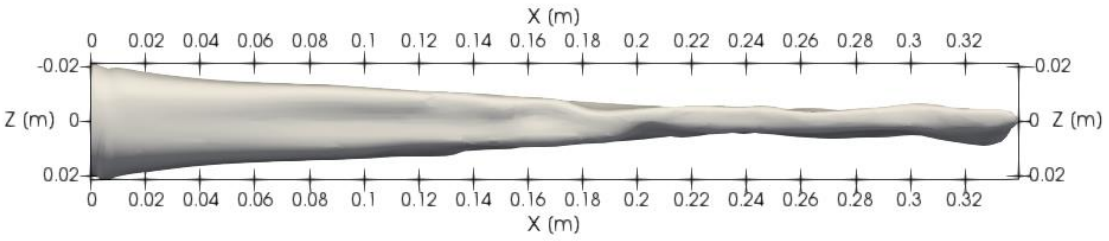

Figure 69: Isosurface of mean reaction regress variable b=0.5 viewed from a) flame major Z-axis and b) flame minor Y-axis

Phase-Average Analysis of Flame Front

Isolines of the regress variable of 0.5 are plotted on the Y=0 and Z=0 planes. The Z=0 plane corresponds to the flame major axis (the wider cross-section of the flame) which passes along the pressure nodes. The Y=0 plane corresponds to the flame minor axis (the narrower cross-section) where the flame front is positioned in the pressure (positive/negative) anti-nodes. The mean progress variable is plotted in black lines. Instantaneous snap-phases of the phase-averaged regress variable are plotted in red lines.

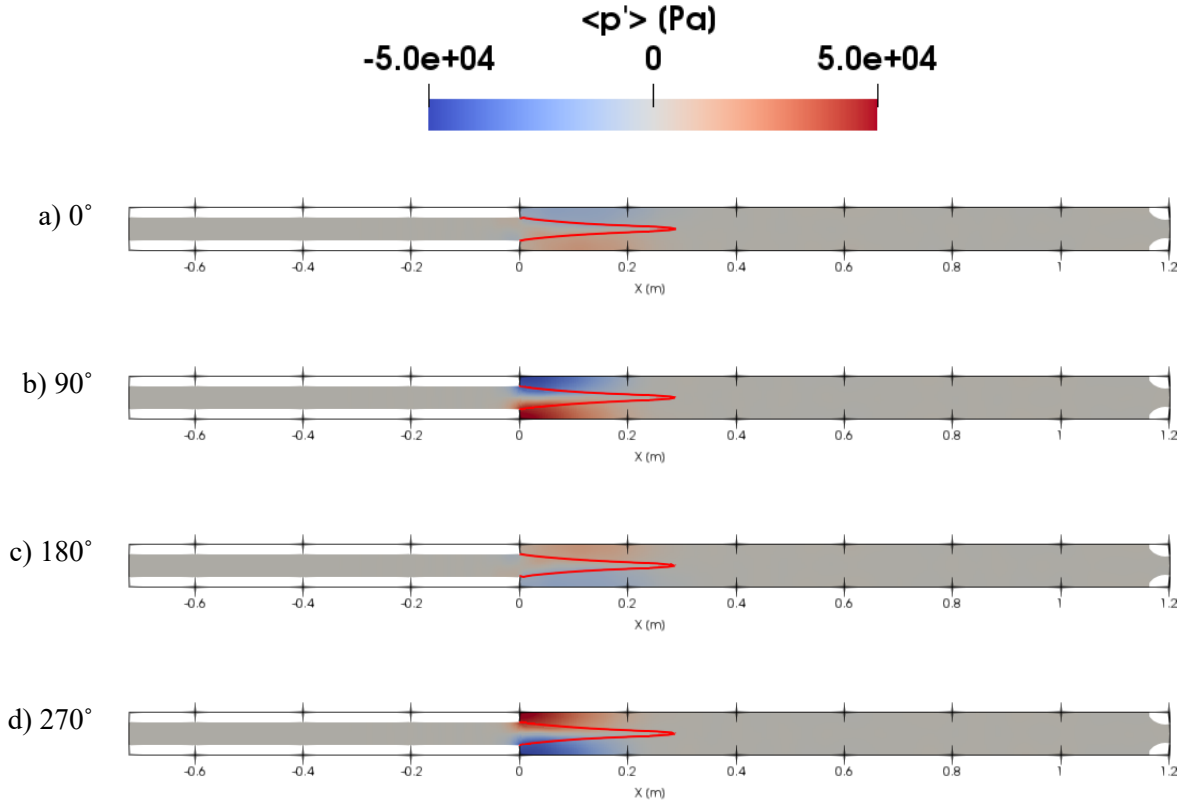

Figure 70: Contours of <p'> averaged over 5600 Hz shown at various phases on Y=0 plane with isoline of regress variable <b>=0.5 (red line)

In Figure 70, the phase-averaged pressure fluctuation (which represents the acoustic pressure) is plotted along the Y=0 plane (the flame minor axis) over the entire domain extent. The flame edge is given in the same figure to visualize the axial extent of the flame. The acoustic pressure amplitude is greater near the dump plane, with a pressure anti-node max/min at the upper and lower parts of the combustion chamber. The acoustic pressure amplitude decays rapidly in the axial direction. Relative to the maximum and minimum amplitudes, the acoustic pressure amplitude near the flame-tip and downstream post-flame region is very small; the pressure amplitude in the premixing duct is also small. Being associated with acoustic modes, there will be some level of amplitude everywhere in the domain. However, it is important to note

that the low levels of acoustic pressure in the premixing duct indicates that the axial mode of the premixing duct is not coupled to the transverse mode in the combustion chamber. This property is demonstrated more definitely in Figure 72, where one notes that the acoustic velocity in the premixing duct is not aligned with the pipe axis. On the other hand, the axial decay of the acoustic pressure amplitude

To better visualize the wrinkles in the flame front, a more zoomed in view is given in Figure 71. Along the flame minor axis, oscillations in the flame front can be distinguished. An already present anti-symmetric oscillation is visible at 0 ˚ phase (an oscillation in the negative z-direction for both the upper and lower parts of the flame). The oscillations propagate downstream until 90˚ degrees phase, the onset of the next oscillation pair begins at around a phase angle of 120˚ degrees. The oscillations are synchronized on the upper and lower parts of the flame (spatially coherent). It is discernable that the black and red lines merge quickly downstream; this indicates that the original pair of oscillations do not continue traveling downstream in a pure propagating wave-like manner but are quickly damped. No more than one wave-crest and wave-trough can be seen for any phase. There are no large scale oscillations in the flame front on the Z=0 plane, Figure 72. This plane is along the pressure nodes where the acoustic pressure amplitude is 0 and the acoustic velocity is predominantly out-of-plane. The wrinkles on the flame front occur near the Y=0 plane, where the velocity oscillations are in-plane.

The fact that these two different behaviors occur in the same configuration suggests that a destabilizing effect occurs on the Y= 0 plane. The acoustic velocity forces the flame and moves

the instantaneous anchoring location, thereby causing oscillations in the flame front. Otherwise, one would observe oscillations also along the Z=0 plane. If this is the destabilizing mechanism, that means we can probably focus on this region to stabilize the excitation mechanism. Geometric changes (or maybe heat transfer at the walls) might be able to better maintain the flame anchoring and make the jet flame more robust against acoustic instabilities.

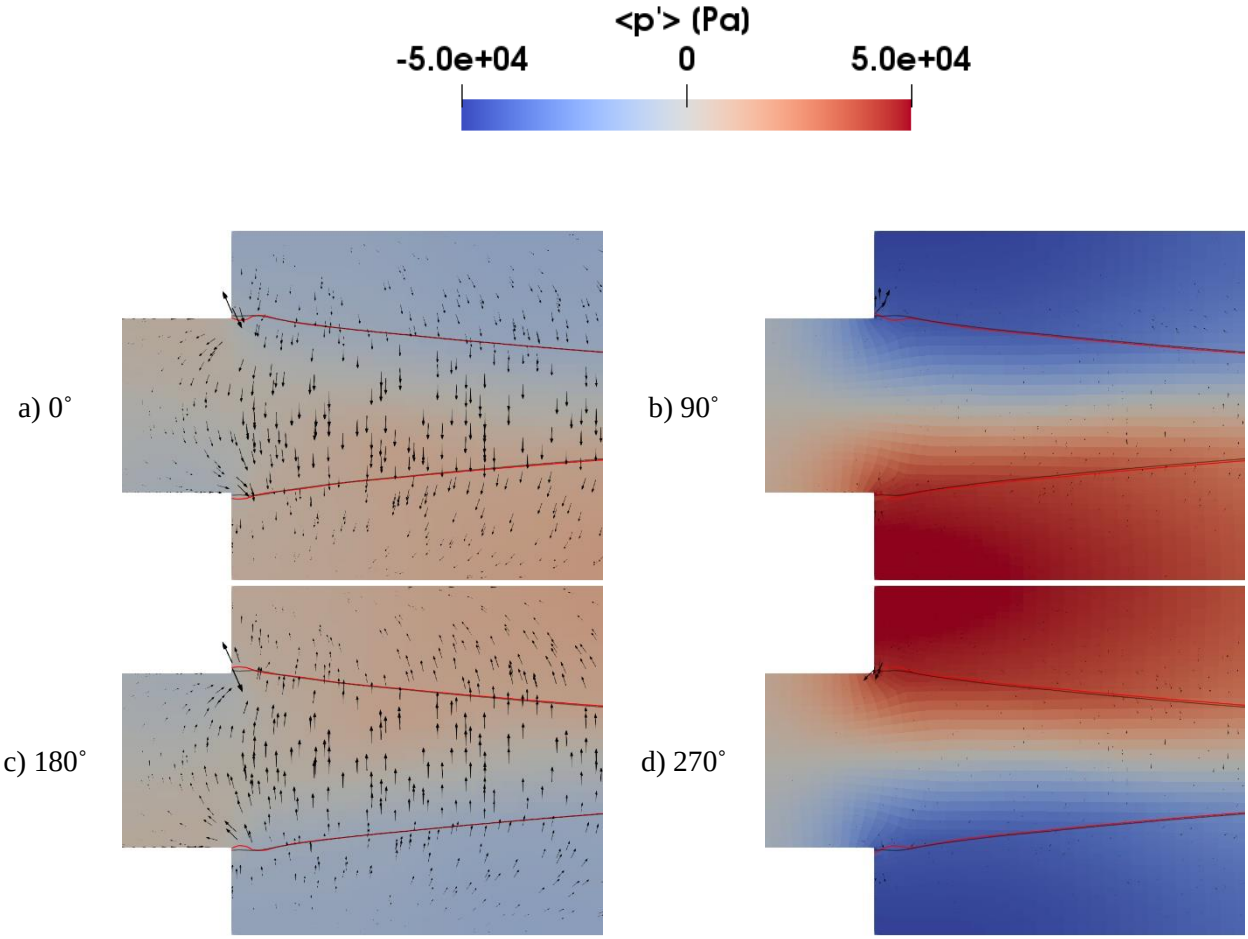

Figure 71: Contours of <p'>at various phases on Y=0 plane with isoline of regress variable <b>=0.5 (red line) and vectors of <u'>

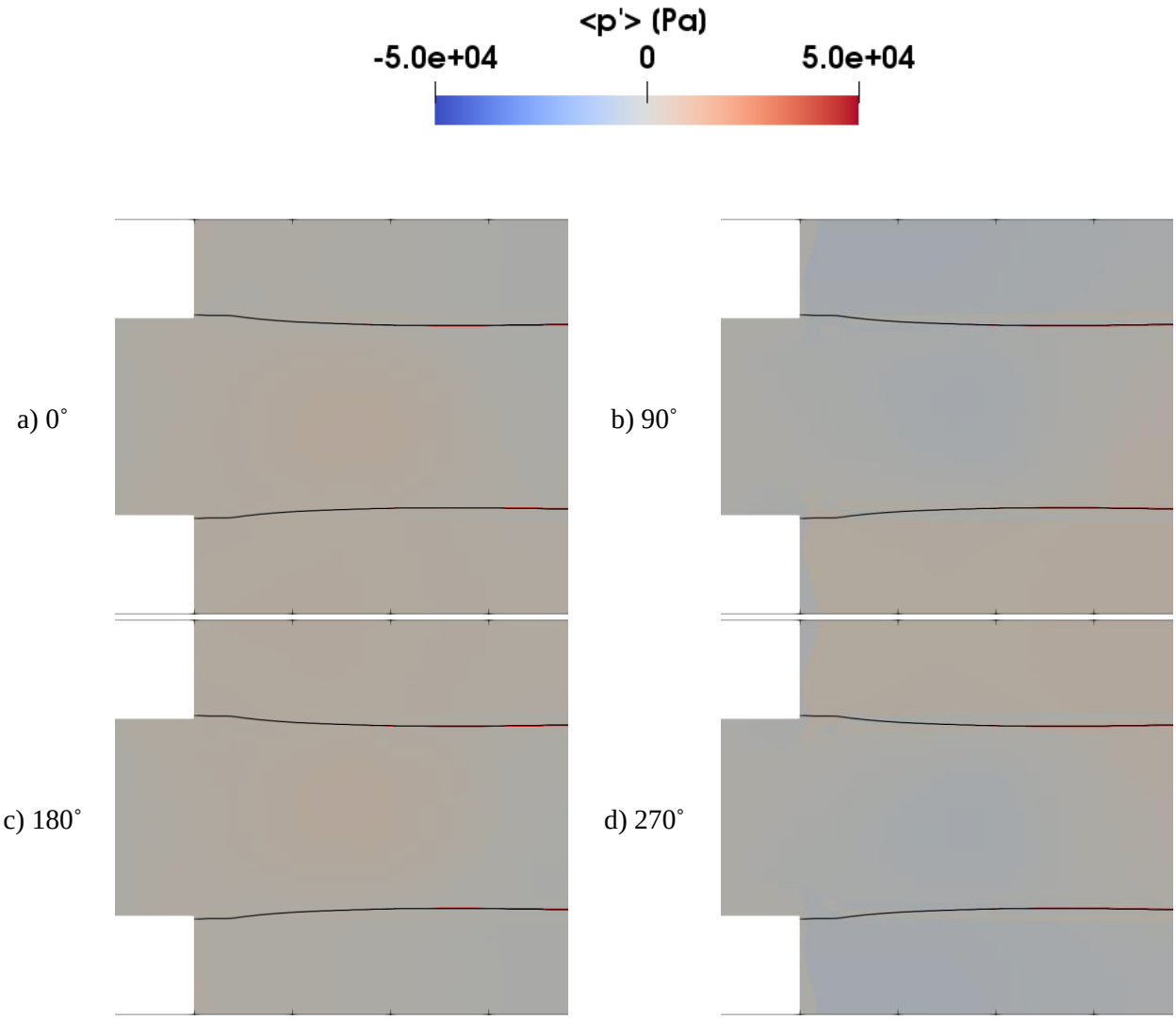

Figure 72: Contours of <p'> at various phases on Z=0 plane with isoline of regress variable <b>=0.5 (red line)

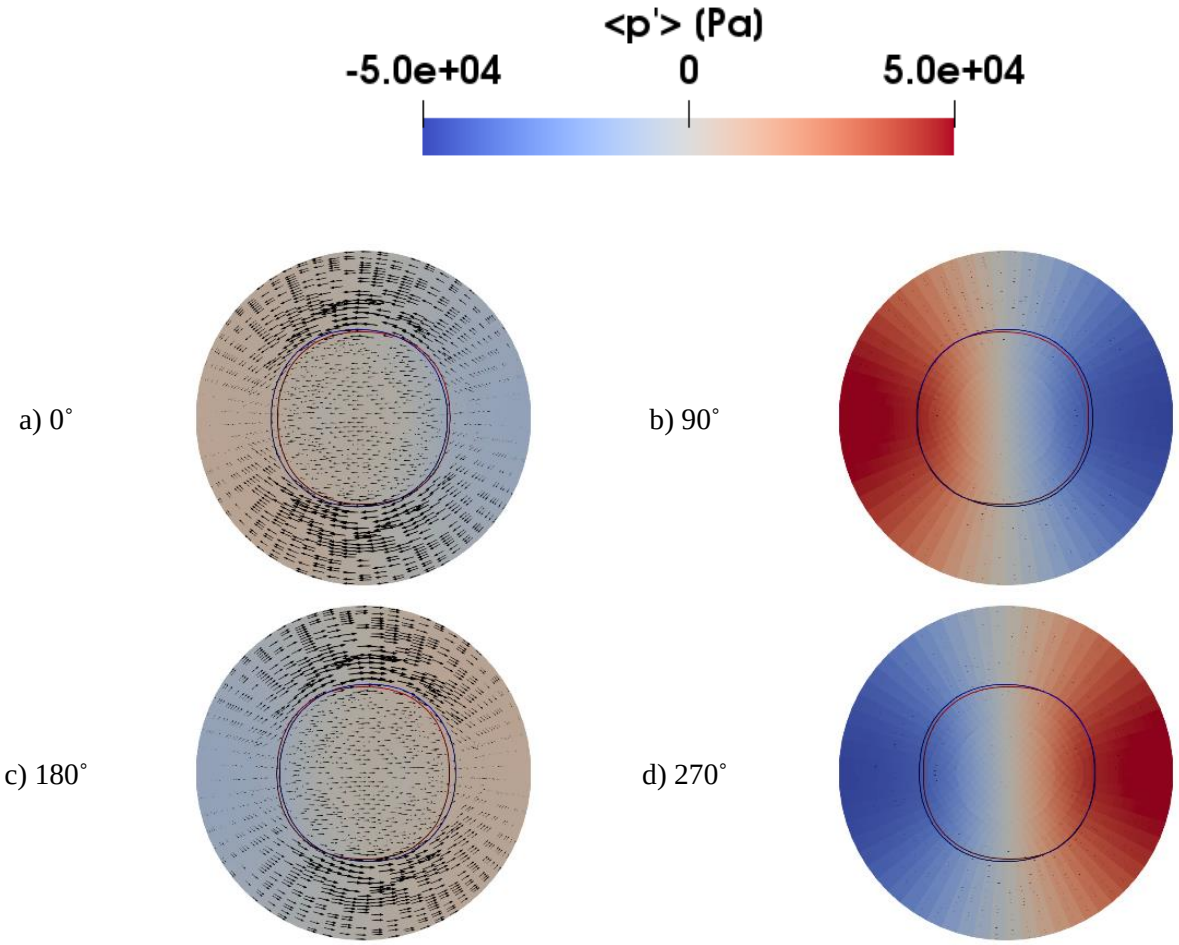

Figure 73: Contours of <p> averaged at 5600 Hz plotted at various phases on X=2 mm plane with isoline of regress variable (<b>=0.5) at X=2mm (blue line) and at X=6mm (red line)

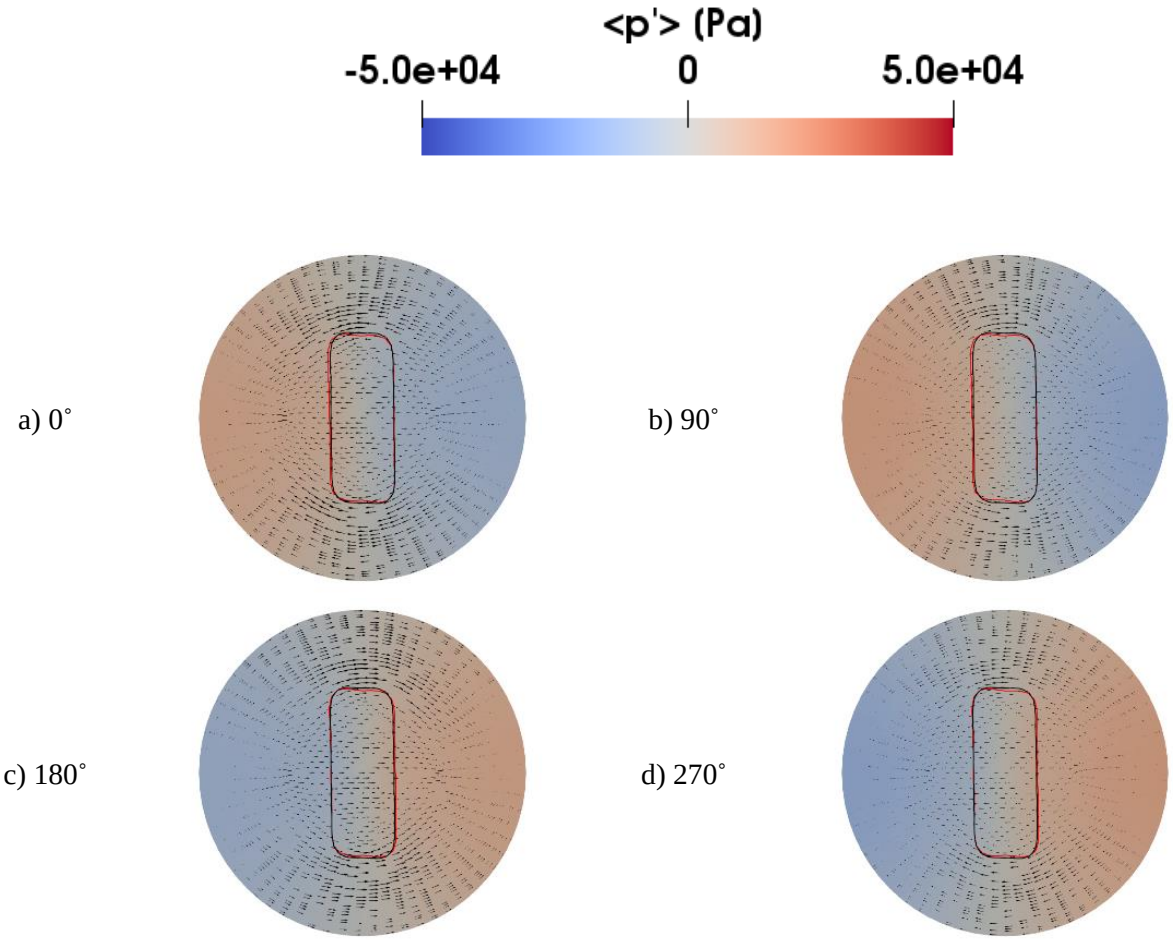

Figure 74: Contours of <p>at various phases on X=160 mm plane with isoline of regress variable <b>=0.5 (red line) and mean b = 0.5 (black line)

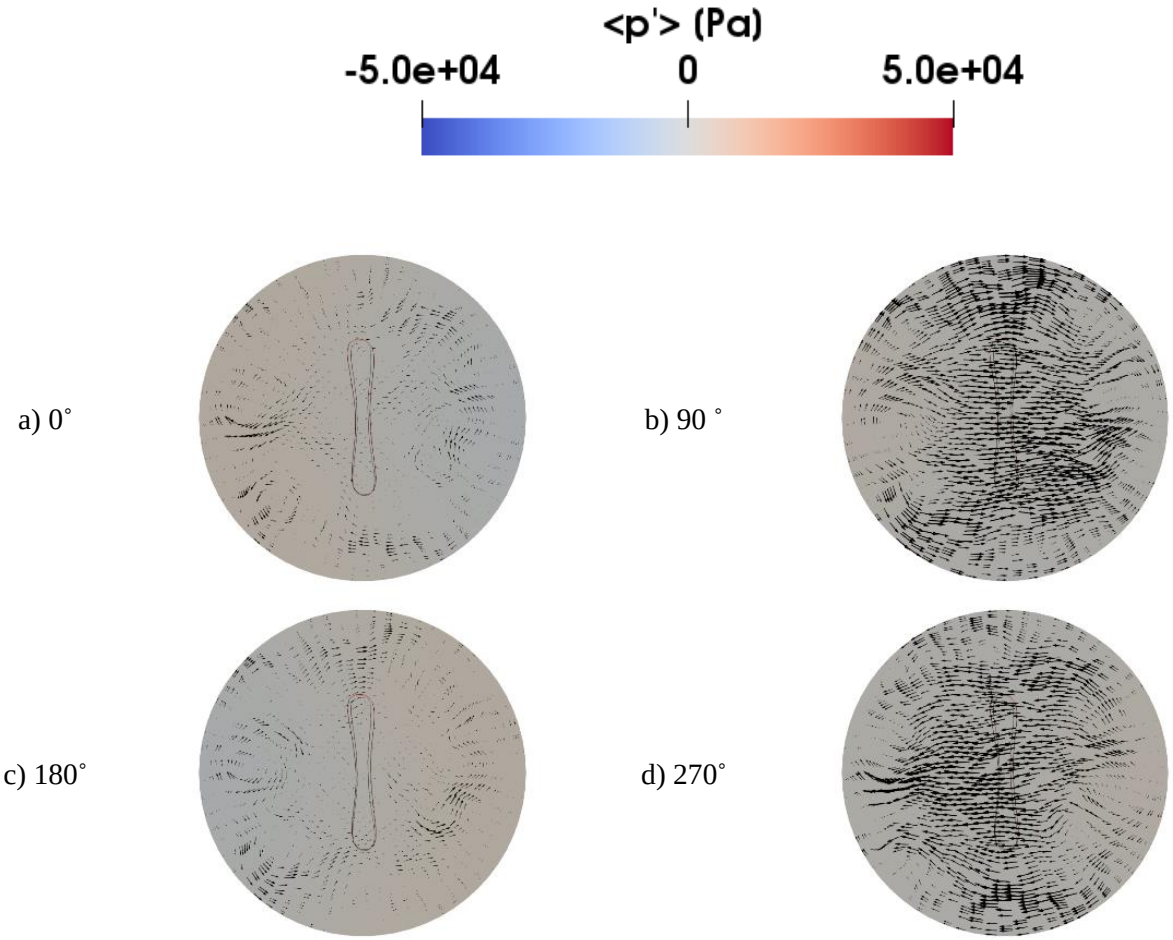

Figure 75: Contours of <p>at various phases on X=280 mm plane with isoline of regress variable <b>=0.5 (red line) and mean b = 0.5 (black line)

Similar plots are generated at cross-sectional slices near the dump plane in Figure 73, at the X=160mm axial location in Figure 74 and near the flame tip at X=280mm in Figure 75. Two colored isolines are drawn in Figure 73 depicting the flame edge at two different but close axial locations. The flame contour at X=2mm is blue and the flame contour slightly downstream is colored red. At a phase of 0˚, the acoustic velocity direction is left, and the blue curve is eccentrically on the left compared to the red curve. At a phase of 90˚, the acoustic velocity is now neutral (zero) and the blue curve occupies the same position as the red curve. At a phase of 180˚, the acoustic velocity direction is rightward, and the blue curve has shifted to the right. At a phase of 270˚, the red curve has again caught up to the blue curve. This sequence of images indicates that the oscillation at the downstream X=6mm location follows the oscillation at X=2mm but delayed in time. When combined with Figure 71, it demonstrates that the initial oscillation occurring at the dump plane propagates downstream in a whip-like manner characteristic of a propagating disturbance.

The bulk displacement of the flame contour is very small relative to the geometric scale of the jet-flame; however, the flame contours at the Z=0 plane over the entire flame length are provided in Figure 77 for completeness. Notice that these flame front oscillations are not found in further downstream location, they decay rapidly in the axial direction. The acoustic pressure amplitude downstream at X=160mm is less than nearer the baseplate. As previously discussed, the flame brush transitions from circular at the dump plane exit to a distorted shape further downstream. The major axis of the flame brush aligns itself along the pressure node line (which spans the Z=0 plane). The pressure nodal line is more easily visualized at phases of 90˚ and 180˚ degree of Figure 73 at the more upstream location where the pressure fluctuation magnitudes are

greater; the orientation of the flame brush is more easily visualized further downstream where the shape is more distorted in Figure 74 and even more so near the flame tip in Figure 75.

Apart from the oscillations in the flame front near the dump plane, the large-scale behavior of the flame can be more easily obtained by considering Figure 74 and Figure 75. The regress variable lags behind the direction of the acoustic velocity. At 0 phase, the acoustic velocity direction is right-to-left. From 0˚ to 90˚ phase, the flame edge moved left. At 90˚ phase, the acoustic velocity is beginning to switch directions. From 90˚ to 180˚ phase, the flame edge has moved rightward and continues to move right through a phase of 270˚.

The dynamic flame behavior can be broadly characterized by two distinguishable phenomena. The first occurs near the dump plane consists of sinusoidal oscillations in the flame front. It is not clear yet whether these are due to hydrodynamic vortex shedding or large-scale flame wrinkling. In the region further downstream, the initial oscillations are damped out and the remainder of the flame moves in a bulk fashion. This behavior downstream seems to correspond to the flame displacement mechanism of Hummel et al. [63] and Hakim et al. [55]

A notable feature not present in any of the cross-sections is a wrinkle in the circumferential (or azimuthal) direction. That is, the flame contours are smooth (e.g. eccentric but wrinkle-less circles in Figure 73), indicating that helical modes are not present in this configuration. That is, we do not observe axisymmetric vortical structures in the flame contour nor do we find the non-axisymmetric & helical structures observed in swirling jet flames. However, an eccentric oscillation of the flame front is present near the baseplate caused by a

superposition of the bulk flame displacement and a downstream propagation of the oscillations in the local anchoring point.

We also noted the lack of any axial pumping at 5600 Hz which would result in a flame breathing mode (and show up as a perfectly axisymmetric motion of the flame front). It is hypothesize-able that under different conditions or configurations, these might occur. That is, flame breathing mechanism might become more important when the premixing duct is acoustically coupled with the combustion chamber. Or, at other operating conditions that result in stronger thermoacoustic instability (much higher amplitudes), both the flame breathing and flame displacement effects might appear together.

The flame front tracking via the reaction regress variable is a binary delineation of unburnt vs burn gas regions. When tracked using a contour of any particular value of the regress variable, it provides only a description of the flame location and does not provide any indication of the flame intensity or flame thickness. The burning rate provides this additional quantity. The phase average of the heat release oscillation is plotted in Figure 76 and Figure 77. The heat release was scaled based on the burning rate (fuel consumption rate). The fuel consumption rate was calculated based on the source term in the regress variable equation in OpenFOAM and then scaled using the fuel heating value of natural gas (the heating value was approximated using 50 MW/m^3)

At 0˚ phase, the pressure is most negative at the top and most positive at the bottom. At the same time the acoustic velocity is upwards. The bulk flame motion under the action of the acoustic velocity causes both the upper and lower parts of the flame to move from a region of

low acoustic pressure into a region of high acoustic pressure. Hence the unsteady heat release is enhanced on the inner-side of the upper part of the flame and on the outer-side of the lower-part of the flame corresponding to the motion of the flame front. Similarly, the unsteady heat release is negative on the outer-side of the upper-part of the flame and inner-side of the lower-part of the lame due to the evacuation of the flame front from these regions.

The flame front oscillation immediately at the baseplate location, occurring in-phase with the bulk flame motion significantly amplifies this trend (becoming more positive and more negative). On the other hand, the subsequent out-of-phase oscillation downstream deviates from the bulk flame motion and causes the opposite, alternate trend to occur in the heat release. When the bulk flame motion is downwards, the out-of-phase oscillation is upwards and causes the heat release to be positive on the outside and negative on the inside of the upper part of flame.

Between 30˚-60˚ phase, there is a node of the oscillation on the burner face. During this phase, we see similar levels of heat release on the upper and lower parts of the flame. But there is an upward crest near the dump plane for both the upper and lower parts of the flame. The flame front is on its way moving downward following this wave. When this happens, there is a region of more intense heat release on the inner-side of flame near the apex of the burner lip on the upper side visible at a phase of 90˚. The upper flame front continues to move towards the apex of the corner and the heat release grows in magnitude and reaches a maximum at approximately a phase of 180˚, completing the downward trough motion of the wave. Subsequently this heat release weakens as the flame front oscillates upward, returning to the nodal position at a phase of ~270˚. As the flame moves upward, similarly the heat release grows in the lower part of the

flame in a similar fashion. It is noteworthy that throughout this oscillation cycle, the sign of the heat release fluctuations is positive on the convex side and negative on the concave side of the oscillations in the flame front.

On the other hand, the subsequent out-of-phase oscillation downstream deviates from the bulk flame motion and causes the opposite, alternate trend to occur in the heat release. When the bulk flame motion is downwards, the out-of-phase oscillation is upwards and causes the heat release to be positive on the outside and negative on the inside of the upper part of flame.

Due to the spatial decay of the oscillation amplitude, the positive and negative enhancement of the heat release for the downstream out-of-phase counter-oscillation is weaker than the initial disturbance at the baseplate. Thus, the net effect of the downstream oscillations is to partly counter-act the effect of the initial disturbance. In this scenario, the net effect of the flame front oscillations is well-correlated to the strength of the initial disturbance. However, it is imaginable that in other configurations where the oscillations are more unstable (a hydrodynamically neutral or unstable case), the oscillations can maintain their amplitude or even grow in amplitude. When these spatially growing oscillations occur, the out-of-phase oscillations can counter-act more than bulk flame motion driving the instability. It may be possible to damp a thermoacoustic mode by tuning it to occur at a hydrodynamic mode.

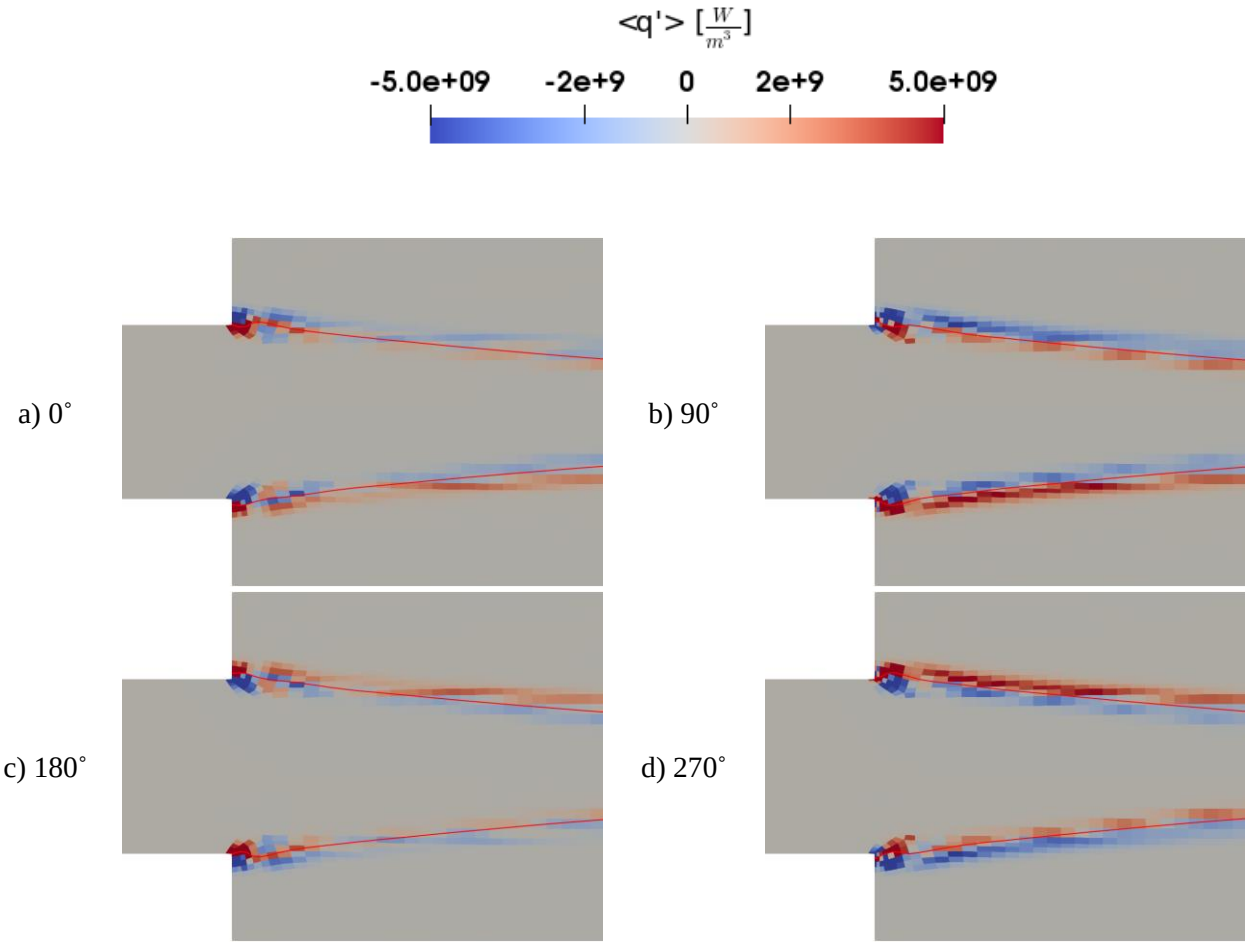

Figure 76: Phase-averaged <q'> at various phases on Y=0 plane

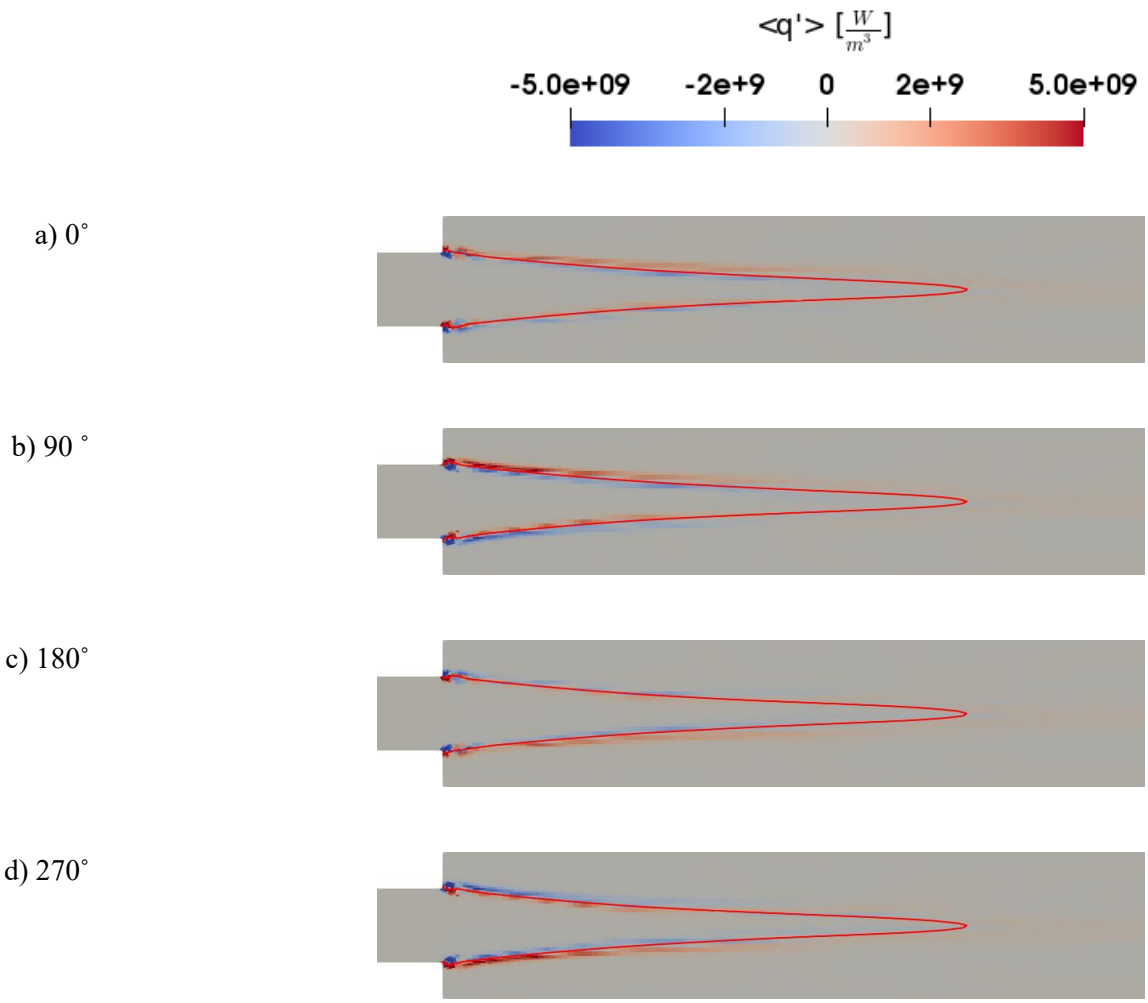

Figure 77: Contours of <q'> averaged over 5600 Hz shown at various phases on Y=0 plane with isoline of regress variable <b>=0.5 (red line)

The product of the acoustic pressure and unsteady burning rate is plotted in Figure 78. The product of the pressure fluctuation and unsteady heat release is the argument which, when integrated of time and space, yields the Rayleigh Index. The products are positive when the acoustic pressure and unsteady heat release both have the same sign and negative when they have opposite sign. Thus, a positive product arises when the two signals are in-phase and

negative when they are out-of-phase. The products are positive out the outside of the flame (in the burnt regions) and negative inside the flame (in the unburnt regions) and the amplitude is modulated over the cycle, except for the small region near the baseplate where the opposite trend occurs due to the flame front oscillations.

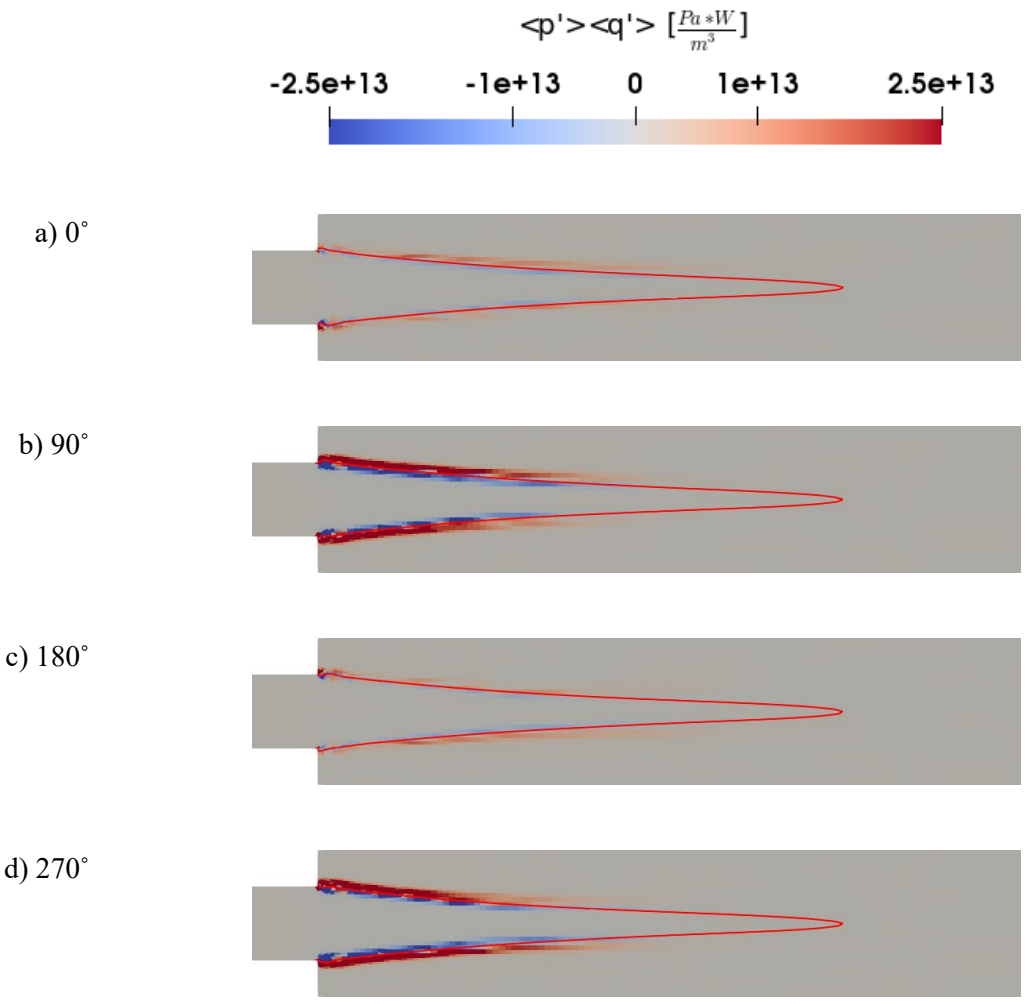

Figure 78: Contours of <p'><q'> averaged over 5600 Hz shown at various phases on Y=0 plane with isoline of regress variable <b>=0.5 (red line)

It is commonly reported that the oscillatory heat release is caused by the axisymmetric vortex shedding, which is generated by strong axial flow fluctuations in the inlet duct. To reinforce this hypothesis, Smith et al. [87] investigated (swirled)jet-flames subjected to various degrees of coupling between the axial fluctuations and transverse fluctuations, by attempting to suppress the axial fluctuations. Accredited to Acharya et al. [88] is that non-axisymmetric modes do not contribute to the global heat release and significant oscillatory heat release rates (due to axisymmetric modes) are found only when there is a pressure anti-node near the jet exit. Smith et al. concluded that axial flow fluctuations in the upstream ducting are responsible for the axisymmetric vortex shedding and therefore cause the oscillatory heat release.

The current findings do not (necessarily) contradict the hypothesis of Smith et al. In the perfectly premixed configuration of VIPER-S, there a pressure node along the jet center (the distinction that the acoustic waves are generated by external forcing or internally self-excited is not different phenomenologically). Strong axial pulsations (due to the premixing duct being acoustically de-coupled) and axisymmetric motions in the flame edge were not observed in the current work. In the current work, the longitudinal mode of the premixing duct is decoupled from the chamber mode and there is no axial pumping at 5600 Hz. It is hypothesized that when the premixing duct is coupled with the chamber mode, axisymmetric vortex shedding will appear (induced by the axial fluctuations) that will provide an additional driving mechanism. However, the notion that the axial pumping and subsequent generation of axisymmetric vortical structures are the only means via which a transverse acoustic mode may be excited deserves to be challenged.

The large scale wrinkles in the flame front are caused by the displacement of the flame front in the vicinity of the baseplate. The size of the flame oscillation is likely proportional to the acoustic velocity amplitude and inversely proportional to the acoustic frequency. These wrinkles then propagate downstream at the group velocity, decaying rapidly. It is hypothesized that the decay rate of these wrinkles can be predicted by hydrodynamic instability theory. If the decay/growth rate of a perturbation could be accurately predicted following hydrodynamic instability theory (or some other means) then one would have a prescription for predicting the size and number of wrinkles in the flame. These wrinkles were not reported by Smith et al. [87], Hummel et al. [63], nor Hakim et al. [55] but is present in the current as an additional, independent mechanism for the unsteady heat release. As a historical note: these wrinkles were observed, in the work preceding that of Hummel et al. [63], by Schwing et al. [60, 61, 89] and Zellhuber et al. [56, 64] and explicitly referred to as a vortex. However, Schwing et al. [61] noted that the vortex shedding principle is in disagreement with the general trend that their combustor is unstable over a broad operating range. Although shear layers are susceptible to broad range of frequencies, shed vortices have a distinct convective time-lag. Thus, Schwing & Sattelmayer [89] concluded that vortex shedding is likely not a driving mechanism (for their combustor) and the mechanism was not included in the later theoretical models of Hummel et al. [63]. The presence of vortex shedding has observed and acknowledged by some investigators, but even when observed the coupling between the vortex shedding and its participation in the thermoacoustic feedback cycle has been debated (even ruled out by Schwing et al. and co).

Due to the high frequency acoustic modes in the current work (> 5000 Hz), the flame front wrinkles are not spatially resolved on the computational grid (the core cell size is on the

order of 4mm, and the oscillation length is also around the same size). Thus, it cannot be determined whether the wrinkles in the flame front are vortex shedding or not. If vortex shedding is present, one would be able to see pockets of burnt gases trapped inside regions of unburn gases (bubbles with regress variable values near unity trapped inside the bubble with the regress variable nearly zero outside). These pockets are formed from the shear layer rollup near the dump plane. The jet shear layer at the dump plane imparts a circulation onto the flow and the flow immediately in the vicinity of the dump plane tends to roll up, ingesting hot burnt gases inside regions of fresh unburnt gases. This vortex shedding is well described and documented in the numerical simulations by Zellhuber et al. [64] and experiments of Schwing et al. [61] from Mie-scattering images. However, due to the insufficient spatial resolution of the current computational grid, this roll up event was not observable, and it cannot be clearly confirmed that the wrinkles in the flame front are vortex shedding events. However, the wrinkles propagate downstream at the convective velocity, which is the same speed that a vortex would propagate at. The characterization of the flame front wrinkles and the identification of vortex shedding is furthered hampered by the high oscillation frequency (> 5000 Hz), resulting in a small initial size of the oscillation/vortex. For lower frequencies at the same acoustic velocity amplitude, the oscillations would be larger and more easily characterized. Furthermore, whereas several well-defined vortices can be seen in the Mie-scattering images of Schwing et al. [61], the oscillations in the current work decay rapidly (only a single oscillation can be clearly identified in the contours). The rapid rate at which the oscillations decay is likely due to the strong spatial stability at this frequency range.

The impact of the flame displacement mechanism has only been explored and accepted in a limited number of configurations (three so far). It is unreasonable to assume the flame displacement mechanism is the main driving mechanism for all flow scenarios, out-competing all other mechanisms. It is agreeable that the flame displacement mechanism is an intrinsic mechanism occurring in all thermoacoustic systems. In general, however, the flame displacement mechanism will be occurring simultaneously amongst other processes and the general thermoacoustic feedback will be a superposition of multiple processes (with the flame displacement mechanism being one guaranteed mechanism). The flame displacement mechanism is known to have a clear dependence on the thermal power of the combustor (which scales with the combustor flow rates); this dependence on the thermal power was one of the reasons the flame displacement mechanism was not readily apparent in earlier works in atmospheric pressure studies, where the thermal power is much lower. Although the flame displacement mechanism provides a novel explanation and sufficiently agrees with the thermoacoustic coupling process in the current work and the previous works [56, 60-64, 89-92], the impact of vortex shedding should not always be disregarded.

It should be reiterated that vortex shedding has been clearly identified in other past works and may be present in the current work. When considering the flame displacement mechanism by itself, the flame always moves in-phase with the acoustic velocity and always leads to a net positive Rayleigh Index. The large scale flame wrinkles on the other hand are alternating in-phase and out-of-phase. Concurrent with the large scale flame wrinkles, the heat release fluctuation is positive on the convex side of the flame wrinkle and negative on the concave side of the wrinkle. For the in-phase oscillation, the wrinkles augment the flame displacement and

further increase the coupling between the unsteady heat release and acoustic pressure. At the following downstream the whip-like counter-oscillation of the flame front, the heat release fluctuation for this counter-oscillation is anti-coupled from the motion of the flame front induced by the acoustic velocity according to the flame displacement mechanism (the counter-oscillation is out-of-phase with the acoustic velocity). The alternating in-phase and out-of-phase flame front oscillations associated with the hydrodynamic oscillation may decouple or weaken the net coupling between the heat release and acoustic pressure. It hypothesized that this effect may be exploitable under certain conditions. In the current work the acoustically-induced flame front oscillations decay rapidly downstream and only a small portion of the flame in the immediate vicinity of the dump plane is affected by the wrinkles, the downstream part of the flame is dominated by the flame displacement mechanism. It may be possible to design a combustion system such that the large scale flame wrinkles appear over the entire flame brush and the downstream region where only the bulk flame displacement mechanism occurs is no longer distinguishable, becoming embedded within the large scale wrinkles. These more prevalent wrinkles could be obtained at conditions where the spatial decay rate is lower (more stable). It seems reasonable to suggest that these spatial decay/growth rates might be obtained from the spatiotemporal analysis within hydrodynamic instability theory. The effect of the more stable hydrodynamic oscillations is to weaken the relative coupling of the flame displacement mechanism to the heat release and make the combustions system acoustically more stable or, in extreme cases, prevent the transverse modes from being excited. Since the frequency response of hydrodynamic instabilities is broadband, this hydrodynamic damper would also be robust and respond well to changes in operating conditions. This broadband response is important since the

flame displacement mechanism is always present for all acoustic eigenfrequencies. Additionally, the size of the large scale wrinkles is proportional to the acoustic velocity amplitude. As the acoustic instability amplitude increases, the increased size of the wrinkles allows them to have a greater interaction with the heat release fluctuations. It would be interesting to explore a hydrodynamic instability based damping approach in future work and see whether it could be applied in a practical system.

Figure 79 is a compound plot equivalent to Figure 70, but phase-averaged at 6090 Hz; Figure 80 is phase-averaged at 6590 Hz. At 6090 Hz, the acoustic velocity amplitude has more features than at 5600 Hz. There is a pressure node (and velocity anti-node) near the base of the flame and near the flame tip. Near these pressure nodes the acoustic velocity is predominantly up-down as was in the 5600 Hz 1T mode. However, the acoustic velocity acts in different directions at the flame base compared to the flame tip because these regions are out-of-phase. At 0˚ phase the acoustic velocity direction is upward near the flame base and downward near the flame tip, similarly at 180˚ it is downward at the flame base and upward near the flame tip. A notable feature present at 6090 Hz but not 5600 Hz is the axial direction of the acoustic velocity that occurs in the intermediate region between the flame base and flame tip. That is, near the combustion chamber walls, the acoustic velocity direction is in an axial direction. Furthermore, as can be seen at 0˚, the direction is rightward at the upper part of the figure and leftward at the lower part of the figure. The axial velocity fluctuations are also out-of-phase. This longitudinal part of the acoustic velocity cycle occupies a significant portion of the flame and does not contribute to the bulk flame displacement because it is aligned with the contour of the flame front (rather than acting across it); and this feature explains why the 6090 Hz mode has a lower

pressure amplitude compared to the 5600 Hz mode. The 6090 Hz is also driven by the bulk flame displacement mechanism (even though the base and tip are displaced in opposite directions) but is less significant due to the longitudinal character of the 6090 Hz 1T1L mode.

The features of the 6590 Hz mode are similar to that of the 6090 Hz mode, except that the pressure amplitude is greater near the flame tip than the near the flame base. Consequently, the acoustic velocity magnitude is greatest near the flame tip. Due to the modeshape at 6590 Hz, there is less acoustic-flame interaction. There are additional zones where the acoustic direction is axial and fewer zones where the acoustic velocity is in the transverse direction (a smaller region at the flame base and flame tip compared to 6090 Hz). Not visible at 6090 Hz or 6590 Hz are the oscillations in the flame front near the baseplate; which is likely due to the lower acoustic amplitude (compared to the amplitude at 5600 Hz) at this location for the higher frequencies; the oscillation is not strong enough to force a large enough oscillation to be seen in our simulation. At higher frequencies these oscillations would also be damped out faster than at 5600 Hz. Simulations with much higher spatial resolution in this region might be able to resolve these oscillations. Despite our inability to resolve these oscillations, it is hypothesized that they should contribute less to the unsteady heat release (based on our current understanding of the driving mechanism) than at 5600 Hz. It is also noteworthy that that the acoustic velocity direction in the premixing duct near the dump plane is also not in the axial direction even for 6090 Hz and 6590 Hz. These higher frequencies do contain longitudinal components and can propagate into the premixing duct. However, they do not propagate into the premixing duct because the premixing duct it is not coupled to the acoustic mode of the combustion chamber (the premixing duct is not resonating with the combustion chamber).

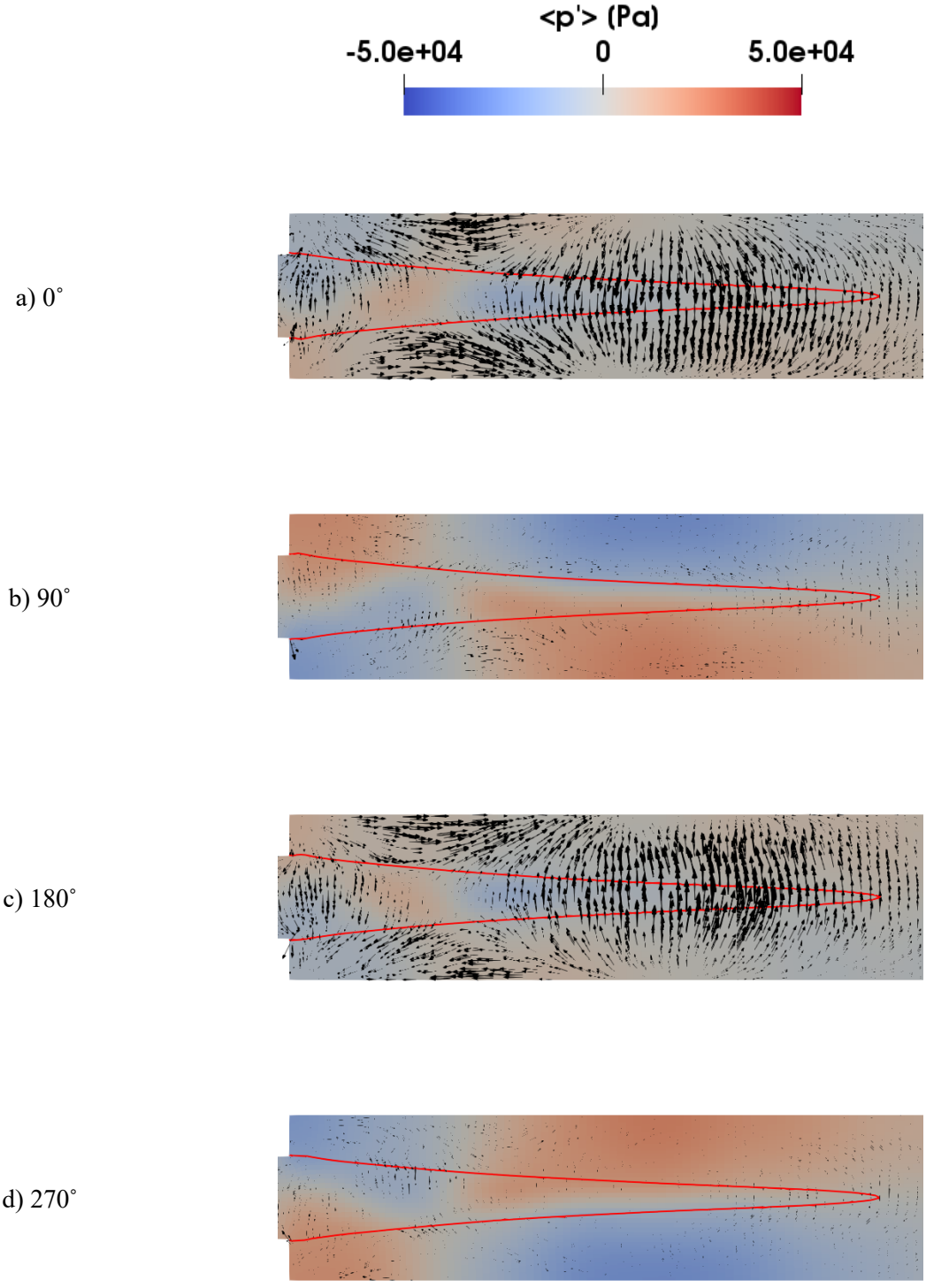

Figure 79: Contours of <p'> averaged at 6090 Hz shown at various phases on Y=0 plane with isoline of regress variable <b>=0.5 (red line)

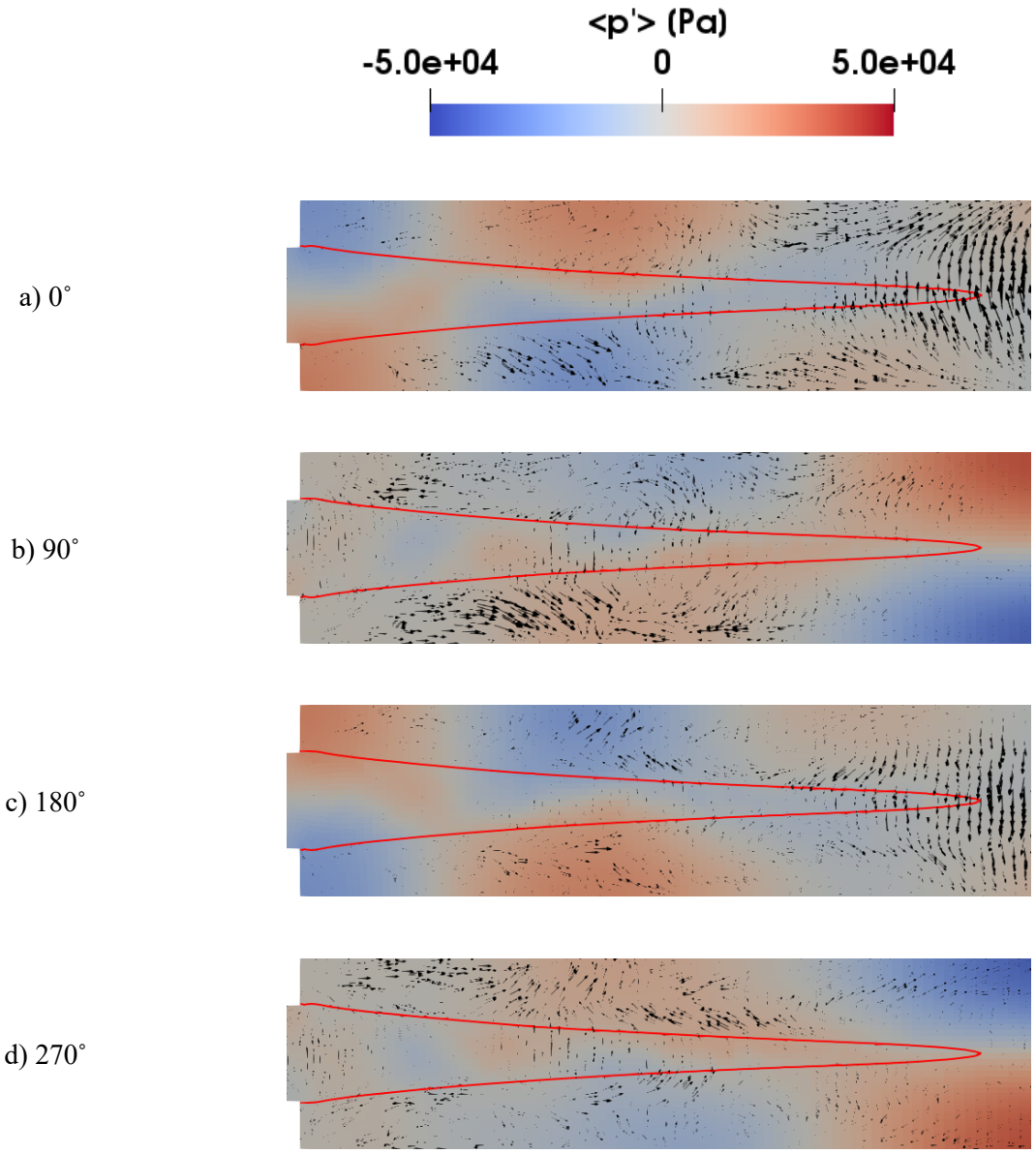

Figure 80: Contours of <p'> averaged at 6590 Hz shown at various phases on Y=0 plane with isoline of regress variable <b>=0.5 (red line)

CONCLUSION

Self-excited thermoacoustic oscillations were observed in a cylindrical dump combustor, prompting a more detailed numerical study to investigate the potential mechanisms involved. The system supports solutions that are not axisymmetric (the 1T and 1T1L modes were excited), despite the boundary conditions and geometry being axisymmetric: the combustor and premix tube are both cylindrical and aligned on the same axis. The mean flow is expected to be axisymmetric in the absence of acoustics but non-symmetric solutions under the action of acoustic modes were observed. The mean flame shape is distorted by the acoustic field, resulting in a non-conical flame. Predicting the correct modeshape and frequency using low-order models requires the correct gas properties distribution (most importantly, temperature and density), and the distributions depend on the mean flame shape. Using an oversimplified field (such as a flat 1D flame) would result in an incorrect modeshape. Even if the frequency appears to be close, the predicted modeshape may not represent the acoustic conditions in the combustion chamber. For example, the axially decaying acoustic pressure amplitude was not predicted when a simple jump discontinuity at the dump plane was used for the temperature profile. Using the mean fields from LES, COMSOL predicted the same modeshapes as the self-excited LES. The thermoacoustic instability in this configuration was predominantly driven by a bulk flame oscillation in the transverse direction caused by the local acoustic velocity oscillations. That is, the flame front locally responds to the local acoustic velocity, and not to any upstream perturbation traveling along the mean flow. Since the acoustic mode is spatially coherent, the entire flame tends to move together in a bulk fashion. The currently accepted hypothesis is that transverse acoustic oscillations drive axial pulsations in the premix tube, which results in hydrodynamic oscillations

along the flame. Our observations contrast with this hypothesis for the dominant mechanism. However, the hydrodynamic oscillations were still observed, leading to large scale wrinkles of the flame front near the baseplate that exhibited a whip-like behavior that allowed the flame to move both in and out of phase with the acoustic velocity oscillation. The initial oscillation at the baseplate was clearly induced by the acoustic velocity. The out-of-phase whip-like motions cannot be predicted by the bulk displacement mechanism. But these oscillations are dominant only locally near the baseplate, the overall instability is still driven by the local displacement mechanism. The cases studied were spatially stable, with the large scale wrinkles decaying rapidly. Hence, it can be hypothesized that at hydrodynamically less-stable conditions, the large scale wrinkles can persist farther downstream, and thus become the dominant mechanism. In addition to these two mechanisms, the acoustic oscillations also alter the mean flame shape, changing the location of the unsteady heat release, which determines the limit cycle pressure amplitude in the combustor. In general, one can expect the thermoacoustic feedback process, even for a single premixed flame, would be a superposition of all three mechanisms (and more). Thermoacoustic models need to account for all three of these mechanisms for accurate prediction of limit cycle amplitudes, not just the individual independent mechanisms but also their combined interactions with one-another. The linearized flame displacement/deformation mechanisms can be predicted easily with acoustic fields calculated with available low-order tools (e.g. COMSOL) using background flow fields as inputs. The flame oscillations due to hydrodynamic oscillations cannot be predicted as easily using low-order models. Current predictive capability with low-order tools is limited to stability analysis, describing the growth/rates of these oscillations, and cannot be used to develop a linearized flame response

function. The mean flame shape change due to acoustics, which predominantly determines the non-linear response of the flame and the limit cycle amplitude, can only be predicted using high-fidelity tools, like self-excited LES, or other techniques like the method of successive approximations (if these underlying models can be developed). However, a low-order model-based prediction of the mean flame shape is difficult when there are multiple concurrent acoustic modes.

REFERENCES

1. Crocco, L. "Aspects of Combustion Stability in Liquid Propellant Rocket Motors Part I: Fundamentals. Low Frequency Instability With Monopropellants," *Journal of the American Rocket Society* Vol. 21, No. 6, 1951, pp. 163-178.

   doi: 10.2514/8.4393
2. Crocco, L. "Aspects of Combustion Stability in Liquid Propellant Rocket Motors Part II: Low Frequency Instability with Bipropellants. High Frequency Instability," *Journal of the American Rocket Society* Vol. 22, No. 1, 1952, pp. 7-16.

   doi: 10.2514/8.4410
3. Crocco, L. "High-Frequency Combustion Instability in Rocket Motor with Concentrated Combustion," *Journal of the American Rocket Society* Vol. 23, No. 5, 1953, pp. 301-313.

   doi: 10.2514/8.4623
4. Crocco, L. "Measurements of the Combustion Time Lag in a Liquid Bipropellant Rocket Motor," *Journal of Jet Propulsion* Vol. 26, No. 1, 1956, pp. 20-25.

   doi: 10.2514/8.6907
5. Crocco, L. "Theory of Liquid PropelIant Rocket Combustion Instability and Its Experimental Verification," *ARS Journal* Vol. 30, No. 2, 1960, pp. 159-168.

   doi: 10.2514/8.5020
6. Crocco, L. "Transverse Combustion Instability in Liquid Propellant Rocket Motors," *ARS Journal* Vol. 32, No. 3, 1962, pp. 366-373.

   doi: 10.2514/8.6022
7. Coulbert, C. D. "Selecting cooling techniques for liquid rockets for spacecraft," *Journal of Spacecraft and Rockets* Vol. 1, No. 2, 1964, pp. 129-139.

   doi: 10.2514/3.27612
8. Zinn, B. T. "A theoretical study of nonlinear combustion instability in liquid-propellant rocket engines," *AIAA Journal* Vol. 6, No. 10, 1968, pp. 1966-1972.

   doi: 10.2514/3.4908
9. Culick, F. E. C. "The Stability of One-Dimensional Motions in a Rocket Motor," *Combustion Science and Technology* Vol. 7, No. 4, 1973, pp. 165-175.

   doi: 10.1080/00102207308952355
10. Culick, F. E. C. "Stability of Three-Dimensional Motions in a Combustion Chamber," *Combustion Science and Technology* Vol. 10, No. 3-4, 1975, pp. 109-124.

    doi: 10.1080/00102207508946663
11. Rayleigh, L. *The Theory of Sound*. New York: Dover, 1945.
12. Culick, F. E. C., and Magiawala, K. "Excitation of acoustic modes in a chamber by vortex shedding," *Journal of Sound and Vibration* Vol. 64, No. 3, 1979, pp. 455-457.

    doi: 10.1016/0022-460X(79)90591-1

13. Schlimpert, S., Hemchandra, S., Meinke, M., and Schröder, W. "Hydrodynamic instability and shear layer effect on the response of an acoustically excited laminar premixed flame," *Combustion and Flame* Vol. 162, No. 2, 2015, pp. 345-367.

doi: 10.1016/j.combustflame.2014.08.001

14. O'Connor, J., Acharya, V., and Lieuwen, T. "Transverse combustion instabilities: Acoustic, fluid mechanic, and flame processes," *Progress in Energy and Combustion Science* Vol. 49, 2015, pp. 1-39.

doi: 10.1016/j.pecs.2015.01.001

15. Kirthy, S. K., Hemchandra, S., Hong, S., Shanbhogue, S., and Ghoniem, A. F. "Role of Shear Layer Instability in Driving Pressure Oscillations in a Backward Facing Step Combustor," No. 49767, 2016, p. V04BT04A010.

doi: 10.1115/GT2016-57322

16. Mongia, R., Dibble, R., and Lovett, J. "Measurement of Air-Fuel Ratio Fluctuations Caused by Combustor Driven Oscillations," *ASME 1998 International Gas Turbine and Aeroengine Congress and Exhibition*. Vol. 3, ASME, Stockholm, Sweden, 1998, p. V003T06A026.

17. Lieuwen, T., and Zinn, B. T. "The role of equivalence ratio oscillations in driving combustion instabilities in low NOx gas turbines," *Symposium (International) on Combustion* Vol. 27, No. 2, 1998, pp. 1809-1816.

doi: 10.1016/S0082-0784(98)80022-2

18. Sattelmayer, T. "Influence of the Combustor Aerodynamics on Combustion Instabilities From Equivalence Ratio Fluctuations," *Journal of Engineering for Gas Turbines and Power* Vol. 125, No. 1, 2002, pp. 11-19.

doi: 10.1115/1.1365159

19. Rajaram, R., and Lieuwen, T. "Acoustic radiation from turbulent premixed flames," *Journal of Fluid Mechanics* Vol. 637, 2009, pp. 357-385.

doi: 10.1017/S0022112009990681

20. Yang, V., Kim, S. I., and Culick, F. E. C. "Triggering of Longitudinal Pressure Oscillations in Combustion Chambers. I: Nonlinear Gasdynamics," *Combustion Science and Technology* Vol. 72, No. 4-6, 1990, pp. 183-214.

doi: 10.1080/00102209008951647

21. Roediger, T., Lammel, O., Aigner, M., Beck, C., and Krebs, W. "Part-Load Operation of a Piloted FLOX® Combustion System," *Journal of Engineering for Gas Turbines and Power* Vol. 135, No. 3, 2013, pp. 031503-031503.

doi: 10.1115/1.4007754

22. Lammel, O., Schütz, H., Schmitz, G., Lückerath, R., Stöhr, M., Noll, B., Aigner, M., Hase, M., and Krebs, W. "FLOX® Combustion at High Power Density and High Flame Temperatures," *Journal of Engineering for Gas Turbines and Power* Vol. 132, No. 12, 2010, pp. 121503-121503.

doi: 10.1115/1.4001825

23. Zahn, M., Schulze, M., Hirsch, C., and Sattelmayer, T. "Impact of Quarter Wave Tube Arrangement on Damping of Azimuthal Modes," No. 49750, 2016, p. V04AT04A025.

doi: 10.1115/GT2016-56450
24. Sohn, C. H., and Park, J. H. "A comparative study on acoustic damping induced by half-wave, quarter-wave, and Helmholtz resonators," *Aerospace Science and Technology* Vol. 15, No. 8, 2011, pp. 606-614.

doi: 10.1016/j.ast.2010.12.004
25. Fok, L., and Zhang, X. "Negative acoustic index metamaterial," *Physical Review B* Vol. 83, No. 21, 2011, p. 214304.

doi: 10.1103/PhysRevB.83.214304
26. Bandaru, R. V., and Turns, S. R. "Turbulent jet flames in a crossflow: effects of some jet, crossflow, and pilot-flame parameters on emissions," *Combustion and Flame* Vol. 121, No. 1–2, 2000, pp. 137-151.

doi: 10.1016/S0010-2180(99)00166-2
27. Goh, S.-F., and Gollahalli, S. R. "Pilot Flame Effects on Gas Jet Flames in Crossflow," *Journal of Propulsion and Power* Vol. 18, No. 5, 2002, pp. 1068-1075.

doi: 10.2514/2.6036
28. Bray, K. N. C., and Fletcher, R. S. "Pilot Ignition of Cold Supersonic Flows," *AIAA Journal* Vol. 10, No. 1, 1972, pp. 72-79.

doi: 10.2514/3.50068
29. Masri, A. R., and Pope, S. B. "PDF calculations of piloted turbulent nonpremixed flames of methane," *Combustion and Flame* Vol. 81, No. 1, 1990, pp. 13-29.

doi: 10.1016/0010-2180(90)90066-Z
30. Cao, R. R., and Pope, S. B. "The influence of chemical mechanisms on PDF calculations of nonpremixed piloted jet flames," *Combustion and Flame* Vol. 143, No. 4, 2005, pp. 450-470.

doi: 10.1016/j.combustflame.2005.08.018
31. Nair, S., and Lieuwen, T. "Acoustic Detection of Imminent Blowout in Pilot and Swirl Stabilized Combustors," *ASME Turbo Expo 2003*. Vol. 2, ASME, Atlanta, Georgia, USA, 2003.
32. Nair, S., and Lieuwen, T. "Acoustic Detection of Blowout in Premixed Flames," *Journal of Propulsion and Power* Vol. 21, No. 1, 2005, pp. 32-39.

doi: 10.2514/1.5658
33. Nair, S., and Lieuwen, T. C. "Near-Blowoff Dynamics of a Bluff-Body Stabilized Flame," *Journal of Propulsion and Power* Vol. 23, No. 2, 2007, pp. 421-427.

doi: 10.2514/1.24650
34. Li, C., Tang, H., Jing, L., and Zhu, M. "Investigations of the Stabilities of Piloted Flames Using Blast Furnace Gas," *Journal of Engineering for Gas Turbines and Power* Vol. 138, No. 3, 2015, pp. 031505-031505.

doi: 10.1115/1.4031348
35. Sheikhi, M. R. H., Drozda, T. G., Givi, P., Jaberi, F. A., and Pope, S. B. "Large eddy simulation of a turbulent nonpremixed piloted methane jet flame (Sandia Flame D)," *Proceedings of the Combustion Institute* Vol. 30, No. 1, 2005, pp. 549-556.

doi: 10.1016/j.proci.2004.08.028
36. Wang, H., and Chen, Y. "Comprehensive chemical kinetic modeling of turbulent methane/air piloted jet flames," *Combustion and Flame* Vol. 151, No. 1–2, 2007, pp. 386-390.

doi: 10.1016/j.combustflame.2007.03.009
37. Rittler, A., Proch, F., and Kempf, A. M. "LES of the Sydney piloted spray flame series with the PFGM/ATF approach and different sub-filter models," *Combustion and Flame* Vol. 162, No. 4, 2015, pp. 1575-1598.

doi: 10.1016/j.combustflame.2014.11.025
38. Chen, Y., and Ihme, M. "Large-eddy simulation of a piloted premixed jet burner," *Combustion and Flame* Vol. 160, No. 12, 2013, pp. 2896-2910.

doi: 10.1016/j.combustflame.2013.07.009
39. Dunn, M. J., Masri, A. R., and Bilger, R. W. "A new piloted premixed jet burner to study strong finite-rate chemistry effects," *Combustion and Flame* Vol. 151, No. 1–2, 2007, pp. 46-60.

doi: 10.1016/j.combustflame.2007.05.010
40. Barlow, R. S., Meares, S., Magnotti, G., Cutcher, H., and Masri, A. R. "Local extinction and near-field structure in piloted turbulent CH4/air jet flames with inhomogeneous inlets," *Combustion and Flame*, 2015.

doi: 10.1016/j.combustflame.2015.06.009
41. Kundu, A., Klingmann, J., Subash, A. A., and Collin, R. "Experimental and Numerical Investigation of a Prototype Low NOx Gas Turbine Burner," No. 50213, 2016, p. V001T03A013.

doi: 10.1115/POWER2016-59592
42. Kundu, A., Klingmann, J., Subash, A. A., and Collin, R. "Pilot-Pilot Interaction Effects on a Prototype DLE Gas Turbine Burner Combustion," No. 49767, 2016, p. V04BT04A012.

doi: 10.1115/GT2016-57338
43. Dhanuka, S. K., Temme, J. E., and Driscoll, J. "Unsteady Aspects of Lean Premixed Prevaporized Gas Turbine Combustors: Flame-Flame Interactions," *Journal of Propulsion and Power* Vol. 27, No. 3, 2011, pp. 631-641.

doi: 10.2514/1.B34001
44. Kumaran, K., and Shet, U. S. P. "Effect of swirl on lean flame limits of pilot-stabilized open premixed turbulent flames," *Combustion and Flame* Vol. 151, No. 1–2, 2007, pp. 391-395.

doi: 10.1016/j.combustflame.2007.06.016
45. Foley, C. W., Chterev, I., Seitzman, J., and Lieuwen, T. "High Resolution PIV and CH-PLIF Measurements and Analysis of a Shear Layer Stabilized Flame," No. 56697, 2015, p. V04BT04A027.

doi: 10.1115/GT2015-43387
46. Aguilar, M., Malanoski, M., Adhitya, G., Emerson, B., Acharya, V., Noble, D., and Lieuwen, T. "Helical Flow Disturbances in a Multinozzle Combustor," *Journal of Engineering for Gas Turbines and Power* Vol. 137, No. 9, 2015, pp. 091507-091507.

doi: 10.1115/1.4029696

47. Smith, T., Emerson, B., Chterev, I., Noble, D. R., and Lieuwen, T. "Flow Dynamics in Single and Multi-Nozzle Swirl Flames," No. 49767, 2016, p. V04BT04A041.

doi: 10.1115/GT2016-57755

48. Färber, J., Koch, R., Bauer, H.-J., Hase, M., and Krebs, W. "Effects of Pilot Fuel and Liner Cooling on the Flame Structure in a Full Scale Swirl-Stabilized Combustion Setup," *Journal of Engineering for Gas Turbines and Power* Vol. 132, No. 9, 2010, pp. 091501-091501-7.

doi: 10.1115/1.4000588

49. Froud, D., O'Doherty, T., and Syred, N. "Phase averaging of the precessing vortex core in a swirl burner under piloted and premixed combustion conditions," *Combustion and Flame* Vol. 100, No. 3, 1995, pp. 407-412.

doi: 10.1016/0010-2180(94)00167-Q

50. Bradley, D., Gaskell, P. H., Gu, X. J., Lawes, M., and Scott, M. J. "Premixed turbulent flame instability and NO formation in a lean-burn swirl burner," *Combustion and Flame* Vol. 115, No. 4, 1998, pp. 515-538.

doi: 10.1016/S0010-2180(98)00024-8

51. Albrecht, P., Bade, S., Lacarelle, A., Paschereit, C. O., and Gutmark, E. "Instability Control by Premixed Pilot Flames," *Journal of Engineering for Gas Turbines and Power* Vol. 132, No. 4, 2010, pp. 041501-041501.

doi: 10.1115/1.3019293

52. Wolf, P., Staffelbach, G., Roux, A., Gicquel, L., Poinsot, T., and Moureau, V. "Massively parallel LES of azimuthal thermo-acoustic instabilities in annular gas turbines," *Comptes Rendus Mécanique* Vol. 337, No. 6, 2009, pp. 385-394.

doi: 10.1016/j.crme.2009.06.003

53. Urbano, A., Selle, L., Staffelbach, G., Cuenot, B., Schmitt, T., Ducruix, S., and Candel, S. "Exploration of combustion instability triggering using Large Eddy Simulation of a multiple injector liquid rocket engine," *Combustion and Flame* Vol. 169, 2016, pp. 129-140.

doi: 10.1016/j.combustflame.2016.03.020

54. O'Connor, J., and Lieuwen, T. "Disturbance Field Characteristics of a Transversely Excited Burner," *Combustion Science and Technology* Vol. 183, No. 5, 2011, pp. 427-443.

doi: 10.1080/00102202.2010.529478

55. Hakim, L., Schmitt, T., Ducruix, S., and Candel, S. "Dynamics of a transcritical coaxial flame under a high-frequency transverse acoustic forcing: Influence of the modulation frequency on the flame response," *Combustion and Flame* Vol. 162, No. 10, 2015, pp. 3482-3502.

doi: 10.1016/j.combustflame.2015.05.022

56. Zellhuber, M., Meraner, C., Kulkarni, R., Polifke, W., and Schuermans, B. "Large Eddy Simulation of Flame Response to Transverse Acoustic Excitation in a Model Reheat Combustor," *Journal of Engineering for Gas Turbines and Power* Vol. 135, No. 9, 2013, pp. 091508-091508-9.

doi: 10.1115/1.4024940

57. O'Connor, J. "Visualization of Shear Layer Dynamics in a Transversely Forced Flow and Flame," *Journal of Propulsion and Power* Vol. 31, No. 4, 2015, pp. 1127-1136.

doi: 10.2514/1.B35457

58. Saurabh, A., Moeck, J. P., and Paschereit, C. O. "Swirl Flame Response to Simultaneous Axial and Transverse Velocity Fluctuations," *Journal of Engineering for Gas Turbines and Power* Vol. 139, No. 6, 2017, pp. 061502-061502-7.

doi: 10.1115/1.4035231

59. Wang, M., Freund, J. B., and Lele, S. K. "Computational prediction of flow-generated sound," *Annual Review of Fluid Mechanics* Vol. 38, No. 1, 2006, pp. 483-512.

doi: 10.1146/annurev.fluid.38.050304.092036

60. Schwing, J., Sattelmayer, T., and Noiray, N. "Interaction of Vortex Shedding and Transverse High-Frequency Pressure Oscillations in a Tubular Combustion Chamber," No. 54624, 2011, pp. 259-268.

doi: 10.1115/GT2011-45246

61. Schwing, J., Grimm, F., and Sattelmayer, T. "A Model for the Thermo-Acoustic Feedback of Transverse Acoustic Modes and Periodic Oscillations in Flame Position in Cylindrical Flame Tubes," No. 44687, 2012, pp. 553-566.

doi: 10.1115/GT2012-68775

62. Berger, F. M., Hummel, T., Hertweck, M., Kaufmann, J., Schuermans, B., and Sattelmayer, T. "High-Frequency Thermoacoustic Modulation Mechanisms in Swirl-Stabilized Gas Turbine Combustors—Part I: Experimental Investigation of Local Flame Response," *Journal of Engineering for Gas Turbines and Power* Vol. 139, No. 7, 2017, pp. 071501-071501-9.

doi: 10.1115/1.4035591

63. Hummel, T., Berger, F., Hertweck, M., Schuermans, B., and Sattelmayer, T. "High-Frequency Thermoacoustic Modulation Mechanisms in Swirl-Stabilized Gas Turbine Combustors—Part II: Modeling and Analysis," *Journal of Engineering for Gas Turbines and Power* Vol. 139, No. 7, 2017, pp. 071502-071502-10.

doi: 10.1115/1.4035592

64. Zellhuber, M., Schwing, J., Schuermans, B., Sattelmayer, T., and Polifke, W. "Experimental and Numerical Investigation of Thermoacoustic Sources Related to High-Frequency Instabilities," Vol. 6, No. 1, 2014, pp. 1-34.

doi: 10.1260/1756-8277.6.1.1

65. Garby, R., Selle, L., and Poinsot, T. "Large-Eddy Simulation of combustion instabilities in a variable-length combustor," *Comptes Rendus Mécanique* Vol. 341, No. 1, 2013, pp. 220-229.

doi: 10.1016/j.crme.2012.10.020

66. James, S., Portillo, J., Yen, Y., and William, A. "Non-Linear Characteristics of Longitudinal Instabilities in a Model Rocket Combustor," *43rd AIAA/ASME/SAE/ASEE Joint Propulsion Conference & Exhibit*. American Institute of Aeronautics and Astronautics, 2007.

67. Sisco, J., Portillo, J., Yu, Y., and Anderson, W. "Non-Linear Characteristics of Longitudinal Instabilities in a Model Rocket Combustor," *43rd AIAA/ASME/SAE/ASEE Joint Propulsion Conference & Exhibit*. American Institute of Aeronautics and Astronautics, 2007.

68. Yen, Y., Loral, O. H., James, S., and William, A. "Experimental Study of High-Frequency Combustion Instability in a Continuously Variable Resonance Combustor (CVRC)," *47th AIAA Aerospace Sciences Meeting including The New Horizons Forum and Aerospace Exposition*. American Institute of Aeronautics and Astronautics, 2009.
69. Yen, Y., Stefan, K., James, S., and William, A. "Combustion Instability of Gaseous Fuels in a Continuously Variable Resonance Chamber (CVRC)," *44th AIAA/ASME/SAE/ASEE Joint Propulsion Conference & Exhibit*. American Institute of Aeronautics and Astronautics, 2008.
70. Sisco, J. C., Yu, Y. C., Sankaran, V., and Anderson, W. E. "Examination of mode shapes in an unstable model combustor," *Journal of Sound and Vibration* Vol. 330, No. 1, 2011, pp. 61-74.

doi: 10.1016/j.jsv.2010.07.016
71. Yu, Y., Sisco, J. C., Rosen, S., Madhav, A., and Anderson, W. E. "Spontaneous Longitudinal Combustion Instability in a Continuously-Variable Resonance Combustor," *Journal of Propulsion and Power* Vol. 28, No. 5, 2012, pp. 876-887.

doi: 10.2514/1.B34308
72. Lammel, O., Stöhr, M., Kutne, P., Dem, C., Meier, W., and Aigner, M. "Experimental Analysis of Confined Jet Flames by Laser Measurement Techniques," *Journal of Engineering for Gas Turbines and Power* Vol. 134, No. 4, 2012, pp. 041506-041506-9.

doi: 10.1115/1.4004733
73. Patil, S., Cooper, J., Orsino, S., Meadows, J., Valdes, R., and Laster, W. R. "Investigation of Single-Jet Combustor Near Lean Blowout Conditions Using Flamelet-Generated Manifold Combustion Model and Detailed Chemistry," *Journal of Engineering for Gas Turbines and Power* Vol. 138, No. 12, 2016, pp. 121503-121503-7.

doi: 10.1115/1.4034041
74. Slabaugh, C. D., Pratt, A. C., Lucht, R. P., Meyer, S. E., Benjamin, M., Lyle, K., and Kelsey, M. "The development of an optically accessible, high-power combustion test rig," Vol. 85, No. 3, 2014, p. 035105.

doi: 10.1063/1.4867084
75. Meyer, S. E., Heister, S. D., Slabaugh, C., Lucht, R. P., Pratt, A., Gejji, R. M., Bedard, M., and Lemcherfi, A. "Design and Development of the High Pressure Combustion Laboratory at Purdue University," *53rd AIAA/SAE/ASEE Joint Propulsion Conference*. American Institute of Aeronautics and Astronautics, 2017.
76. Portillo, J., Jim, S., Martin, J. C., Venkateswaran, S., and William, A. "Generalized Combustion Instability Model," *42nd AIAA/ASME/SAE/ASEE Joint Propulsion Conference & Exhibit*. American Institute of Aeronautics and Astronautics, 2006.
77. Portillo, J., James, S., Yen, Y., Venkateswaran, S., and William, A. "Application of a Generalized Instability Model to a Longitudinal Mode Combustion Instability," *43rd AIAA/ASME/SAE/ASEE Joint Propulsion Conference & Exhibit*. American Institute of Aeronautics and Astronautics, 2007.
78. Harmen, K., Werner, K., Juan Enrique, P., and Jim, K. "Prediction of Thermoacoustic Limit Cycles During Premixed Combustion using the Modified Galerkin Approach," *46th AIAA/ASME/SAE/ASEE Joint Propulsion Conference & Exhibit*. American Institute of Aeronautics and Astronautics, 2010.
79. Jared, P., Kock, B., Werner, K., and Juan, P. "Application of a Generalized Instability Model to Industrial Annular Combustion Chambers," *50th AIAA Aerospace Sciences Meeting including the*

New Horizons Forum and Aerospace Exposition. American Institute of Aeronautics and Astronautics, 2012.

80. Buschhagen, T., Gejji, R., Philo, J., Tran, L., Enrique Portillo Bilbao, J., and Slabaugh, C. D. "Experimental Investigation of Self-Excited Combustion Instabilities in a Lean, Premixed, Gas Turbine Combustor at High Pressure," *Journal of Engineering for Gas Turbines and Power* Vol. 140, No. 11, 2018, pp. 111503-111503-9.

doi: 10.1115/1.4039760

81. Buschhagen, T., Gejji, R., Philo, J., Tran, L., Bilbao, J. E. P., and Slabaugh, C. D. "Self-excited transverse combustion instabilities in a high pressure lean premixed jet flame," *Proceedings of the Combustion Institute*, 2018.

doi: 10.1016/j.proci.2018.07.086

82. Tay-Wo-Chong, L., and Polifke, W. "Large Eddy Simulation-Based Study of the Influence of Thermal Boundary Condition and Combustor Confinement on Premix Flame Transfer Functions," *Journal of Engineering for Gas Turbines and Power* Vol. 135, No. 2, 2013, pp. 021502-021502-9.

doi: 10.1115/1.4007734

83. Weller, H. G., Tabor, G., Gosman, A. D., and Fureby, C. "Application of a flame-wrinkling les combustion model to a turbulent mixing layer," *Symposium (International) on Combustion* Vol. 27, No. 1, 1998, pp. 899-907.

doi: 10.1016/S0082-0784(98)80487-6

84. Polifke, W., Wall, C., and Moin, P. "Partially reflecting and non-reflecting boundary conditions for simulation of compressible viscous flow," *Journal of Computational Physics* Vol. 213, No. 1, 2006, pp. 437-449.

doi: 10.1016/j.jcp.2005.08.016

85. Brown, J. C. "Calculation of a constant Q spectral transform," Vol. 89, No. 1, 1991, pp. 425-434.

doi: 10.1121/1.400476

86. Brown, J. C., and Puckette, M. S. "An efficient algorithm for the calculation of a constant Q transform," Vol. 92, No. 5, 1992, pp. 2698-2701.

doi: 10.1121/1.404385

87. Smith, T., Emerson, B., Proscia, W., and Lieuwen, T. "Flame Response to Transverse Acoustic Forcing With Minimal Axial Coupling," No. 50848, 2017, p. V04AT04A050.

doi: 10.1115/GT2017-63812

88. Acharya, V. S., Shin, D.-H., and Lieuwen, T. "Premixed Flames Excited by Helical Disturbances: Flame Wrinkling and Heat Release Oscillations," *Journal of Propulsion and Power* Vol. 29, No. 6, 2013, pp. 1282-1291.

doi: 10.2514/1.B34883

89. Schwing, J., and Sattelmayer, T. "High-Frequency Instabilities in Cylindrical Flame Tubes: Feedback Mechanism and Damping," No. 55102, 2013, p. V01AT04A003.

doi: 10.1115/GT2013-94064

90. Hummel, T., Temmler, C., Schuermans, B., and Sattelmayer, T. "Reduced-Order Modeling of Aeroacoustic Systems for Stability Analyses of Thermoacoustically Noncompact Gas Turbine Combustors," *Journal of Engineering for Gas Turbines and Power* Vol. 138, No. 5, 2015, pp. 051502-051502.

doi: 10.1115/1.4031542

91. Berger, F. M., Hummel, T., Schuermans, B., and Sattelmayer, T. "Pulsation-Amplitude-Dependent Flame Dynamics of High-Frequency Thermoacoustic Oscillations in Lean-Premixed Gas Turbine Combustors," *Journal of Engineering for Gas Turbines and Power* Vol. 140, No. 4, 2017, pp. 041507-041507-10.

doi: 10.1115/1.4038036

92. Hummel, T., Hammer, K., Romero, P., Schuermans, B., and Sattelmayer, T. "Low-Order Modeling of Nonlinear High-Frequency Transversal Thermoacoustic Oscillations in Gas Turbine Combustors," *Journal of Engineering for Gas Turbines and Power* Vol. 139, No. 7, 2017, pp. 071503-071503-11.

doi: 10.1115/1.4035529